FINAL REPORT

Project Title: Localized Deformation as a Primary Cause of Irradiation Assisted Stress Corrosion Cracking

Covering Period: July 1, 2005 to December 31, 2008

Date of Report: March 31, 2009

Recipient: University of Michigan
2355 Bonisteel Blvd
Ann Arbor, MI 48109-2104

Award Number: DE-FG07-05ID14703

Principal Investigator: Gary S. Was, 734 763-4675, gsw@umich.edu

Project Objective: The objective of this project is to determine whether deformation mode is a primary factor in the mechanism of irradiation assisted intergranular stress corrosion cracking of austenitic alloys in light water reactor core components. Deformation mode will be controlled by both the stacking fault energy of the alloy and the degree of irradiation. In order to establish that localized deformation is a major factor in IASCC, the stacking fault energies of the alloys selected for study must be measured. Second, it is completely unknown how dose and SFE trade-off in terms of promoting localized deformation. Finally, it must be established that it is the localized deformation, and not some other factor that drives IASCC.

Summary

The stacking fault energies were measured in all seven alloys and the results were compared to the predicted values. The measured SFE showed the same trend as predicted values and were within the range of similar alloys from other experimental measurements.

The IASCC susceptibility of the studied alloys increases with increasing irradiation dose when tested in a simulated BWR environment. Alloy A is susceptible to cracking at both 1 dpa and 5 dpa. Alloys C, D and E are resistant to cracking at 1 dpa but are susceptible to cracking at 5 dpa. Alloy B, F and G shows cracking resistance at both doses. IASCC was found to initiate at locations where a large slip channel intersects a grain boundary in simulated BWR environment.

Localized deformation was characterized in proton-irradiated austenitic alloys A-G irradiated to 1 and 5 dpa and strained to 1% and 3% at 288ºC in argon. The slip channels in all alloys are inhomogeneous at 1% plastic strain. At a higher strain of 3%, slip channels become more homogeneous. The average step height in the channel is much smaller in alloys B, F and G. High irradiation dose results in larger channel height. Localized grain boundary sliding was observed to be associated with large dislocation channels intersecting grain boundaries. Large regions of deformation around grain boundaries were observed when small dislocation channels interact with grain boundaries.

Localized deformation was found to be dependent on irradiation microstructures. The dislocation loops contribute more to localized deformation than voids because voids do not contribute to the formation of dislocation channels.

The correlation of SFE, hardness, RIS and localized deformation with IASCC was examined. The correlation strength was the highest for localized deformation (0.88) followed by hardness (0.54), SFE (0.5) and RIS (0-0.4). Localized grain boundary deformation caused by the intersection of large slip channels with grain boundaries is believed to be important for IG cracking. Results also imply that localized deformation may be the most important factor in crack initiation of irradiated alloys in BWR environments.

Table of Contents

Localized Deformation as a Primary Cause of Irradiation Assisted Stress Corrosion Cracking

1. Introduction

1.1 Background

Irradiation assisted stress corrosion cracking (IASCC) refers to intergranular stress corrosion cracking that is accelerated under the action of irradiation in light water reactor core components. It is referred to as "assisted" because irradiation enhances, or accelerates the IGSCC process over the unirradiated state. IASCC has been a problem in the nuclear industry for the last 30 years and continues to occur due to a lack of understanding of its underlying mechanism. It is the single most important problem in core component cracking in boiling water reactors (BWR) [1] and is of growing importance in pressurized water reactors (PWR). Understanding the mechanism of IASCC is required in order to provide guidance for the development of mitigation strategies.

The IASCC problem has taken on new urgency with the proposal of more advanced water reactor concepts under the Generation IV program [2], such as the supercritical water reactor (SCWR). The SCWR represents a more demanding environment than LWRs in temperature, irradiation dose and the corrosiveness of the media itself. As such, there is an even more pressing need to develop a solution to the IASCC problem. However, in order to do so, the underlying mechanism must first be understood. This proposal aims to establish such an understanding, which will lead directly to mitigation strategies for current and future reactors.

IASCC is affected by changes to both the water environment and the microstructure of the irradiated alloy. [3] However, the changes to the microstructure are the real concern since IASCC can be replicated in the laboratory by conducting stress corrosion cracking tests (either slow strain rate tensile tests (SSRT) or crack growth tests (CGR)) on pre-irradiated samples. In essence, changes to the environment can alter the severity of the cracking, but it is the irradiation-induced changes to the microstructure that trigger the occurrence of IASCC, as it has been replicated in BWR normal water chemistry (NWC), hydrogen water chemistry (HWC) and low potential PWR primary water.
One of the principal reasons why the IASCC mechanism has been so difficult to understand is the inseparability of the different material changes caused by irradiation. Figure 1-1 shows that the principal changes due to irradiation; microstructure (formation and growth of dislocation loops, voids, bubbles, phases), grain boundary chemistry (segregation of alloying and impurity elements to or from the grain boundary), and hardening, all follow a similar dose dependence. [4] At any irradiation dose, all three types of radiation effects are proceeding together at roughly the same rate, and there is no way to ascribe the resulting cracking behavior to one or any combination of them.

Another complicating factor has been the pre-occupation of the research community with finding a "smoking gun" or a single parameter that is responsible for cracking (e.g. a

threshold in yield strength, or segregation of a particular species to the grain boundary). Unfortunately, for every case that can be explained by a single parameter, there is one that can't. For example, the argument that segregation of impurities is the primary cause of IASCC is in conflict with the observation of IASCC in ultra-high purity alloys. The obsession with finding a simple indicator of IASCC susceptibility is beginning to give way to a realization that the mechanism is more likely due to several factors that may have varying levels of importance. Hence, the aim of this program is to identify a primary factor or primary cause, rather than the only factor. It is our belief that localized deformation is a primary factor in IASCC.

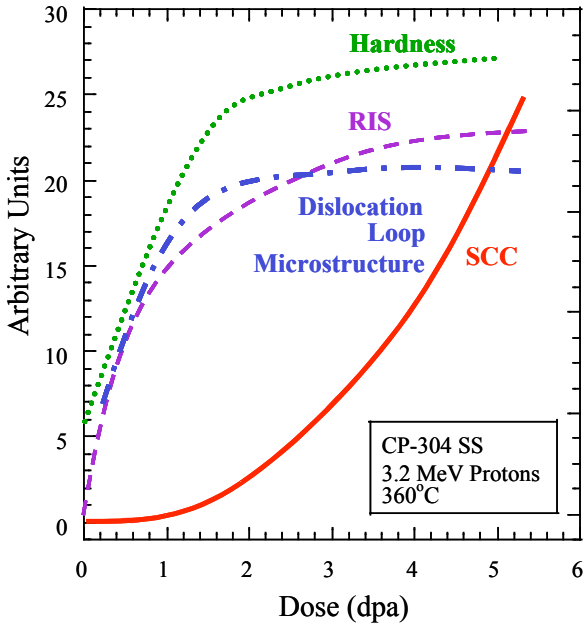

Figure 1-1: Schematic representation of the dose dependence of IASCC and other principal irradiation-induced changes

1.2 Insight into localized deformation as a key factor affecting IASCC

The development of post-irradiation annealing (PIA) as a technique to separate the different effects of irradiation on the alloy is a major advance in the understanding of the IASCC mechanism. The work was led by a key paper by Busby et al. [5] (supported by a 1999 NEER program grant) who showed that judicious selection of PIA time-temperature combinations could essentially anneal out the microstructure and hardening effects while leaving the radiation-induced grain boundary segregation intact. This strategy provided a means of assessing the effect of grain boundary composition on IASCC. Figure 1-2 shows the results of PIA studies that support the observation that IASCC susceptibility drops to zero long before grain boundary chromium content begins to change from the as-irradiated value. These results confirm that grain boundary chromium concentration is not a *primary* factor in IASCC in either normal water chemistry (BWR) or in primary water chemistry in a PWR primary system. To date there are 7 studies (see Figure 1-2)

[5-11] that support this conclusion. These results have collectively focused attention more closely on the role of the irradiated microstructure and radiation hardening.

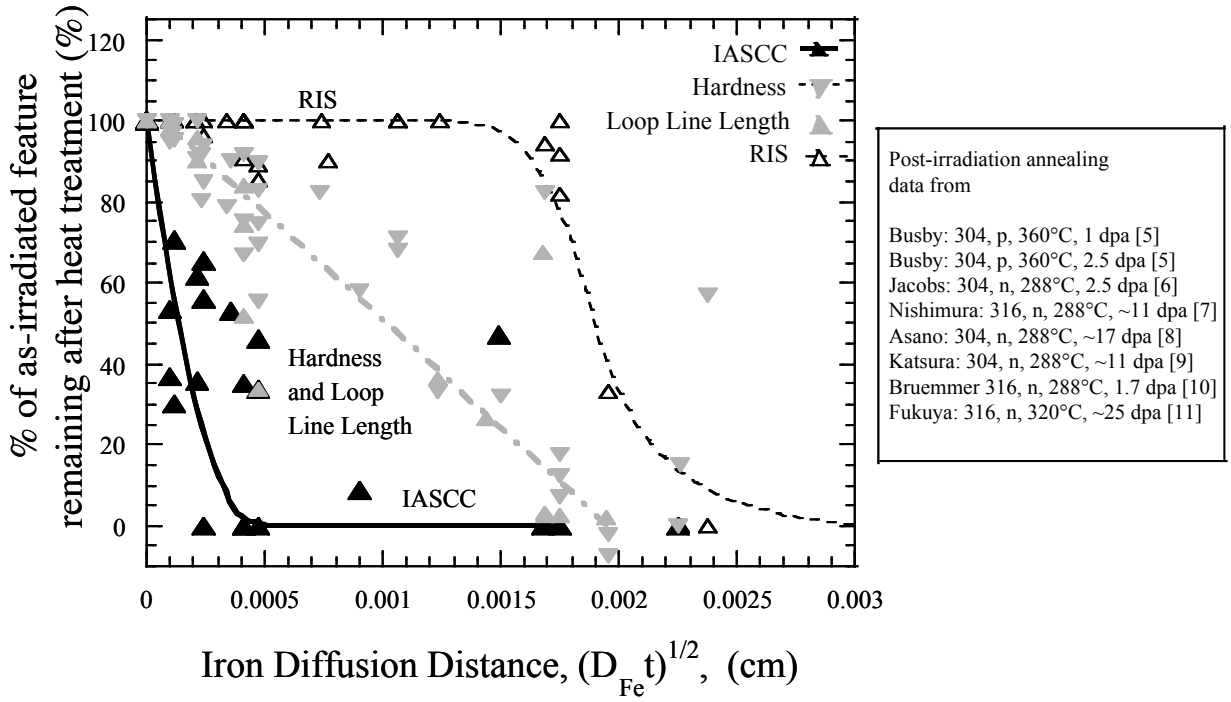

Figure 1-2: Summary of post-irradiation annealing data of neutron- and proton-irradiated stainless steels [5-11].

A second key result was the experiment by Hash et al. [12] that evaluated the role of the source of hardening (cold work vs. irradiation) on the IASCC susceptibility. He studied a commercial purity 304 SS using five samples of the same hardness, but containing different mixtures of cold work and irradiation. At the extremes were one sample that was only cold worked (35%) and one that was only irradiated (1.67 dpa at 360°C). The other three samples had varying amounts of cold-work and irradiation such that the total hardening was the same for all five samples (within 5% of each other). In constant extension rate tensile experiments in BWR normal water chemistry at 288°C, only the two samples with the highest irradiation dose cracked; the sample that underwent irradiation only and the one with the next highest dose and the lowest (10%) amount of cold work, Figure 1-3. In addition to the IASCC susceptibility, the prominence of surface slip steps was noticeably greater on those two samples. Slip steps are commonly observed in deformed, irradiated alloys and arise from the large amount of slip in dislocation channels that intersects the surface. In this case, the significance of the observation is that the localized deformation was much more prominent in the samples that cracked than in those that didn't, drawing attention to the possible role of localized deformation in IASCC.

Data exists to show that the degree of slip planarity correlates with IGSCC in unirradiated alloys. Bernstein and Thompson [13] conducted SCC experiments on a series of Fe-Cr-Ni alloys in which the Ni content was varied between 8% and 23%. Increasing Ni

content resulted in decreasing SCC. However, it is not the Ni content by itself that affects SCC; rather it is the effect of Ni on the stacking fault energy (SFE). SFE is known to affect slip planarity with lower values of SFE causing planar slip and higher values of SFE resulting in cellular dislocation networks. The increasing degree of slip planarity, a greater amount of IGSCC was observed.

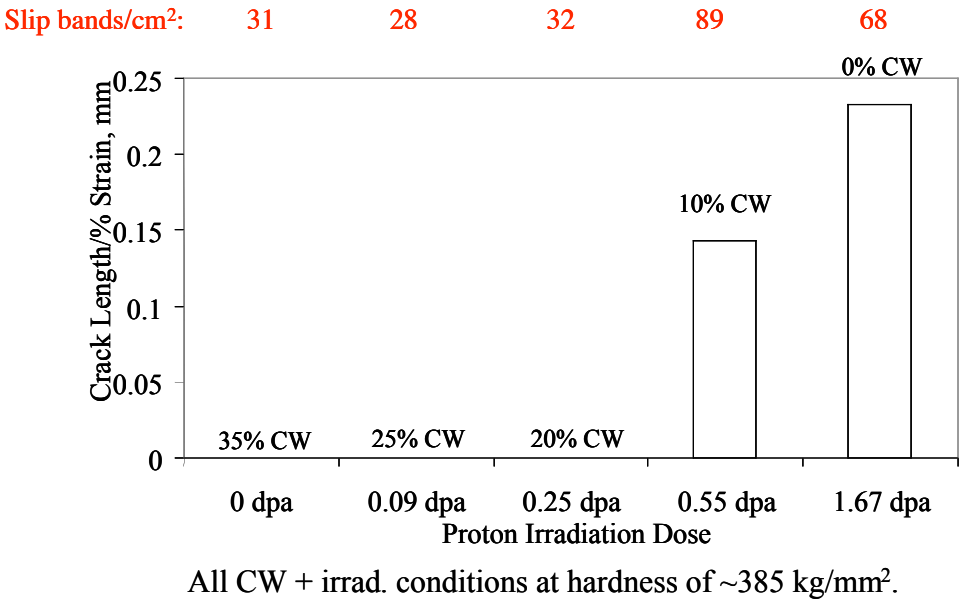

Figure 1-3: IG cracking and slip band activity in 288°C water as a function of irradiation dose and cold work [12]. All samples were tested with a hardness of 385 kg/mm^2 ($\pm$5%).

It is the impingement of intense, localized slip bands on grain boundaries that is believed to be associated with IGSCC. The way in which dislocations in the slip band interact with grain boundaries determines if IGSCC will occur. Interactions that promote IGSCC are the absorption of slip by the grain boundary where grain boundary sliding can rupture an otherwise protective oxide film, and the formation of wedge cracks at the grain boundary caused by the pile-up of dislocations in a slip band. In irradiated alloys, localized deformation occurs by dislocation channeling, which is a more severe form of planar deformation where strain in the channels can reach levels in excess of 200%. [14]

1.3 The potential role of localized deformation

In addition to SFE, slip planarity is also caused by irradiation through the formation of dislocation channels. These channels are formed by the passage of a dislocation through the matrix which clears out the small defects, therefore making the slip trace a path of least resistance for subsequent dislocations. Farrell et al. [15] conducted an analysis of dislocation channeling in irradiated austenitic steels as a function of dose and showed that with increasing dose, work hardening decreases and the amount of channeling, as measured by the volume of material occupied by the channel, sharply increases. So the

picture that has emerged is one in which intense localized deformation can result in the transmission of extremely large local strains to the grain boundary, which can result in cracking through either deformation (slip) in the grain boundary, or wedge crack nucleation, both of which can lead to rupture of the protective oxide film over the boundary and initiation of a new crack, or propagation of an existing one. Further, either a low SFE or an irradiated microstructure can induce localized deformation, making both features important factors in IASCC.

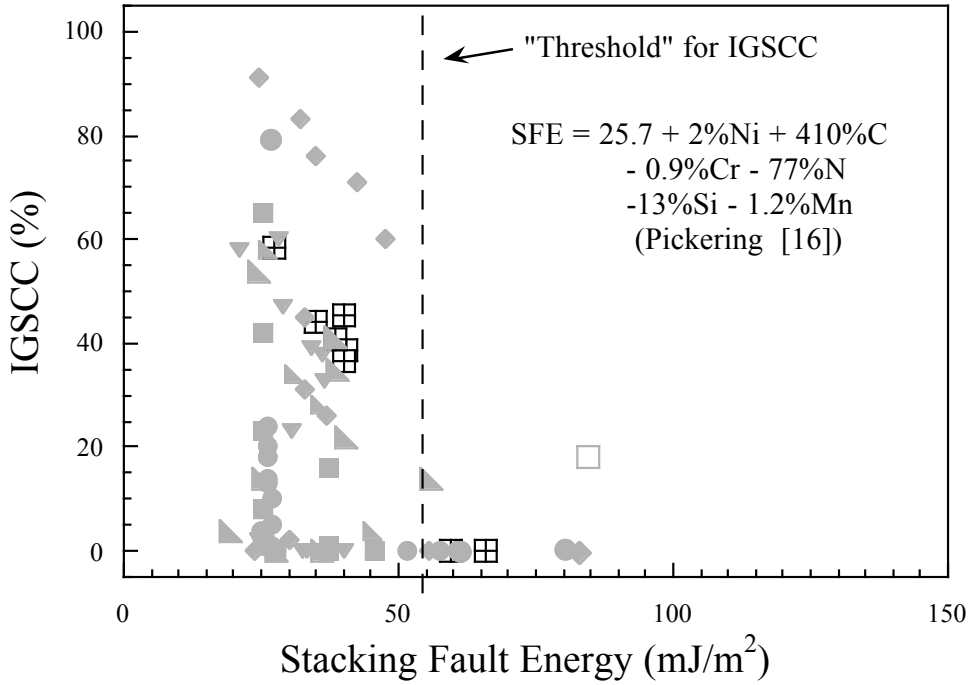

Figure 1-4: Cracking susceptibility in simulated BWR environment as a function stacking fault energy [16] for proton- and neutron-irradiated austenitic stainless steels.

The existing IASCC database can be evaluated with respect to the stacking fault energy to show that there is a strong correlation between IG cracking and SFE. The %IGSCC in irradiated austenitic alloys is shown as a function of SFE [16] in Figure 1-4. Note that there is a sharp threshold in IGSCC at a specific value of SFE (shown by the dashed line) such that high SFE alloys are resistant to IGSCC while low SFE alloys suffer much greater IGSCC. By far, the largest amount of data on IASCC is for 304 and 316 stainless steels. Generally, 316 SS is less susceptible to IASCC than is 304 SS. [4] By virtue of the higher Ni content in 316 SS, the SFE is higher, which correlates with greater IGSCC resistance. Figure 1-5 provides additional data plotted so as to show the combined effect of SFE and irradiation. Since IGSCC decreases with SFE but increases with dose, IASCC should be worse when either SFE is low or dose is high. As shown in Figure 1-5, the existing data follow a trend that supports this behavior. What is needed to establish the role of localized deformation in IASCC is a relationship like that shown in Figure 1-6 which plots IASCC susceptibility vs. degree of localized deformation. If such a relationship can be established, then it would show that deformation localization is a key factor in IASCC, and is independent of source (SFE vs. irradiation). It would also

establish localized deformation as a major controlling factor in IASCC that dominates other irradiation-induced features such as RIS, hardening, alloy composition or even dose. Finally, this approach would also indicate potential mitigation factors for IASCC (e.g., by increasing the SFE of the base alloy through solute addition.)

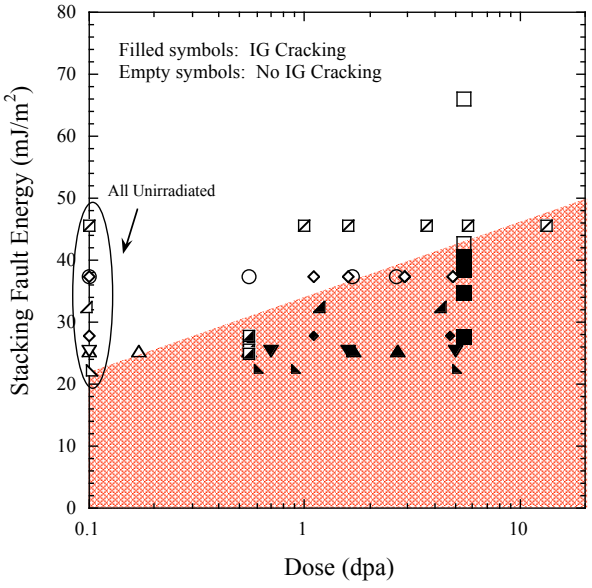

Figure 1-5: IASCC Susceptibility map: IGSCC as a function of dose and SFE [16] for proton and neutron-irradiated austenitic stainless steels.

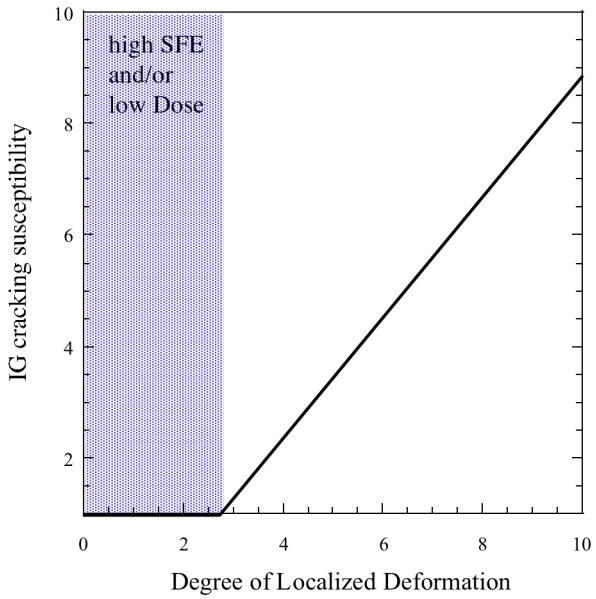

Figure 1-6: Hypothetical effect of degree of localized deformation on IGSCC. In this representation, the IGSCC susceptibility is a function only of the degree of localized deformation. If such a plot can be generated with statistical significance, then localized deformation must be a dominant factor in the process.

1.4 Objective

The objective of this project is to determine whether deformation mode is a primary factor in the mechanism of irradiation assisted intergranular stress corrosion cracking of austenitic alloys in light water reactor core components.

2. Experimental

2.1 Material selection

Seven alloys were chosen with various Ni and Cr content. The compositions of these alloys are shown in Table 2-1. The alloys were selected based on the hypothesis that the degree of localized deformation may vary with stacking fault energies. In austenitic alloys, stacking fault energies are known to be dependent on compositions. By varying the compositions, alloys with different SFEs may be achieved. It is ideal to select alloys that only vary in Ni and Cr content so that the effect of minor elements such as Si and P etc. on IASCC can be minimized.

Figure 2-1 shows a schematic illustration of how the value of SFE (as determined by calculation [16]) varies with alloy nickel content for alloys of various chromium contents. Alloys A, B and F systematically increase SFE by increasing nickel content with a constant Cr content. Alloys C and D are at similar SFE but different Ni contents. (Ideally they would be at the same SFE, but this is as close as we can get and maintain austenite stability.) Alloys D and E are at the same Ni content and different SFE. So taken together, this set of alloys covers the possible combinations of Ni content and SFE.

Alloy A is commercial grade alloy. It was chosen because of its very low SFE. The other six alloys are high purity alloys supplied by the General Electric Company.

Table 2-1: compositions of selected alloys.

Alloy #	Nominal	Fe	Cr	Ni	Mn	Si	P	C	SFE (mJ/m^2)
A	18Cr8Ni	71.04	18.30	8.50	1.38	0.65	0.03	0.04	25.2
B	18Cr12Ni	69.5	17.49	11.87	0.98	0.11	0.014	0.02	39.3
C	15Cr12Ni	71.1	15.76	12.04	0.98	0.10	<0.01	0.02	41.3
D	22Cr15Ni	61.99	22.00	15.00	1.00	0.10		0.02	42.9
E	13Cr15Ni	70.4	13.41	15.04	1.03	0.10	<0.01	0.016	47.7
F	18Cr25Ni	55.98	18.00	25.00	1.00	0.03	0.01	0.02	66.0
G	21Cr32Ni	75.06	20.73	31.16	0.94	0.10	0.014	0.014	72.7

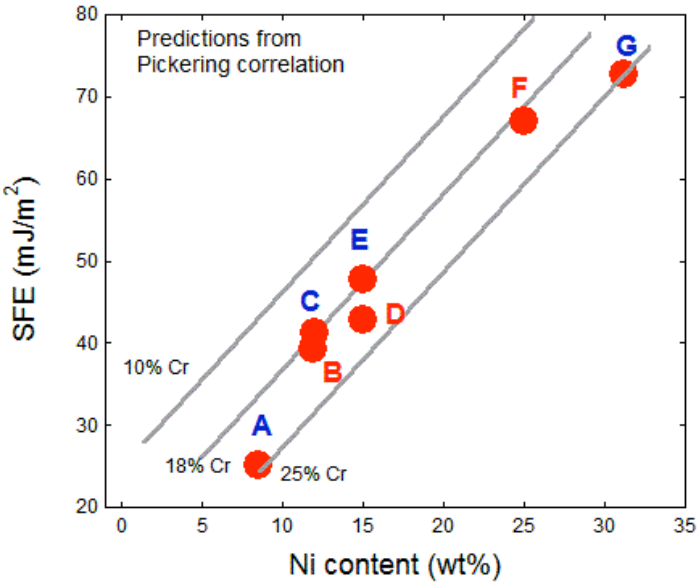

Figure 2-1: Plot of calculated SFE [16] vs. Ni content for various alloy Cr levels.

2.2 Sample fabrication

Two types of samples were required for this program: transmission electron microscopy (TEM) bars and stress corrosion cracking (SCC) specimens. Drawings of sample designs are provided in Figure 2-2. Using these sample dimensions, each irradiation can accommodate 4 SCC bars, and 3 TEM bars as shown in Figure 2-3.

Upon receipt of stock material, specimens for CERT testing and TEM analysis were fabricated using electric discharge machining at Shular Tool Co, in Oak Ridge, TN.

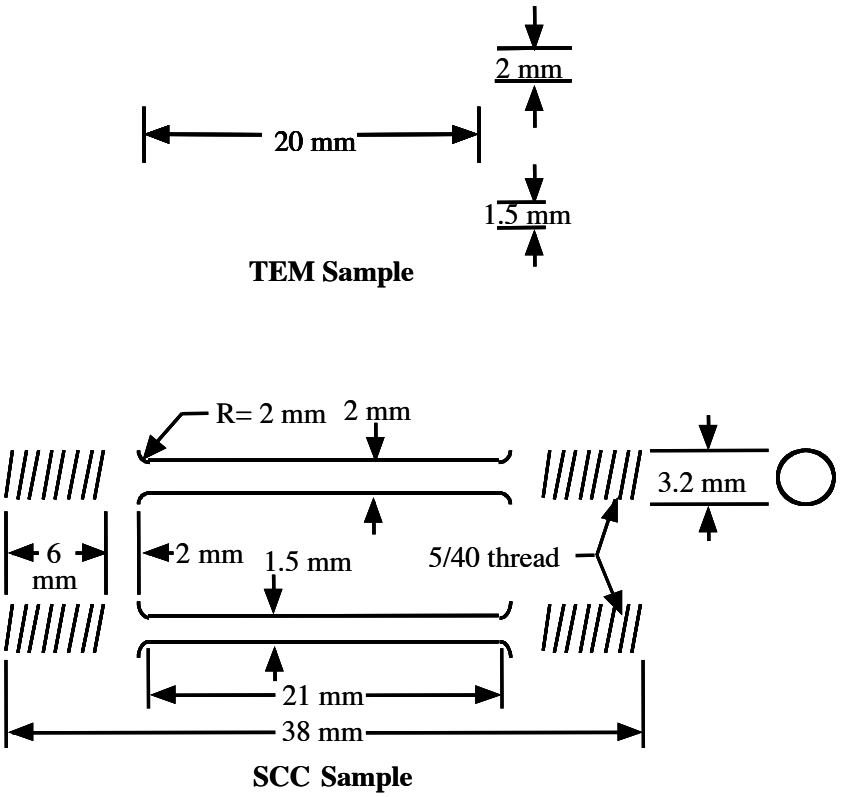

Figure 2-2: Schematic of samples for proton irradiations

2.3 Sample irradiation

Sample irradiations were performed using a specially designed stage connected to the General Ionex Tandetron accelerator at the Michigan Ion Beam Laboratory. Irradiations were conducted using 2-3.2 MeV protons at a dose rate of approximately 3×10^{-6} dpa/s (the experimental doses and dose rates are calculated using TRIM97 [17]), resulting in a nearly uniform damage rate through the first 35 μm of the proton range (40 μm). Irradiations were conducted to 5.5 dpa, where dpa is calculated using TRIM with a displacement energy of 40 eV. This value recommended in ASTM E 521-89. [18]

Sample bars were fixed to the stage at the top and bottom of each sample by hold-down bars. Multiple samples were irradiated simultaneously, providing duplicate samples for the same experimental conditions. The maximum allowable sample width for irradiation was 16 mm, providing flexibility in the number and type of samples loaded during a

given irradiation. A typical sample loading consisted of 3 TEM bars and 4 SCC bars (shown in Figure 2-3).

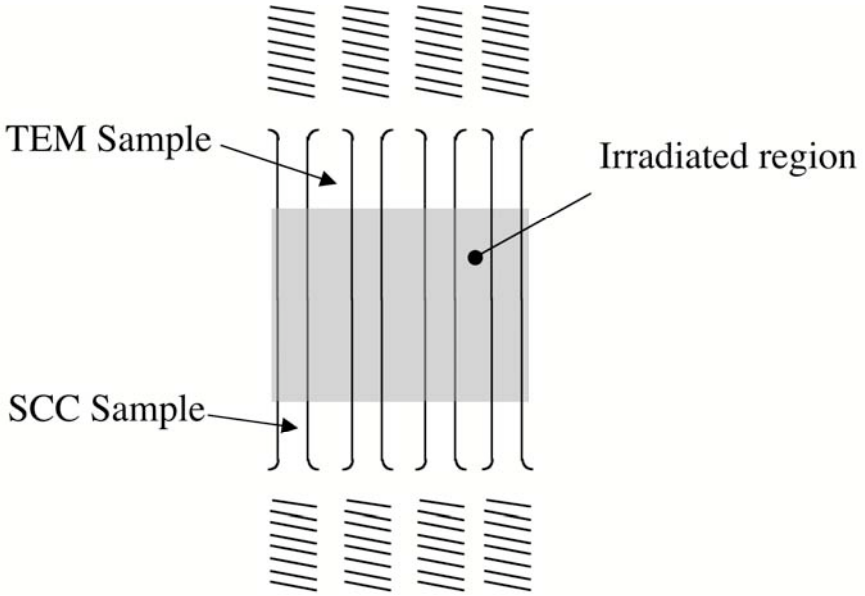

Figure 2-3: Schematic of sample configuration during proton irradiation.

The irradiation stage was electrically isolated from the beam line and four rectangular tantalum apertures were used to define the area on the sample bars that was irradiated with the proton beam. The approximately 3 mm diameter proton beam was rastered (at 255 and 2061 Hz, horizontally and vertically, respectively) across the stage so that about half the total beam current was deposited on the samples and half on the apertures. This rastering ensured that samples at any position on the stage received the same dose. Additionally, balancing the amount of current on each of the apertures centered the proton beam.

The irradiation stage was designed to control the sample temperature by controlling the stage temperature. The stage was heated using a resistive cartridge heater and cooled using room temperature air flowing through cooling lines that penetrated the back of the stage. The stage surface is made of copper to provide good heat conduction away from the samples. To provide effective thermal contact between the sample bars and the stage, a thin layer of indium was placed between the samples and the stage surface. Indium melts at 156°C and is molten at the irradiation temperature, maximizing the thermal contact between samples and stage. Sample temperature was monitored using two techniques. Type J (iron/constantan) thermocouples were spot welded directly to TEM sample surfaces to provide one temperature measurement. Typically, three or four thermocouples were attached to the samples during any one irradiation. A separate thermocouple monitored the temperature at the back of the stage. In addition to the thermocouples, a calibrated infrared pyrometer monitored the surface temperature of the

samples during irradiation. The pyrometer was also controlled remotely to scan the surface of the specimens to insure a uniform temperature. The pyrometer was calibrated prior to irradiation by heating the samples with the cartridge heater to the setpoint temperature and adjusting the pyrometer's emissivity setting so that the pyrometer reading matched that of the thermocouples. During irradiation, the sample temperature was controlled to ± 10°C of the set point temperature (360°C) by controlling the amount of heating and/or cooling provided to the stage. By providing a large fraction of the total heat input to the samples from the cartridge heater, temperature fluctuations due to fluctuations in beam current were minimized.

Experimental parameters were tracked continuously during irradiation using a PC-based monitoring system. The monitoring software recorded the stage current, current for each of the apertures, pyrometer temperature and up to five thermocouple temperatures. This system allowed the operator to continuously monitor experimental parameters while also providing a comprehensive history of each irradiation. Alarms were installed to alert the operator when experimental parameters moved outside acceptable limits.

Total seven batches of irradiation experiments were completed. The irradiations and the number and type of tensile samples (BWR or argon) irradiated were listed is Table 2-2. Four alloys (A, C, E and G) were selected for the first irradiation and subsequent interrupted straining test because they have a large spread in SFEs. Three irradiations were completed to doses of 5 dpa, 1 dpa and 5 dpa, respectively, for these four alloys using 3.2 MeV protons at Michigan Ion Beam Laboratory. The first irradiation was done on March 6, 2006. Four tensile samples for simulated BWR test and four TEM bars for TEM analysis were irradiated to a dose of 5 dpa. The sample temperature was maintained at 360±10ºC for the duration of the irradiation. The average dose rate was 8.2×10^{-6} dpa/s.

The second irradiation was completed on March 31, 2006. In this irradiation, four tensile samples and four TEM bars made from alloys A, C, E and G were irradiated to 1 dpa. The average dose rate for this irradiation was 8.7×10^{-6} dpa/s and the average irradiation temperature was 359.7 ºC±7.8ºC.

The third irradiation was completed on July 31, 2006. Four tensile samples from alloys A, C, E and G together with three TEM bars from alloys B, D and F were irradiated to 5 dpa. The irradiated tensile samples will be used for interrupted straining test in the argon environment. The average dose rate for this irradiation was 9.0×10^{-6} dpa/s and the average sample temperature during irradiation was 359.6 ºC±9.7ºC.

The fourth irradiation was done in December 2006. This irradiation was initiated on December 19, 2006 and completed on December 22, 2006. Due to the stability issue of the proton beam, the current on the stage was kept low (15 μA vs. 35 μA in previous experiments). The duration of the irradiation was almost doubled because of the low current. The sample temperatures were still able to be maintained at 360±10ºC for the duration of the irradiation. The average dose rate for this experiment was $\sim 4.6 \times 10^{-6}$ dpa/s.

During the year of 2007, some major parts of the accelerator were refurbished. The fifth radiation was completed in December 2007 using 2 MeV protons. The sixth and seventh irradiations were completed in February and May of 2008, respectively, and 2 MeV protons were used. A slightly high dose rate was used ~9.5×10^{-6} dpa/s for 2 MeV proton irradiations.

During each irradiation, the sample temperatures were monitored by a Stinger thermal imager. Temperatures of the upper, middle and lower part of a single sample were recorded by the Stinger software. The temperature distributions during the third irradiation for the four tensile samples are shown in Figure 2-4 as an example of the temperature control of the irradiations. In this case, 95.4% of the sampled temperatures are within the two dashed lines ($\pm 2\sigma$).

Table 2-2. Summary of irradiation experiments.

		5 dpa				1 dpa		
Alloy #	Nominal	Batch 1	Batch 2	Batch 6	Batch 7	Batch 3	Batch 4	Batch 5
A	18Cr8Ni	1 BWR	1 Argon			1 BWR	1 Argon	
B	18Cr12Ni			1 BWR 1 Argon				1 BWR 1 Argon
C	15Cr12Ni	1 BWR	1 Argon		1 PWR 1 BWR	1 BWR	1 Argon	
D	22Cr15Ni			1 BWR	1 Argon			1 BWR
E	13Cr15Ni	1 BWR	1 Argon			1 BWR	1 Argon	
F	18Cr25Ni			1 BWR 1 Argon				1 BWR 1 Argon
G	21Cr32Ni	1 BWR	1 Argon		1 PWR	1 BWR	1 Argon	

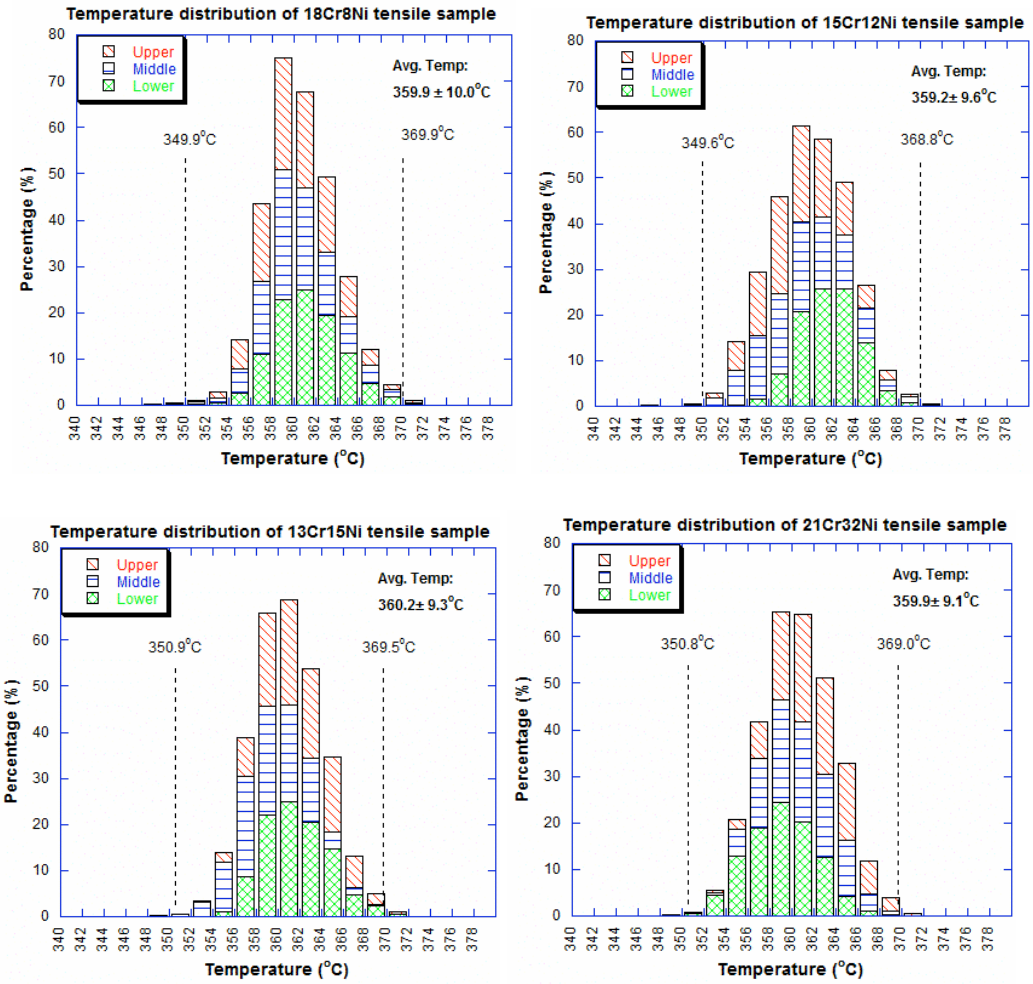

Figure 2-4. Temperature distribution on tensile samples of alloys A, C, E and G during irradiation with 3.2 MeV protons to 5 dpa at 360°C.

2.4 Dislocation and void microstructure analysis

Transmission electron microscopy (TEM) was conducted on irradiated samples of all heats. Three TEM disks were cut from each irradiated TEM bar. The unirradiated face of each bar was ground away using SiC paper (up to 1500 grit) to a thickness of ~150-200 μm. TEM disks were then cut from the bar using a South Bay Slurry Core-Drill cutter with a 3-mm ID brass core cutter and 600 grit SiC powder. Each disk was then polished to a thickness of ~100-160 μm using SiC paper (1200-4000 grit).

Final thinning to electron transparency was done using a Model 550D South Bay Single Jet Polisher. The jet-polish solution was a mixture of 5 vol% perchloric acid and 95 vol% methanol. The perchloric/methanol solution was cooled to –64°C. During polishing, the voltage was adjusted to maintain a constant current of 15-18 mA on the sample. Prior to jet-thinning irradiated TEM disks, the unirradiated disks from the same bar were thinned to test and adjust the thinning conditions, thus improving the quality of

the irradiated TEM disks. The irradiated face was jet polished for 10-15 seconds to remove any contamination layers that may have formed on the sample surface (an estimated 5 μm was removed). The sample was then thinned from the unirradiated face until perforation (typically 12-18 minutes). Following polishing, each sample was rinsed gently in acetone and methanol to remove any chemical residue on the sample surface.

TEM was used to characterize the dislocation microstructure, void population and to examine grain boundaries for evidence of second phases. The existence or absence of voids was determined by changing focus of the image at a condition where no strong diffraction is excited.

Bright field imaging was used initially for analysis. For bright-field imaging (BF), a two-beam condition at g=[200] (close to the <110> zone axis) was used. This condition revealed all the faulted dislocation loops (b=a0/3<111>) and 2/3 of perfect loops (b=a0/2<100>). Dislocation loops were most readily imaged in relatively thin regions of the TEM foil (50 to 100 nm thick). Further, only relatively flat areas of the foil with uniform thickness were used for dislocation loop analysis. Thickness and bend contours created by wedge-shaped or warped specimens, respectively, resulted in changing diffraction conditions within the same specimen area and made dislocation loop imaging more difficult. Most dislocation loop images were taken at magnifications of 100k-200k.

The rel-rod technique was also used to image faulted dislocation loops. It is convenient to image loops using the fine structure diffraction effects associated with the stacking faults within the loops. In thin foil electron microscopy, the reciprocal lattice points are elongated along the direction normal to foil surface forming “spikes”. The intersections of the reflecting sphere with the spikes produce single spots on the diffraction pattern. Lattice imperfections within the crystal affect the intensity distribution among the diffraction spots in the diffraction pattern. A planar defect structure in the crystal will form a spike oriented along the direction normal to the defect plane, its intersection with the reflecting sphere will then give rise to additional spots. The stacking faults within the Frank loops produce such fine structure effects on the diffraction patterns.

For an FCC lattice the stacking faults are present on all 4 sets of (111) planes at 70.5° relative to each other. As a result, 5 spikes are associated with any reflection in reciprocal space affected by all 4 sets of faults, one in the direction of the foil normal and 4 corresponding to the faulted plane normal. Such a reflection is the 002 in the kinematical region. The reflecting sphere intersects all 5 spikes and produces 5 spots at each 020 or 002 reflection on the diffraction pattern for a (100) projection with one of the (022) strongly excited in a 2-beam condition. When high resolution, dark field micrographs are taken using one of these satellite spots, the stacking faults with the loops lying in the corresponding (111) plane are revealed in strong contrast. These satellite spots can therefore be used to show the loop distribution on each of the 4 sets of (111) planes for loop density and size measurement. A very small objective aperture must be used so that only one satellite spot is used to form the dark field image.
Frank loops imaged near the <011> zone axis consist of two edge-on variants that can be used to form an edge-on loop image. The edge-on variant shown as a streak in the diffraction pattern is also called a “rel-rod”. By titling 8-10° from the <011> zone axis to

form a g=[113] 2-beam condition, the rel-rods from the Frank loops are strongly excited. Using dark-tilt to center one of the rel-rods to the optical center and using the smallest objective aperture to form a dark field image, the edge-on Frank loops are imaged as streaks oriented along the direction perpendicular to the direction of rel-rod streak in the diffraction pattern. Since the rel-rod image shows Frank loops only from one of the four planes, the number of loops measured must be multiplied by 4 to obtain the loop density. Rel-rod imaging provides higher resolution to show small faulted loops down to sizes around 1 nm in diameter. Due to the weak electron beam condition, longer exposure time was needed (~ 16 sec). Therefore, thermal drifting had to be minimized to ensure clear details in the picture.

2.5 Hardness measurement

Samples for hardness testing were mechanically wet-polished using SiC paper (grit 300-4000) and then electropolished for 30 seconds in a 90% perchloric acid and 10% methanol at – 40ºC. Microhardness was measured using a Vickers hardness indenter (MICROMET II) with a load of 25 g. A lower load was used to confine the plastic zone ahead of the indenter tip to a depth within the proton range (~40 μm) to ensure that unirradiated material was not being sampled. About 20 indents were made at each load condition. To evaluate the hardness changes due to irradiation, the hardness of the samples was measured at a load of 25 g before and after irradiation. For the hardness tester used, it was found that at a load of 25 g, the hardness measurements were in good agreement with results from PNNL measured with a load of 200 g for 316SS cold worked samples over the range of 150-450 Vickers hardness [19].

A total of 20 hardness indents were made for each irradiation condition. An average and standard deviation were determined for each condition. The hardness value of the unirradiated condition was subtracted from that of the irradiated condition to arrive at a hardness increase due to irradiation.

The yield strength of the proton-irradiated heats is a useful parameter for comparison of the effects of proton and neutron irradiation. While yield strength cannot be determined directly from the proton-irradiated samples, correlations have been developed which allow calculation of expected yield strength from dislocation microstructure or hardness. For austenitic alloys, the yield strength change associated with irradiation can be estimated using

$$\Delta\sigma_y = 3.03\,\Delta H_V \quad , \qquad (2\text{-}1)$$

where $\Delta\sigma_y$ is expressed in MPa and ΔH_v is expressed in kg/mm^2 [20]

2.6 Measurement of grain boundary chemistry

Grain boundary composition and composition profiles were measured via STEM/EDS using the Philips CM200/FEG TEM-STEM at the Oak Ridge National Laboratory on the same samples used for microstructure analysis. The CM200/FEG operates with an accelerating voltage of 200 kV and an incident beam size <1.4 nm (full-width at one tenth

maximum of the electron beam intensity). Spectral acquisition and analysis was done using EmiSpec ESVision microscope control and data analysis software. The Philips Compustage, room-temperature double-tilt specimen holder was used to minimize specimen drift during analysis. Microchemistry on heat F was measured using the JEOL 2010F instrument at the Electron Microbeam Analysis Laboratory at the University of Michigan. The 2010F operates at 200 kV with an incident beam size of ~0.9 nm FWHM (~1.1 FWTM). The smaller probe size will result in a slightly greater degree of segregation being measured as the amount of beam broadening is reduced.

Prior to analysis, samples were plasma cleaned using a Southbay PC150 plasma cleaner in both an argon and an oxygen plasma to minimize sample contamination during room-temperature analysis. Only grain boundaries aligned edge-on to the electron beam were analyzed and multiple measurements were taken on each grain boundary. In addition, composition profiles were taken at each grain boundary with measurements taken at 1.5 nm increments. Matrix compositions were taken in each grain (corresponding to the boundaries analyzed) at distances >50 nm from the boundary. Raw intensity data were then converted to weight percents using k-factors calculated for each grain (two per GB analyzed) by comparison of EDS-determined matrix intensities to the bulk alloy composition determined independently by electron microprobe analysis. The k-factors related the ratio of measured intensities for a pair of elements to the ratio of compositions for the same pair of elements. As a result, the measured matrix composition is equal to the bulk composition.

Grain boundary composition profiles and individual grain boundary measurements were taken from the irradiated conditions for all heats. Unfortunately, due to the relatively large grain size, the number of grain boundaries available for analysis was relatively small, and no more than four boundaries were analyzed on any single sample. During typical analysis of each grain boundary, five composition profiles were taken with 1.5 nm steps. In addition to the composition profiles, approximately five spot measurements were taken on each boundary, along with ten to twelve spot measurements of the matrix composition, which were used to determine k-factors. Finally, a matrix composition was taken as an area scan at low magnifications for each grain. The area scans were taken to ensure that the spot matrix measurements (and hence k-factors) did not contain artifacts due to local variations in the matrix composition. A "hole-count" was also taken for each grain boundary to quantify the EDS signal generated by interactions between the electron beam and the microscope or specimen holder and not the sample.

2.7 SCC experiments and autoclave system

The constant extension rate stress corrosion tests were conducted in a multiple-specimen CERT test system, supplied by CorTest. The CorTest system is capable of straining four samples in parallel providing identical conditions within a given test. A schematic of this system is shown in Figure 2-5. The CERT setup consists of an autoclave capable of sustaining pressures up to 3000 psi (20.7 MPa) and temperatures up to 340°C, a load frame, and a computer driven, 30 kN (6750 pound) load train for straining of the samples. The grade-2, commercial-purity, titanium autoclave has a capacity of 1.8 liters and is sealed using deformable stainless steel o-rings.

CERT tests were performed in normal oxygenated BWR water chemistry (NWC) and in a simulated PWR environment. NWC conditions used in this study are specified in Table 2-3. The test conditions for NWC were selected to achieve maximum discrimination of SCC susceptibility [22]. Thus, the conductivity and oxygen composition were selected to arrive at a value of the corrosion potential of about +150 mV_{SHE}. [23] This potential is in the regime where the sensitivity to material condition is greatest [22].

Test temperature was controlled by a series of resistance heater bands outside the autoclave. An internal type K thermocouple, positioned next to the samples, was used to monitor the water temperature. Water temperature and pressure were measured to ±1°C and ±100 psi, respectively. For the NWC condition, the dissolved oxygen concentration was controlled at 2 ppm by bubbling a 5% O_2/Ar mixture through the glass mixing column with a 15 psi overpressure, as shown in Fig. 2-5. Conductivity was controlled via automatic additions of dilute H_2SO_4 (3×10^{-6} N) so that the outlet conductivity was maintained at 0.2 μS/cm. For the PWR condition, the dissolved oxygen content was maintained below 5 ppb by continuous sparging of pure H2 through the glass-mixing column with a 1 atm overpressure. Boric acid and LiOH were carefully added to the mixing columns to yield B and Li contents of 1000 and 2 ppm, respectively. Experimental parameters were tracked continuously during the CERT test using a PC-based monitoring system. The data acquisition system included an upgraded computer, an analogue to digital (A-D) board, and a multiplexor signal conditioning board. Water temperature, system pressure, water conductivity, load for each sample, and extension were all monitored and recorded every 1000 sec.

Table 2-3: Constant extension rate tensile (CERT) test conditions

Parameter	NWC
Temperature	288°C
Extension rate*	3.5×10^{-7} s^{-1}
pH (28°C)	6.0
Outlet Conductivity	0.2 μS/cm
O_2 concentration	2000 ppb
Corrosion potential (SHE)	+160 mV

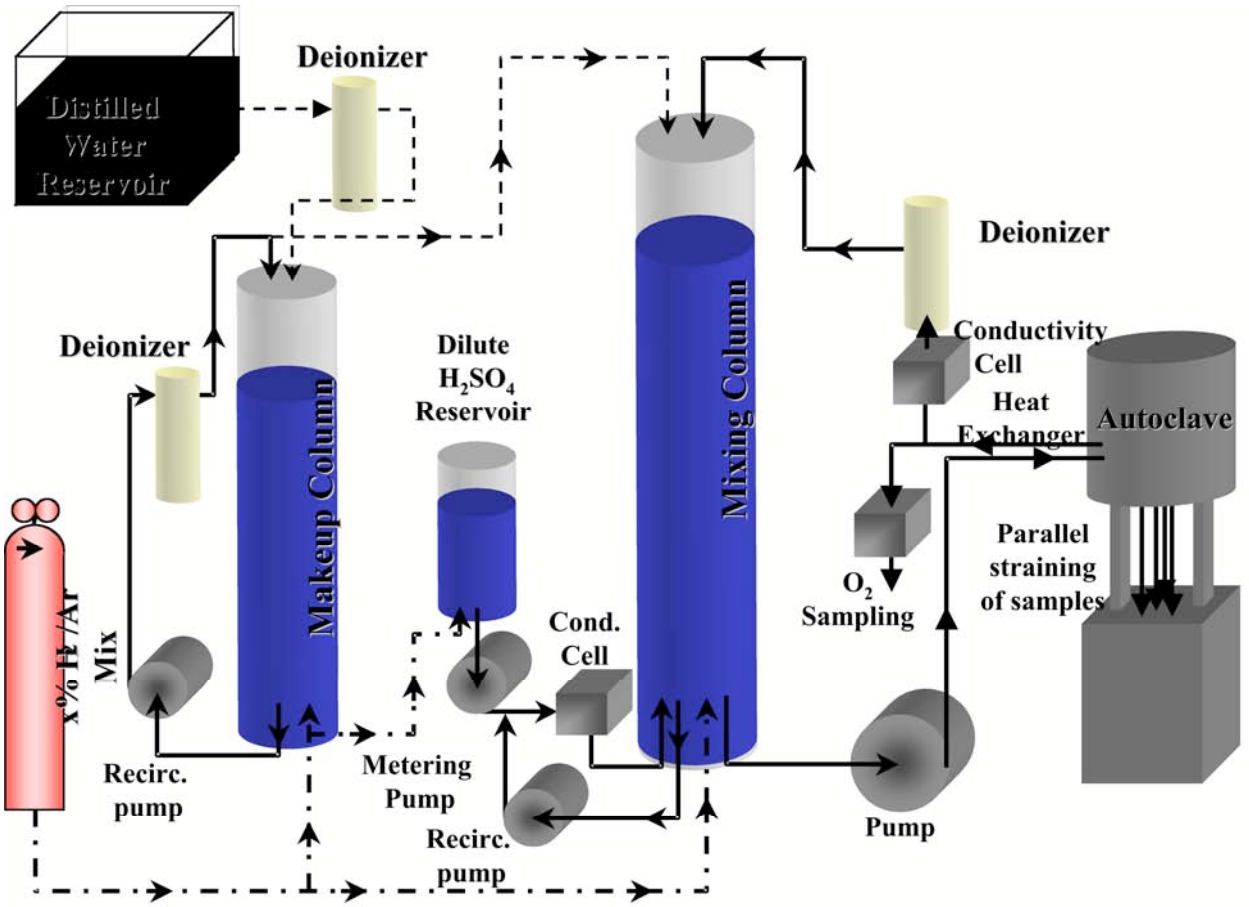

Figure 2-5: Schematic of CorTest system for constant extension rate tests (CERT) of multiple specimens.

2.8 Localized deformation

Dislocation channeling is the primary plastic deformation mode for the tested alloys. The slip channels in the irradiated austenitic alloys are much pronounced than unirradiated alloys as shown in Figure 2-6

The tools used for characterization of dislocation channels are show in Figure 2-7. At each strain step, the surfaces of the irradiated and strained samples were investigated using SEM (for channel spacing) and atomic force microscopy (for channel width and height). Channel spacing was measured using SEM. Images were taken at magnifications of ~ 500x and the distance between channels was measured.

A replica of the specimen surface was also prepared from the strained samples. The replicas provide a smaller specimen, which is better suited for AFM analysis and a durable archive of the specimen surface at each strain increment. The replicas were made using Microset replica kits. To make replicas out the tensile samples, a small amount of Microset 101TH synthetic rubber replicating compound was put on the Microset backing paper. An area of 10 cm x 20 cm was sufficient for 4 tensile samples. The thickness of the compound was about a few millimeters. The tensile samples were put on the compound with the irradiated surface facing downward. No force was applied on the samples and they were settled by their weight. The compound was cured after ~ 1 hour but it was usually left overnight. Once the replicating compound was cured, the samples were removed carefully and a negative copy of the deformed surface was left on the cured compound. To make a positive copy of the deformed surface, the replica with a negative copy of the deformed surface was used as a mold and a copy of the replica was made. The replica of the replica with a negative copy had a positive copy of the deformed surface. The reproduction of the sample surface is a key factor in using replicas for surface analysis. The replica must accurately reproduce the surface in order to be a valid technique. The surface of the sample and replica from alloy B are compared in Figure 2-8. Clearly, the features of the sample are preserved in the replica as viewed with both SEM and AFM.

The Atomic force microscopy (AFM) was performed on the Digital Instruments Nanoprobe IIIa Phase Atomic Force Microscope to measure channel height and width. The AFM was used in tapping mode, and a nano-device rotated the tapping-mode etched silicon probes. The probes have a nominal tip radius of curvature smaller than 10 nm. A frequency oscillation of 200 kHz was used, and the scanned area was set to be about $50 \times 50\ \mu m^2$. The profiles of the slip steps were determined using the Nanoprobe software. A AFM with the measurements is shown in Figure 2-9.

The degree of localization can be characterized by several unique quantities. However, dislocation channel height which correlates to the number of dislocations in the channels is believed to be the most important character of dislocation channels. During deformation, the crystal will relieve the applied stress by slipping along the slip planes. Moving dislocations would end at grain boundaries or at free surfaces and produce slip steps in the amounts equal to a multiple of the unit dislocation displacement vector, Burgers vector **b**. This Burgers vector defines the magnitude and direction of the slip steps made by dislocations. Therefore the number of the Burgers vectors (n_d) in the slip step is proportional to the channel height.

Channels with largest steps are more likely to initiate cracks when they intersect grain boundaries. Weighted average channel height which uses step height itself as weight is a better choice than the mathematic average. Using weighted average channel height, larger channels are put more weights as shown in Eq. 2-2. As shown in Figure 2-10, the weighted average channel height is generally larger than the mathematic average.

$$\bar{h} = \frac{\sum_{i=1}^{n} h_i^2}{\sum_{i=1}^{n} h_i} \qquad (2\text{-}2)$$

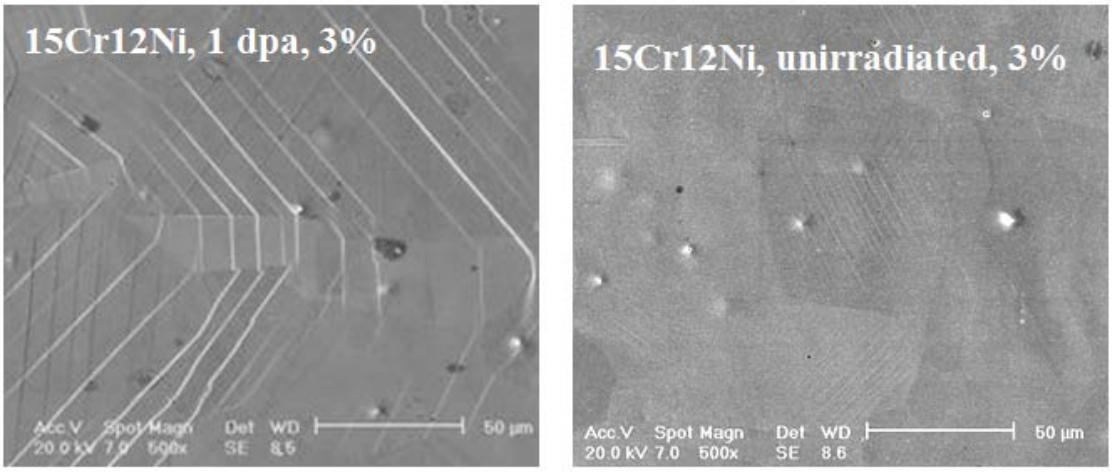

Figure 2-6: Dislocation channels in irradiated (left) and unirradiated alloy 15Cr12Ni strained to 3% in argon. The left sample was irradiated to 1 dpa at 360ºC.

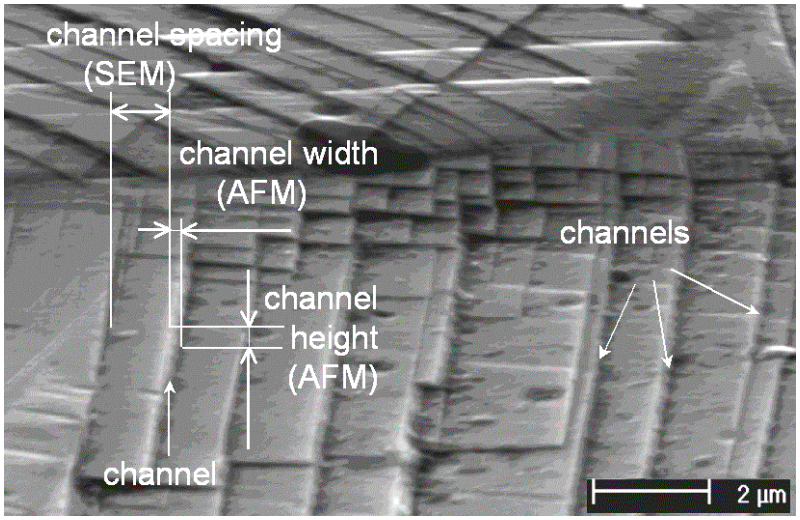

Figure 2-7: SEM image of Fe-Cr-Ni alloy irradiated to 1.0 dpa at 360ºC and strained to 12% at 288ºC in argon.

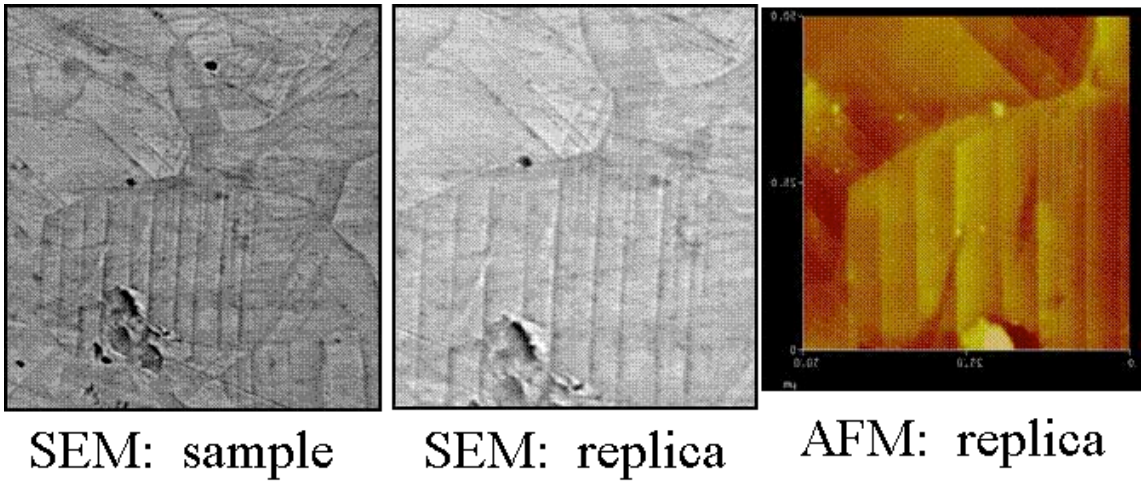

Figure 2-8: Comparison of surface features on sample (left) with the surface features of a replica in both SEM (center) and AFM (right).

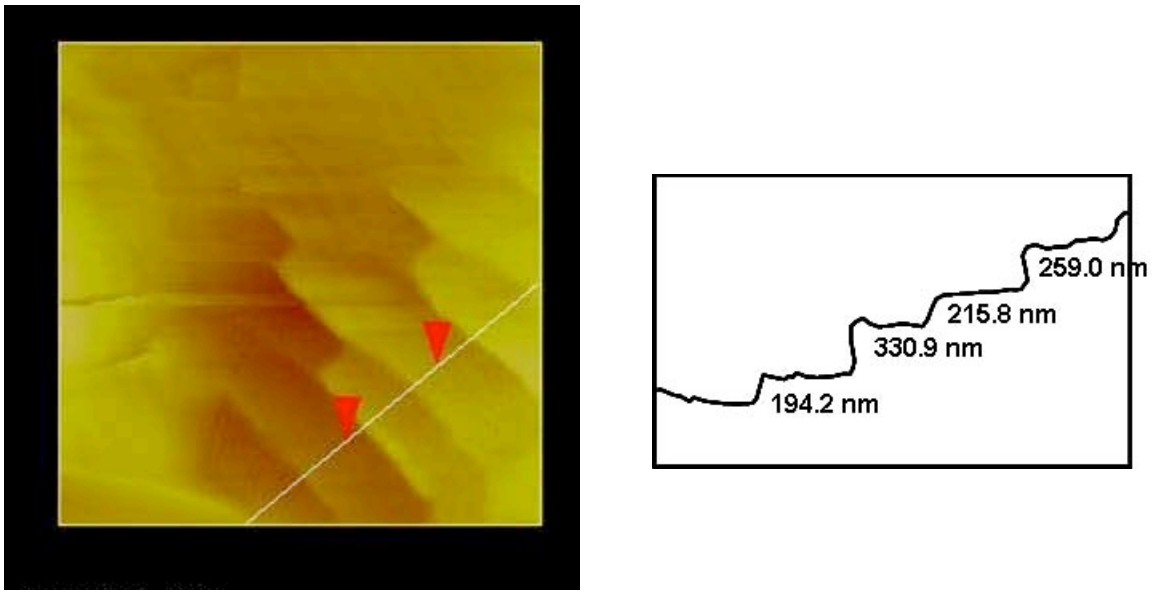

Figure 2-9: Channel height as measured using AFM in alloy Fe-Cr-Ni alloy irradiated to 5 dpa at 360ºC and strained to 3% in argon at 288ºC.

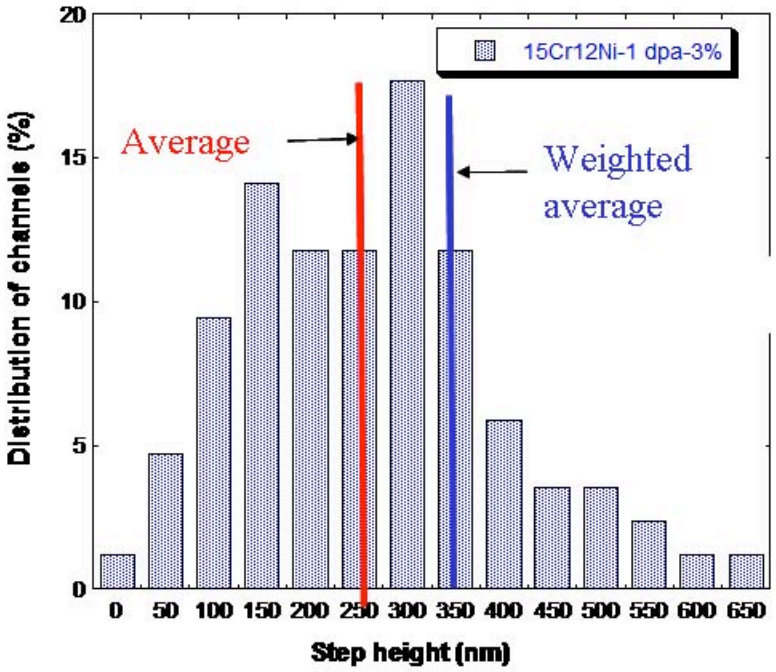

Figure 2-10: A comparison of average channel height with weighted average channel height in alloy C irradiated to 1 dpa at 360ºC and strained to 3% at 288ºC in argon.

3. Results

The results of experimental analysis on the seven alloys irradiated with protons to 1 and 5 dpa at 360°C are presented in this chapter. Measured SFE and hardening and calculated changes to yield stress are presented first followed by the characterization of dislocation loops and voids for all the alloys. Radiation-induced segregation has also been measured for several alloys at selected conditions. Finally, localized deformation results from tests in argon and cracking susceptibility results from CERT tests in BWR environments are presented.

3.1 Measurement of stacking fault energy

As the predicted stacking fault energies may deviate from the real values in the alloys, it is important to verify the SFEs of the selected alloys. The most straightforward method of measuring stack fault energy in an alloy is to measure the separation of dislocation partials. In an f.c.c. SFE alloy, a perfect dislocation (b=1/2<110>) dissociates into two partial dislocations (b=1/6<112>) on {111} planes. The spacing of the two dislocation partials (d) at equilibrium is inversely proportional to stacking fault energy (γ) as shown in the equation:

$$d = \frac{Gb^2}{8\pi} * \frac{2-\nu}{1-\nu} * (1 - \frac{2\nu\cos 2\beta}{2-\nu}) * \frac{1}{\gamma} \quad (3\text{-}1)$$

where G is the shear modulus (74 GPa) and ***b*** is the Burger's vector (0.15 nm), ν Poisson's ration (0.33) and β is the angle between dislocation line and Burger's vector.

For edge dislocations, $\beta = 90^{o}$ and the equation changes to:

$$d = \frac{Gb^2}{8\pi} * \frac{2+\nu}{1-\nu} * \frac{1}{\gamma} \quad (3\text{-}2)$$

For screw dislocations, $\beta = 0^{o}$ and the equation changes to:

$$d = \frac{Gb^2}{8\pi} * \frac{2-3\nu}{1-\nu} * \frac{1}{\gamma} \quad (3\text{-}3)$$

Ideally, pure edge dislocations ill give the largest separation between partials for the same SFE and therefore are preferred. However, dislocations in the studied alloys generally have mixed characters. Assume $\beta = 45^{o}$, the equation changes to

$$d = \frac{Gb^2}{4\pi} * \frac{1}{\gamma} \quad (3\text{-}4)$$

This is the equation generally used for calculated SFE [21].

In order to measure the SFE, 3 mm TEM disks were cut from each alloy and they were subsequently mechanically thinned to 100 μm. They were then electropolished in a jet-thinner to get proper TEM foils. The TEM measurements were performed using a JOEL 2010F transmission electron microscopy at the University of Michigan Electron Microbeam Analysis Laboratory (EMAL). Only isolated dislocations which are at least 100 nm away from others were selected for measurement. The selected dislocations were imaged using g/3g weak beam dark field technique (WBDF) on {110} planes. Some WBDF photographs showing dislocation dissociation in various alloys are presented in Figure 3-1. 10-25 measurements were made on each alloy. The measured separation between partials and calculated SFEs are listed in Table 3-1. The measured values are typically as expected.

Table 3-1. Summary of dislocation partial separation and calculated SFE.

Alloy	Number of meas.	Separation between partials *d* (nm)	SFE (mJ/m^2)
A	20	9.3±1.3	15.5±2.8
B	10	7.0±1.2	19.7±4.1
C	15	4.8±0.3	28.0±2.0
D	10	3.4±0.3	38.2±2.4
E	15	3.6±0.4	36.3±2.1
F	25	2.8±0.1	47.1±1.7
G	25	2.2±0.2	61.1±5.8

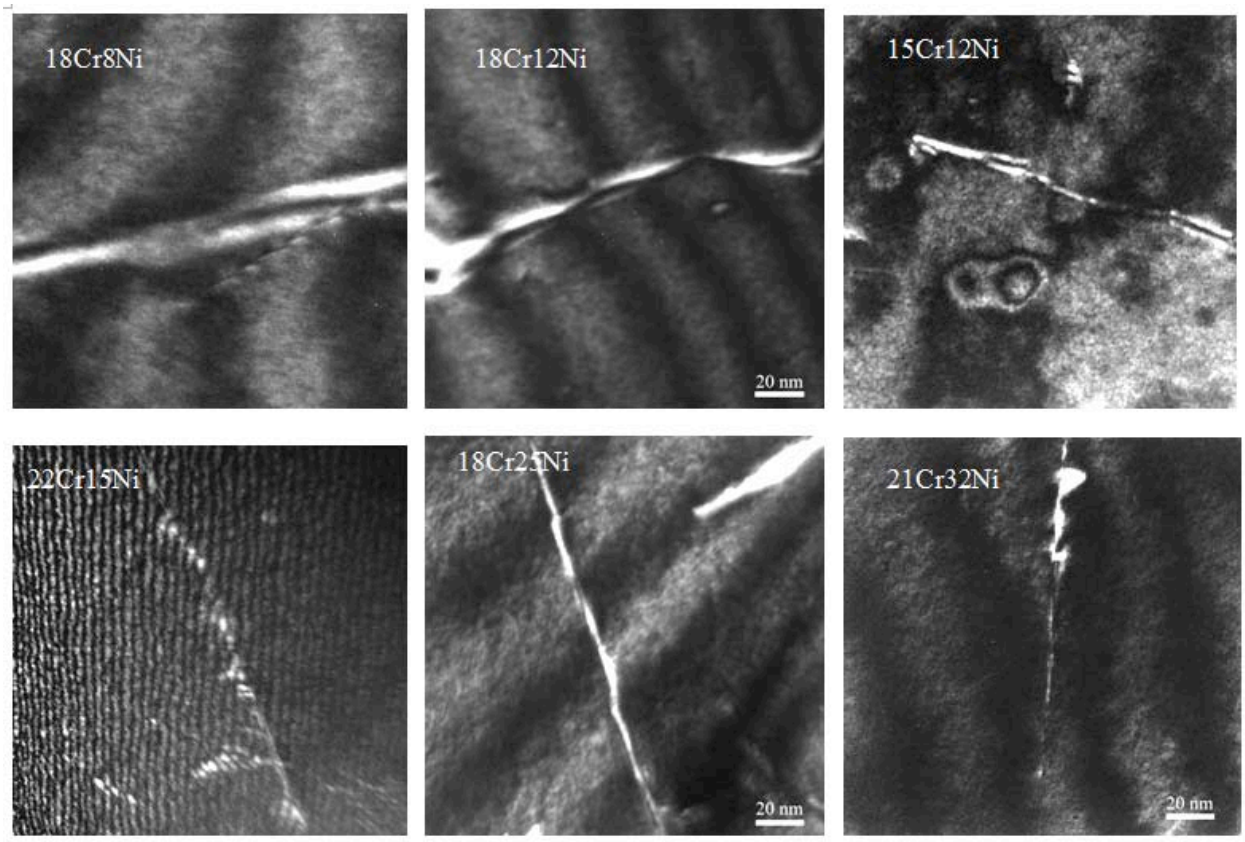

Figure 3-1: Weak beam dark field images showing dissociation of dislocations in alloys studied.

3.2 Hardness

Hardness was measured for all alloys after proton irradiation to 1 and 5 dpa and the results are summarized in Table 3-2. The measured hardness, before and after irradiation for each alloy are also compared in Figure 3-2. Hardness increased to approximately the same level for alloys C, E F, and G following irradiation to 1 dpa and corresponds to an increase of approximately 90-100 kg/mm^2. The increase in hardness for alloys B and D was only 60-70 kg/mm^2. Alloy A has a moderate increase in hardness (80 kg/mm^2) but its hardness after irradiation is the greatest (267 kg/mm^2). After 5 dpa irradiation, the hardness for alloys B-G is comparable while the commercial grade alloy A still has the greatest hardness.

The yield strength of the proton-irradiated heats is also a useful parameter in the radiation materials community. The yield strength change associated with irradiation can be estimated as discussed in session 2.5. Using Eq (2-1), the change in yield stress was calculated for each of the seven alloys irradiated to 1 and 5 dpa. The results are also listed in Table 3-2. The yield stress calculated from the change in hardness is plotted in Figure 3-3 for all alloys.

Table 3-2: Summary of hardness results and calculated yield strengths.

Alloy	Dose (dpa)	Unirradiated hardness (kg/mm^2)	Irradiated hardness (kg/mm^2)	Change in hardness (kg/mm^2)	Calculated Change in yield stress (MPa)*
A	1	187.0±5.8	266.8±14.5	79.0±15.6	239.4
	5	184.1±8.3	363.0±21.9	178.8±23.4	541.8
B	1	150.0±2.0	213.4±12.5	63.4±12.7	192.1
	5	145.3±6.4	314.5±11.7	169.2±13.3	512.7
C	1	137.7±5.6	231.9±12.7	94.2±13.9	285.4
	5	130.8±6.2	301.3±14.6	170.5±15.9	516.6
D	1	135.2±3.8	206.4±14.8	71.2±15.3	215.7
	5	140.4±7.6	321.3±14.1	180.9±16	548.1
E	1	137.2±6.3	238.8±12.2	101.6±13.7	307.8
	5	132.2±6.7	327.9±16.0	195.4±17.3	592.1
F	1	153.1±10.1	246.3±9.4	93.2±13.8	282.4
	5	134.0±4.4	329.8±10.3	195.8±11.2	593.3
G	1	145.6±6.5	243.7±17.3	98.1±18.5	297.2
	5	134.1±5.6	338.3±22.8	204.2±23.5	618.7

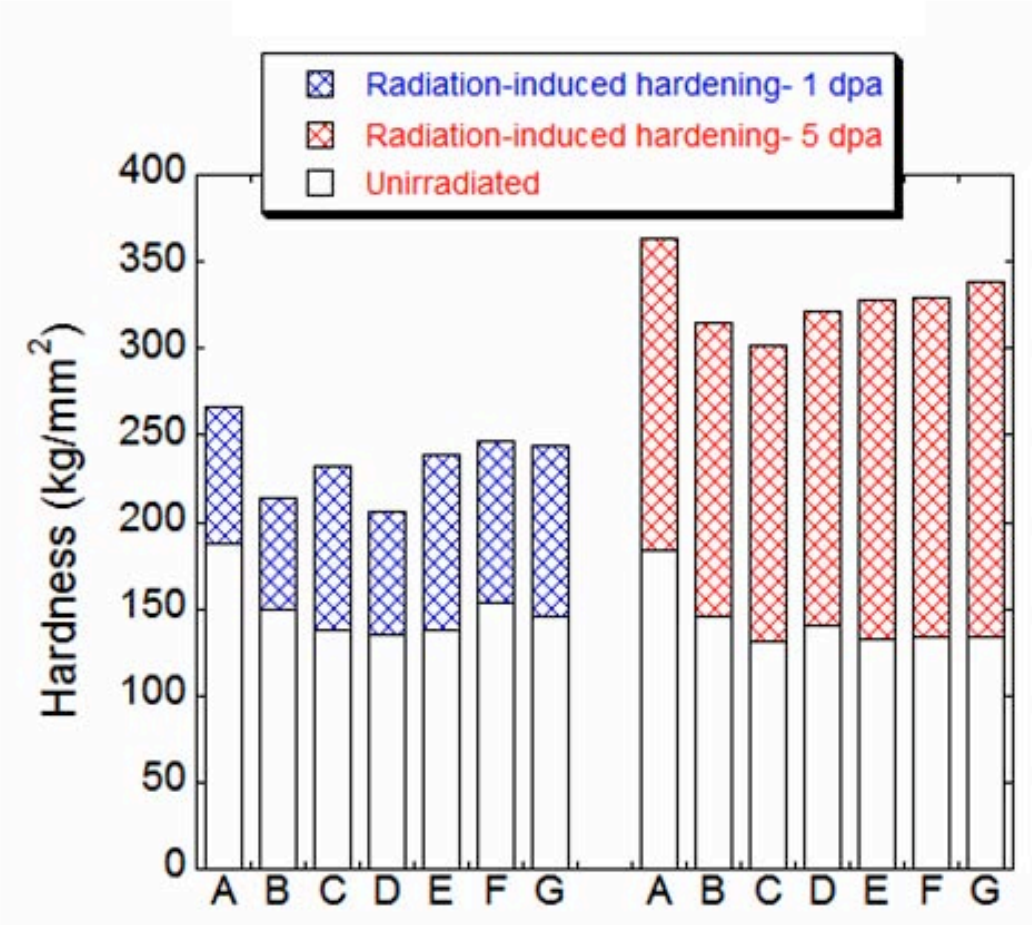

Figure 3-2: Hardness measured before and after irradiation with protons at 360°C to 1 and 5 dpa.

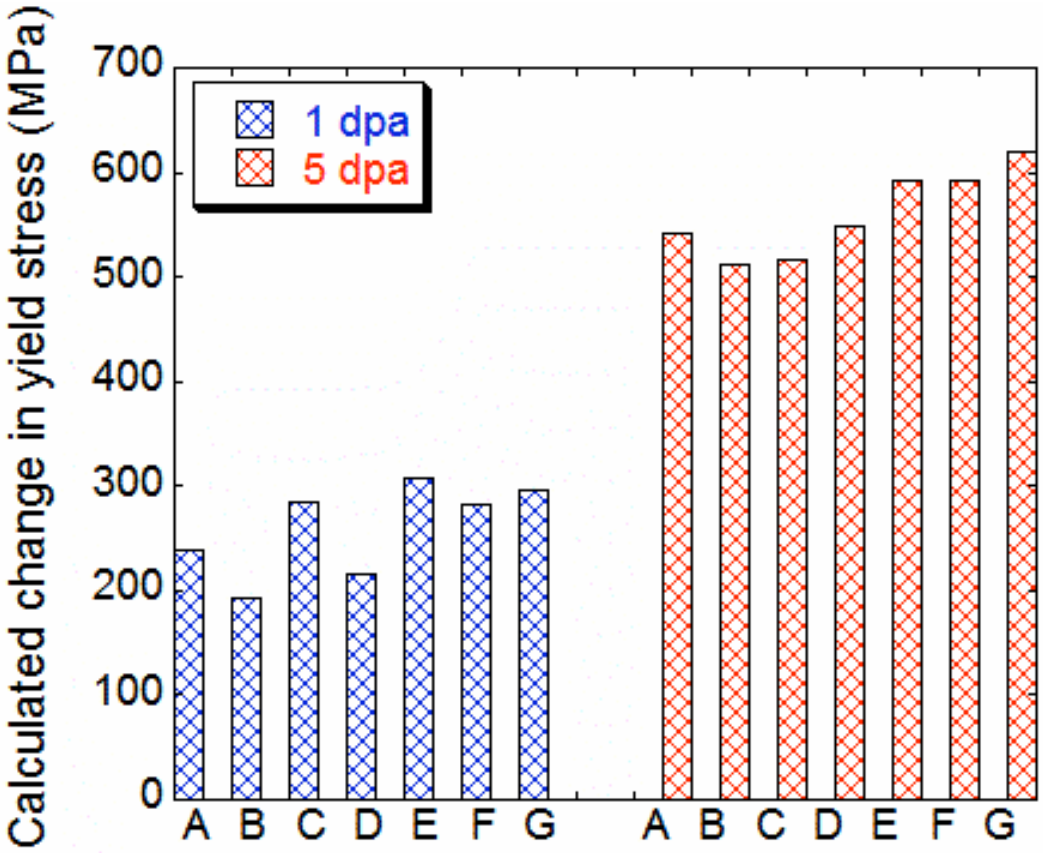

Figure 3-3: Change in yield stress and as-irradiated yield stress, calculated from hardness measurements for all solute addition alloys irradiated with protons at 360°C to 1 and 5 dpa.

3.3 Microstructure

3.3.1 Dislocation Loops

Dislocation loops were observed in all samples. The dark-field images for each of the seven alloys at 1 and 5 dpa are shown in Figure 3-4. The mean loop size and density are summarized in Table 3-3, along with the total number of loops characterized. The loop size and density are compared in Figure 3-5 for each alloy. The mean loop diameters were similar in alloys B, C, D and E, all around 7 nm at 1 dpa and 8 nm at 5 dpa. Larger loops were measured in alloys F and G (8.7 and 7.9 nm, respectively at 1 dpa and 10.9 and 9.8 nm, respectively at 5 dpa) and smaller loops in the commercial grade alloy A (3.6 nm at 1 dpa and 5.7 nm at 5 dpa). Loop densities ranged from 1.1 x 10^{22} m^{-3} in alloy F to 2.4 x 10^{22} m^{-3} in heat E at 1 dpa and 2.0 x 10^{22} in alloy G to 3.9 x 10^{22} m^{-3} in heat D

at 5 dpa in high purity alloys. The loop density is significantly higher in the commercial grade alloy A for both doses.

Table 3-3: Summary of dislocation loop analysis results.

Dose	Alloy	Number of Loops Imaged	Loop Diameter (nm)	Loop Density (10^{22} m^{-3})
1 dpa	A	188	3.6±0.1	3.20±0.30
	B	176	7.1±0.2	1.05±0.08
	C	174	6.6±0.3	2.22±0.32
	D	113	7.3±0.4	0.81±0.07
	E	80	6.9±0.3	2.40±0.30
	F	122	8.7±0.4	1.09±0.08
	G	163	7.9±0.5	1.89±0.20
5 dpa	A	183	5.7±0.2	6.81±0.80
	B	440	7.4±0.2	3.03±0.19
	C	237	7.8±0.3	2.72±0.20
	D	457	8.2±0.2	3.95±0.60
	E	207	8.2±0.2	2.88±0.29
	F	491	10.9±0.2	3.52±0.53
	G	164	9.8±0.6	1.99±0.30

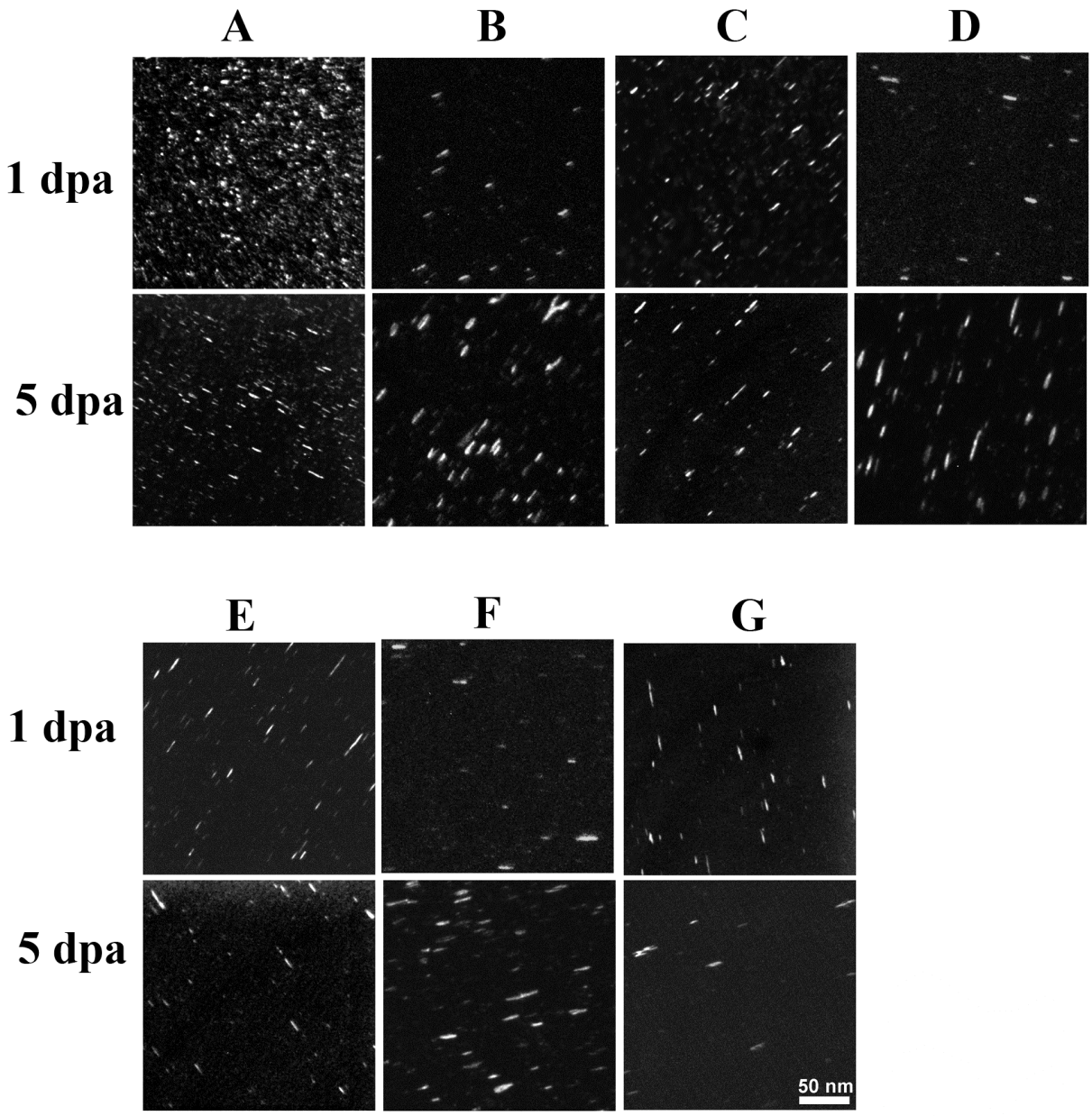

Figure 3-4: Rel-rod image of faulted dislocation loops in alloy A-G irradiated to 1 and 5 dpa at 360ºC.

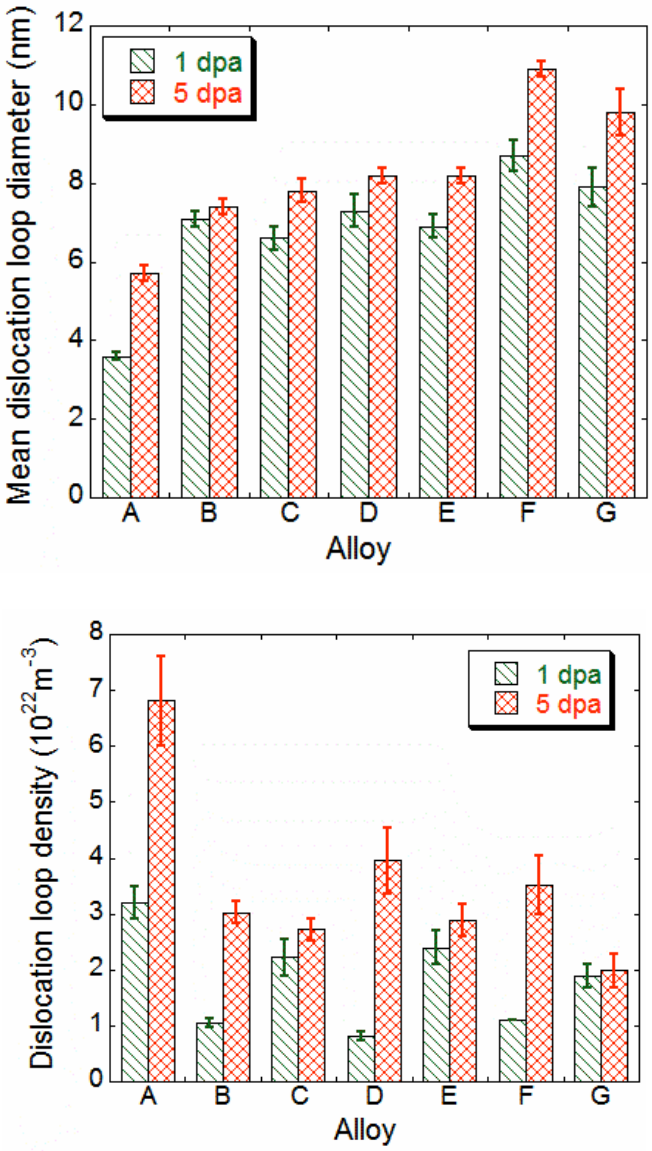

Figure 3-5: Mean dislocation loop diameter (top) and loop density (bottom) in alloy A-G irradiated to 1 and 5 dpa at 360ºC.

3.3.2 Voids

Low density of voids was observed in alloys B, D and E at 1 dpa. Voids were observed in all alloys but alloy at 5 dpa. Figure 3-6 are bright filed TEM images showing voids

observed in some of the alloys. A comparison of void size and density is shown in Figure 3-7. The mean void diameter, density and swelling calculated from the mean diameters and densities are summarized in Table 3-4. The Largest void size and highest density of voids were observed in alloy B at both doses. Swelling is the greatest in alloy B (0.079%) followed by alloys D (0.041) and G (0.036%). A comparison of swelling among alloys is shown in Figure 3-8.

Table 3-4: Summary of void size, density and swelling in each alloy.

Dose	Alloy	Number of voids Imaged	Void Diameter (nm)	Void Density (10^{22} m^{-3})	Swelling (%)
1 dpa	A	-			
	B	63	3.4	0.11	0.002
	C	-			
	D	-	2.5	<0.1	<0.001
	E	-	3.0	<0.01	<0.001
	F	-			
	G	-			
5 dpa	A	-			
	B	86	5.8	0.77	0.079
	C	16	3.2	0.37	0.006
	D	20	3.9	1.32	0.041
	E	15	2.5	0.41	0.003
	F	18	4.8	0.03	0.002
	G	40	4.2	0.93	0.036

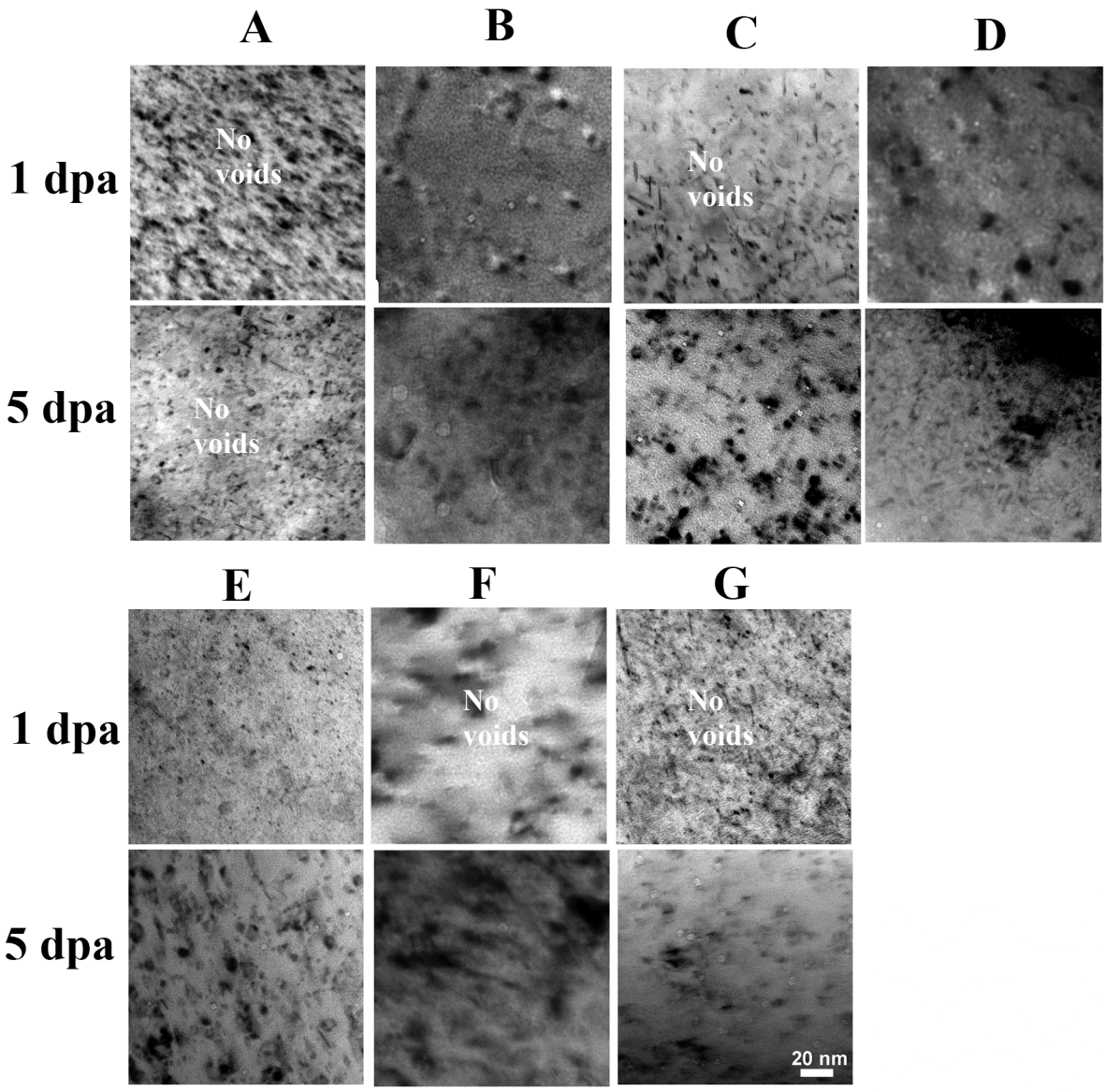

Figure 3-6: TEM bright field images showing voids in some of the alloys irradiated to 1 and 5 dpa at 360ºC.

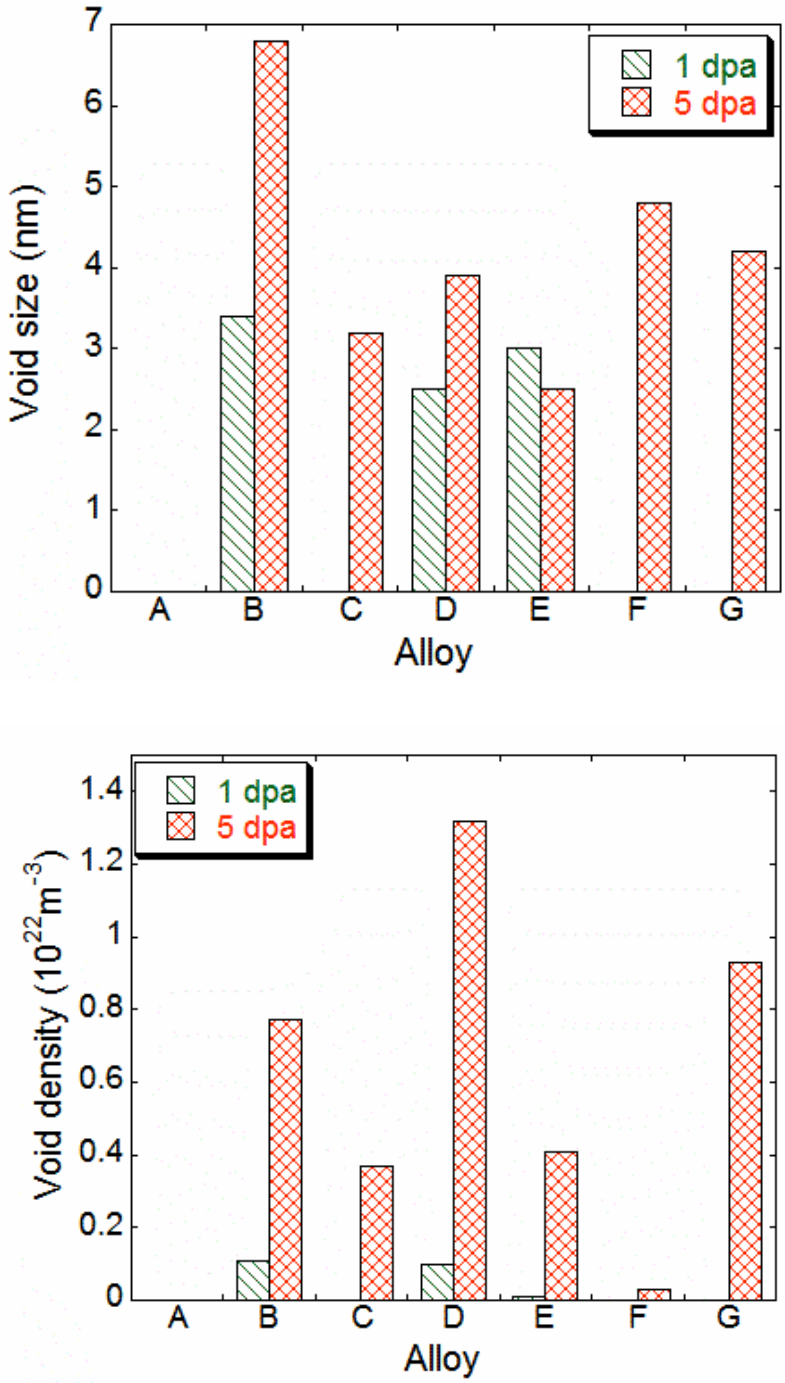

Figure 3-7: Mean void size (top) and density (bottom) in alloys A-G irradiated to 1 and 5 dpa at 360ºC.

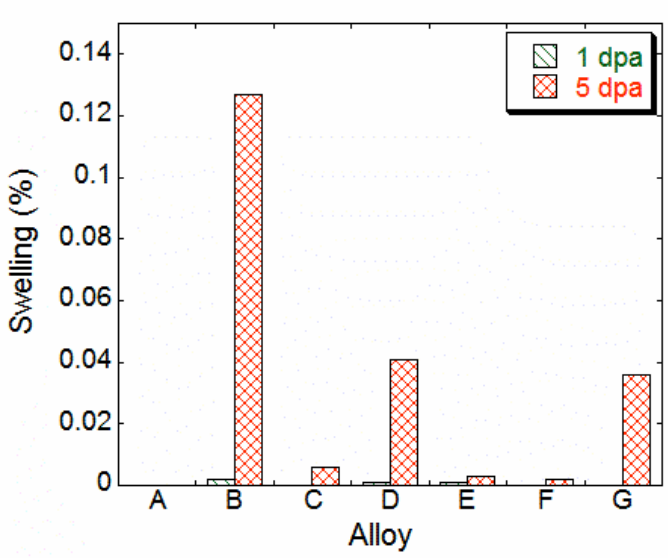

Figure 3-8: A comparison of swelling in alloys A-G irradiated to 1 and 5 dpa at 360ºC.

3.4 Microchemistry

Table 3-5 summarizes the results of the measurements for alloys A, C and E irradiated to 1 dpa with protons at 360°C. Table 3-5 summarizes the results of the measurements for alloys A-G irradiated to 5 dpa. The uncertainties listed in Tables 3-4 and 3-5 represent the standard deviation of the mean associated with the measurement. Only the major constituents were quantified in high purity alloys (B-G). Si was quantified in commercial alloy A. No detectable amount of S or P was measured at the grain boundary for all alloys.

Segregation profiles for Cr and Ni for alloys C and E at 1 dpa are shown in Figure 3-9 and those for all alloys at 5 dpa are shown in Figures 3-10. The peak heights vary from alloy to alloy but the peak widths are similar and the FWHM (full width at half maximum) are all within 5 nm.

The grain boundary Cr content for examined alloys at 1 and 5 dpa is shown in Figure 3-11. The grain boundary Cr content is the highest in alloy D and the lowest in alloy C and E. The grain boundary Cr content shows some degree of dependence on the bulk Cr content since alloy D has the highest bulk Cr (22 wt%) and alloy C and E have the lowest bulk Cr content (15 wt% and 13 wt%, respectively). The change from bulk Cr composition for each of the irradiated alloys is shown in Figure 3-12. All alloys but A at 1 dpa show the depletion of Cr at grain boundaries. The higher-than-bulk Cr content at grain boundary is due to the initial enrichment of Cr prior to irradiation. The grain boundary Cr continued to decrease with dose and at 5 dpa the grain boundary Cr is lower than the bulk content by 2.3 wt%. Alloy F and G have a larger degree of Cr depletion than other alloys. Alloy E, which has the lowest bulk Cr content, shows the lowest level of depletion.

The grain boundary Fe content is at or near the bulk content for alloys B, C, D and E while alloys F and G have significant Fe depletion (Figure 3-13). The enrichment of Ni at grain boundaries was observed at all examined conditions and alloy F and G have the highest grain boundary Ni content probably due to the high bulk Ni content (Figure 3-14).

Table 3-5: Summary of grain boundary composition measurements for alloys A, C and E irradiated to 1 dpa at 360°C.

Alloy	Fe	Cr	Ni	Mn	Si
A matrix/bulk comp.	71.04	18.3	8.5	1.38	0.65
A – 1 dpa					
Avg. GB comp. (wt%)	68.8	18.8	9.3	1.1	1.1
Deviation from bulk	-2.24	0.5	0.8	-0.28	0.45
Number of GB/meas.	2/25				
Std. Dev. of mean (wt%)	0.2	0.2	0.1	0.05	0.02
C matrix/bulk comp.	71.1	15.76	12.04	0.98	
C – 1 dpa					
Avg. GB comp. (wt%)	70.31	13.26	15.40	0.89	
Deviation from bulk	-0.79	-2.5	2.36	-0.09	
Number of GB/meas.	1/7				
Std. Dev. of mean (wt%)	0.3	0.2	0.3	0.1	
E matrix/bulk comp.	70.4	13.41	15.04	1.03	
E – 1 dpa					
Avg. GB comp. (wt%)	70.28	12.3	16.3	1.0	
Deviation from bulk	-0.12	-1.11	1.26	-0.03	
Number of GB/meas.	2/9				
Std. Dev. Of mean (wt%)	0.2	0.1	0.2	0.1	

Table 3-5: Summary of grain boundary composition measurements for alloys A-G irradiated to 5 dpa at 360°C.

Alloy	Fe	Cr	Ni	Mn	Si
A matrix/bulk comp.	71.04	18.3	8.5	1.38	0.65
A – 5 dpa					
Avg. GB comp. (wt%)	68.9	15.99	11.65	1.06	1.86
Deviation from bulk	-2.14	-2.31	3.15	-0.32	1.21
Number of GB/ meas.			2/8		
Std. Dev. Of mean (wt%)	0.4	0.3	0.4	0.2	0.3
B matrix/bulk comp.	67.8	18.8	12.4	0.9	
B – 5 dpa					
Avg. GB comp. (wt%)	67.9	16.1	15.2	0.8	
Deviation from bulk	0.1	-2.7	2.8	-0.1	
Number of GB/meas.			2/12		
Std. Dev. of mean (wt%)	0.3	0.3	0.1	0.1	
C matrix/bulk comp.	71.1	15.76	12.04	0.98	
C – 5 dpa					
Avg. GB comp. (wt%)	70.36	12.18	15.86	1.4	
Deviation from bulk	-0.74	-3.58	3.82	0.42	
Number of GB/meas.			1/7		
Std. Dev. of mean (wt%)	0.5	0.4	0.7	0.1	
D matrix/bulk comp.	61.98	22	15	1	
D – 5 dpa					
Avg. GB comp. (wt%)	61.88	19.28	17.5	1.2	
Deviation from bulk	0.1	-2.72	2.5	0.2	
Number of GB/meas.			2/8		
Std. Dev. of mean (wt%)	0.3	0.3	0.2	0.1	
E matrix/bulk comp.	70.4	13.41	15.04	1.03	
E – 5 dpa					
Avg. GB comp. (wt%)	69.06	12.36	17.32	1.2	
Deviation from bulk	-1.34	-1.05	2.28	0.17	

Number of GB/meas.	1/7				
Std. Dev. of mean (wt%)	0.2	0.4	0.2	0.1	
F matrix/bulk comp.	55.6	18.2	25.1	1.0	
F – 5 dpa					
Avg. GB comp. (wt%)	50.0	13.5	36.0	0.5	
Deviation from bulk	-4.4	-4.7	10.9	-0.5	
Number of meas.	21	21	21	21	
Std. Dev. of mean (wt%)	0.7	0.5	0.9	0.1	
G matrix/bulk comp.	47.01	20.73	31.16	0.94	
G – 5 dpa					
Avg. GB comp. (wt%)	43.44	16.57	39.09	0.77	
Deviation from bulk	-3.57	-4.16	7.93	-0.17	
Number of GB/meas.	2/11				
Std. Dev. of mean (wt%)	0.6	0.2	0.6	0.1	

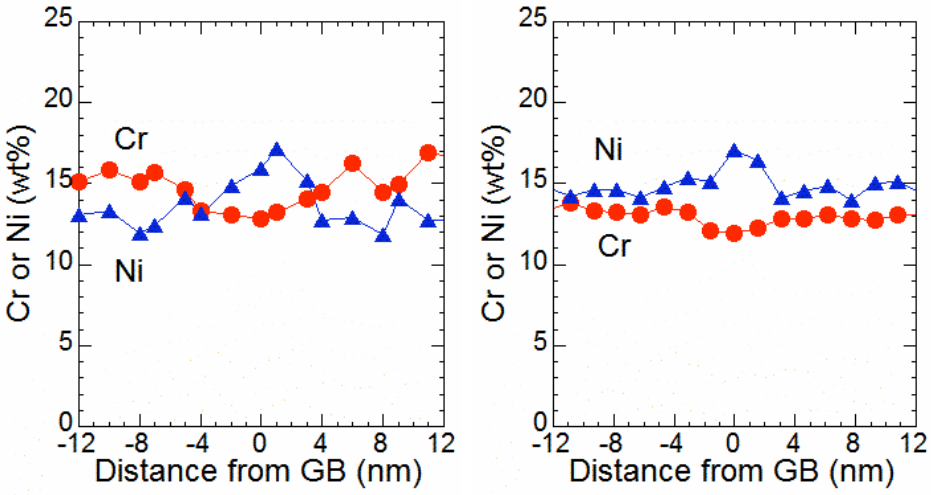

Figure 3-9: Cr and Ni grain boundary segregation profiles for all alloys C and E, proton-irradiated to 1 dpa at 360°C.

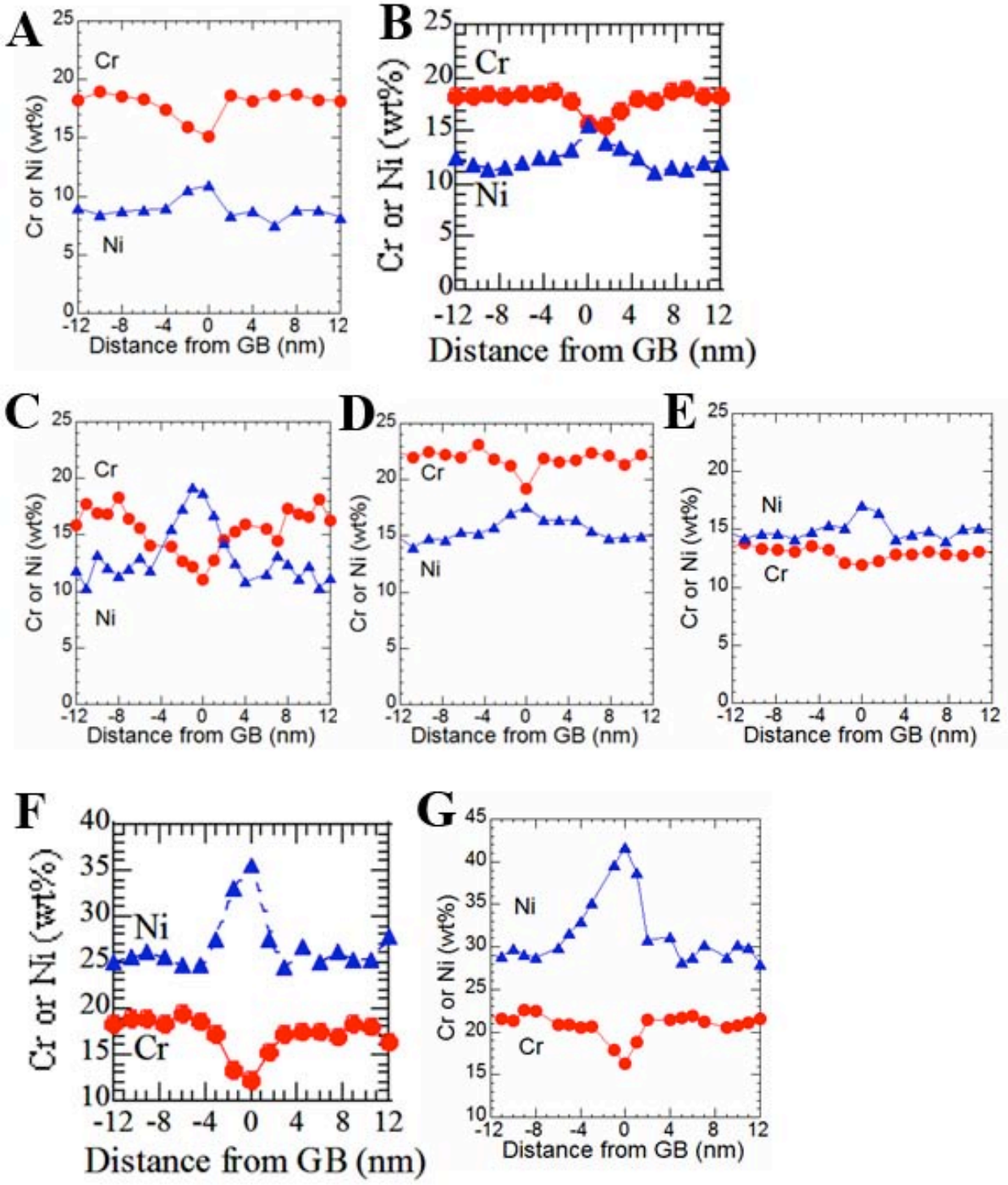

Figure 3-10: Cr and Ni grain boundary segregation profiles for all alloys, proton-irradiated to 5 dpa at 360°C.

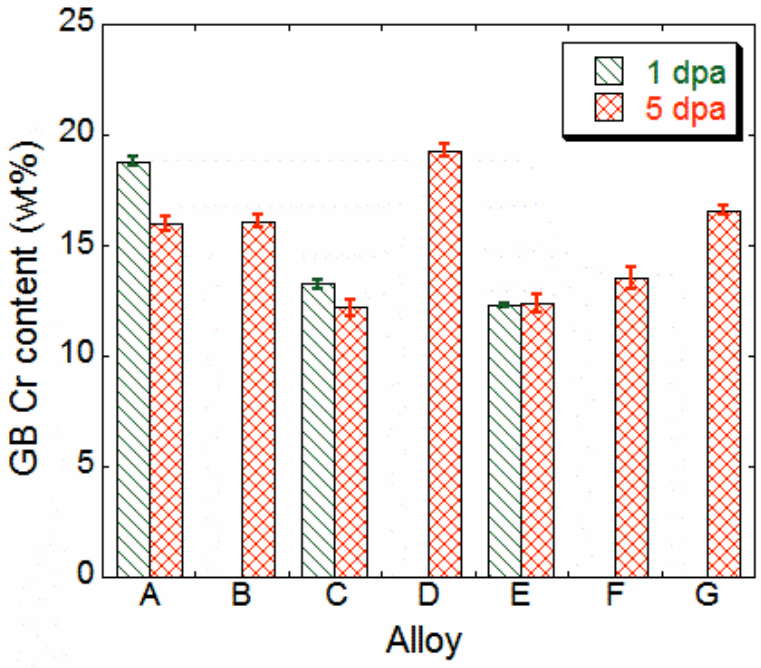

Figure 3-11: Measured grain boundary Cr composition for alloys A-G proton-irradiated to 1 and/or 5 dpa at 360°C.

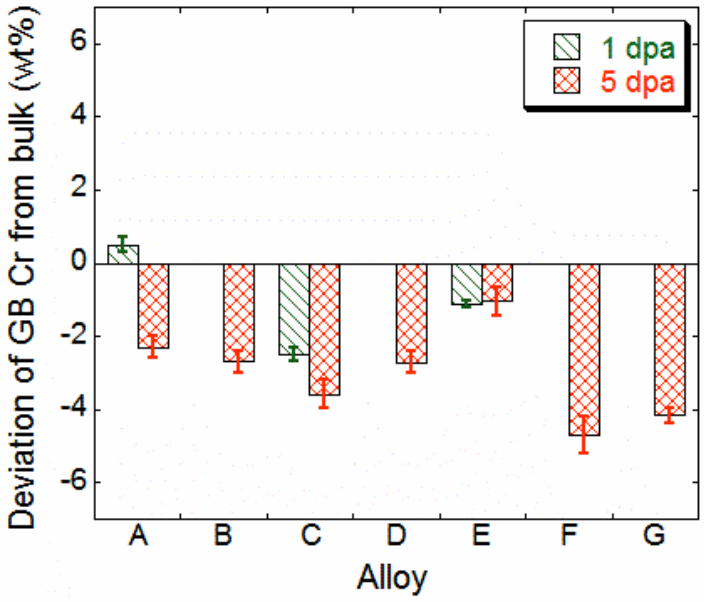

Figure 3-12: Measured grain boundary Cr deviation from bulk composition for alloys A-G proton-irradiated to 1 and/or 5 dpa at 360°C.

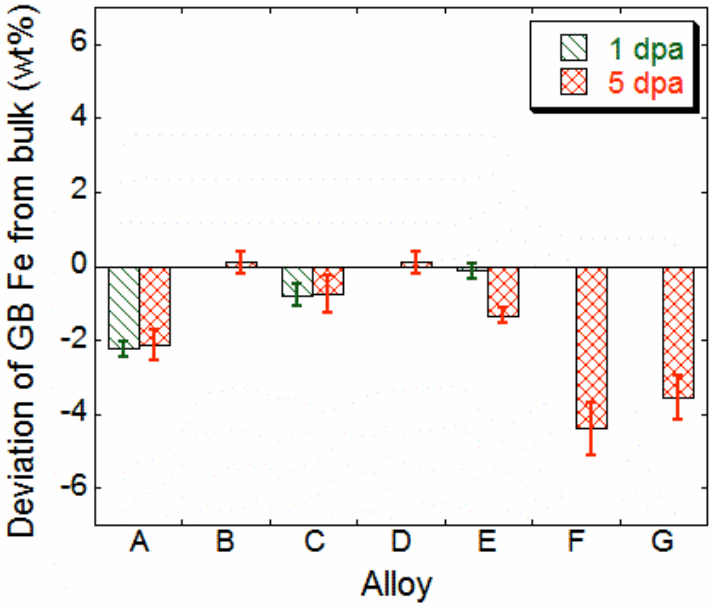

Figure 3-13: Measured grain boundary Fe deviation from bulk composition for alloys A-G proton-irradiated to 1 and/or 5 dpa at 360°C.

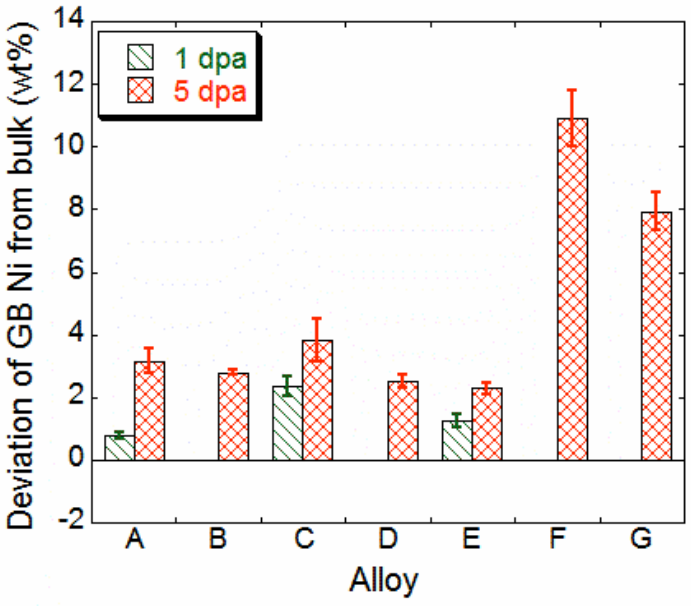

Figure 3-14: Measured grain boundary Ni deviation from bulk composition for alloys A-G proton-irradiated to 1 and/or 5 dpa at 360°C.

3.5 Interrupted CERT Testing

Thirteen interrupted CERT tests in simulated BWR NWC environment and eight interrupted CERT tests in argon were completed. For both environments, all the samples were strained at a rate of 3.5×10^{-7} s^{-1}.

3.5.1 BWR Environment (NWC)

Under NWC conditions, the water chemistry was allowed to stabilize at the test conditions (water temperature = 288°C, outlet water conductivity = 0.2 μS/cm and O_2 content = 2 ppm) for a period of three days, prior to straining. The water temperature and solution conductivity were well controlled during the tests. Alloys were first strained to 1% plastic strain at a strain rate of 3.5×10^{-7} s^{-1}. The test was then interrupted and the samples were removed from the autoclave for scanning electron microscopy (SEM) examination of cracking on the gage section. The samples were further strained to 3% and interrupted for cracking examination. If IASCC initiation was observed at 3%, no further straining was performed on the sample. Samples without cracks were then strained to the next strain level of 5% and the sample surfaces were once again examined for cracks. Samples showing no sign of cracks were further strained to the ultimate tensile stress (UTS) and the test was terminated. The interrupted CERT tests for all the alloys at 1 and 5 dpa are summarized in Table 3-6.

Fractography and semi-quantitative analysis of cracking susceptibility was performed on all of the specimens. The total crack length per unit area and the crack number density observed on the irradiated face are summarized for each specimen in Table 3-7. Micrographs of the irradiated face of each specimen after each strain interval in the NWC CERTS are shown in Figures 3-15 and 3-16, respectively, for 1 and 5 dpa.

All alloys that cracked exhibited intergranular cracking. For all the alloys irradiated to 1 dpa, cracks were only observed in alloy A. at 5 dpa, cracks were observed in alloy A, C and D at 1%. Cracks were observed in alloy E at 3% and significant crack growth was observed in alloys A, C and D. Alloys showed the greatest degree of cracking susceptibility while alloys B, F and G showed high cracking resistance even at 5 dpa and strained to UTS.

Crack initiation sites were carefully examined in alloys A, C and E at the condition of 5 dpa and 1% strain. Cracks were observed to initiate preferably at locations where a slip line intersected a grain boundary. Cracks tended to link to the MnS precipitates in alloy A as shown in Figure 3-17. A total of 6 crack initiation sites were found in alloy C and all of them can be linked to the interaction of slip lines with grain boundaries. One example of crack initiation sites is shown in Figure 3-18. Very likely, the initiation of cracks was the result of grain boundary deformation which was caused by the impingement of slip lines as indicated by small arrows in the inserts. More crack initiation sites in alloy C are shown in Figures 3-19(a) and 3-19(b). Similar crack initiation sites were also observed in

alloy E (Figure 3-19(c)). At the very beginning of the crack initiation stage, localized deformation as the result of the interaction of slip lines with grain boundaries plays a crucial role. The quantitative information of localized deformation is usually difficult to be obtained from samples tested under BWR conditions due to surface corrosions. Therefore, it is necessary to conduct parallel experiments in argon in favor of clean sample surfaces.

Table 3-6: Summary of interrupted tests carried out for the seven alloys.

Alloy #	Nominal	1 dpa				5 dpa			
		1%	3%	5%	UTS	1%	3%	5%	UTS
A	18Cr8Ni	√	√			√	√		
B	18Cr12Ni	√	√	√	√	√	√	√	√
C	15Cr12Ni	√	√	√	√	√	√	√	√
D	22Cr15Ni	√	√			√	√		
E	13Cr15Ni	√	√	√	√	√	√	√	√
F	18Cr25Ni	√	√	√	√	√	√	√	√
G	21Cr32Ni	√	√	√	√	√	√	√	√

Table 3-7: Summary of yield stress and IASCC susceptibility of the seven alloys.

Dose (dpa)	Alloy	IGSCC analysis			
		Strain (%)	Yield stress (MPa)	Crack density (mm^2)	Crack length per unit area ($\mu m/mm^2$)
1	18Cr8Ni	1	185	0	0
		3	-	20	3.6
	18Cr12Ni	1		0	0
		3	174	0	0
		5	-	0	0
		UTS		0	0
	15Cr12Ni	1	167	0	0
		3	-	0	0
		5		0	0
		UTS		0	0
	22Cr15Ni	1	164	0	0
		3	-	0	0
		5		0	0
	13Cr15Ni	1	170	0	0
		3	-	0	0
		5		0	0
		UTS		0	0

	18Cr25Ni	1	167	0	0
		3	-	0	0
		5		0	0
		UTS		0	0
	21Cr32Ni	1	160	0	0
		3	-	0	0
		5		0	0
		UTS		0	0
5	18Cr8Ni	1	190	35	30
		3	-	150	188
	18Cr12Ni	1	162	0	0
		3	-	0	0
		5		0	0
		UTS		0	0
	15Cr12Ni	1	169	20	3.5
		3	-	50	50.5
	22Cr15Ni	1	158	15	3.7
		3	-	15	4.3
	13Cr15Ni	1	176	0	0
		3	-	20	21.9
	18Cr25Ni	1	159	0	0
		3	-	0	0
		5		0	0
		UTS		0	0
	21Cr32Ni	1	165	0	0
		3	-	0	0
		5		0	0
		UTS		0	0

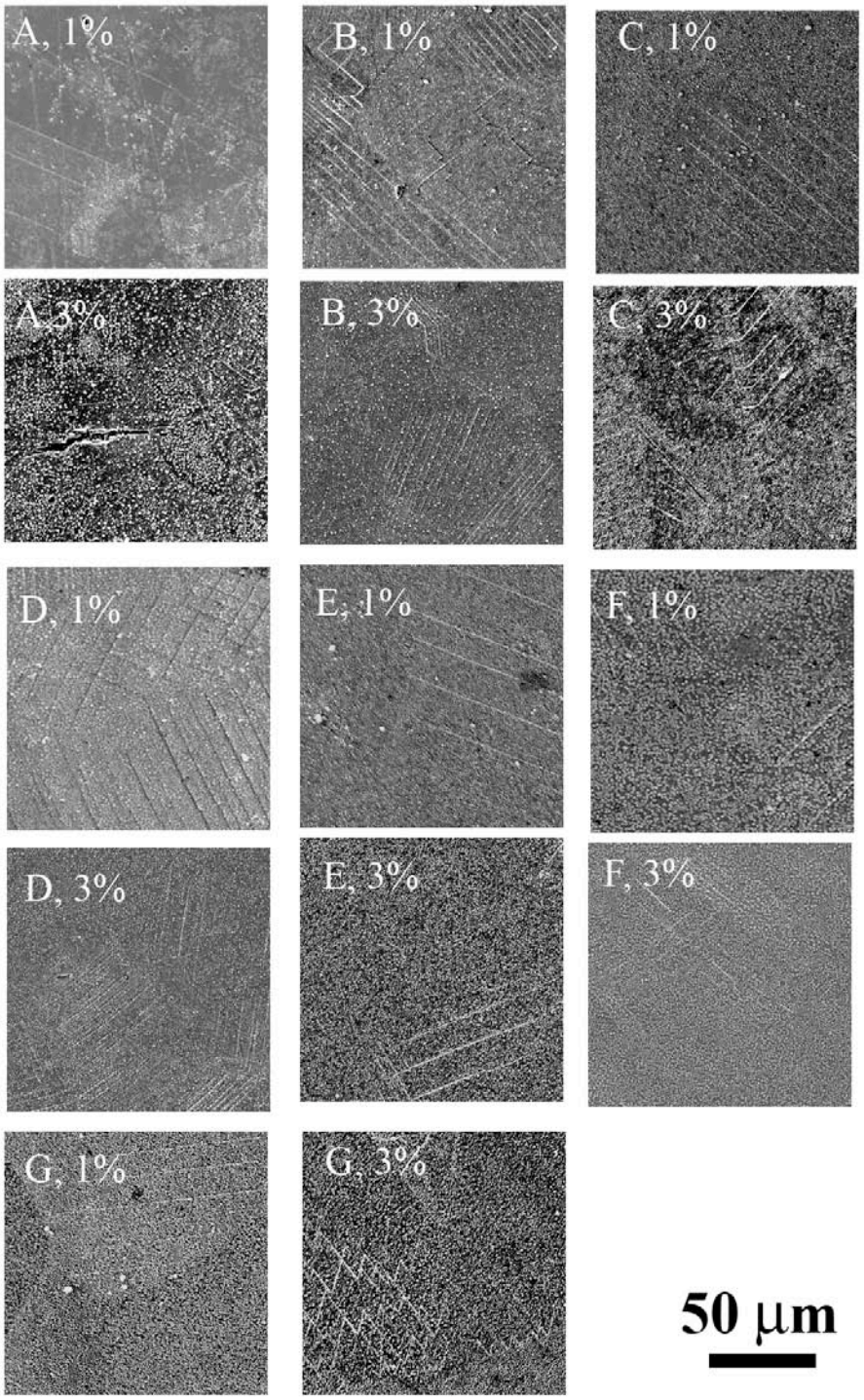

Figure 3-15: SEM images of the irradiated surfaces after 1 and 3% strain for alloys A-G proton-irradiated to 1 dpa at 360°C.

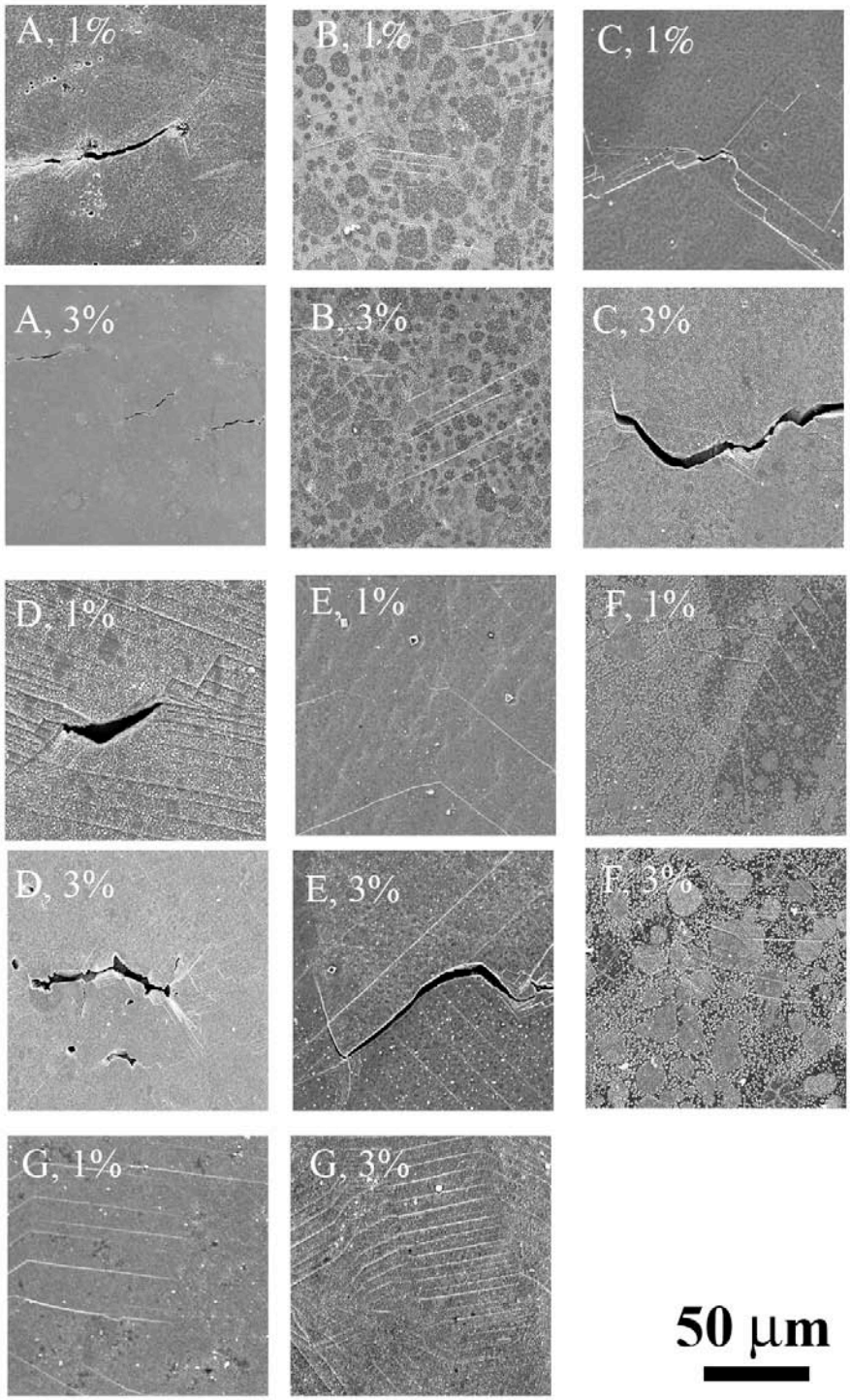

Figure 3-16: SEM images of the irradiated surfaces after 1 and 3% strain for alloys A-G proton-irradiated to 5 dpa at 360°C.

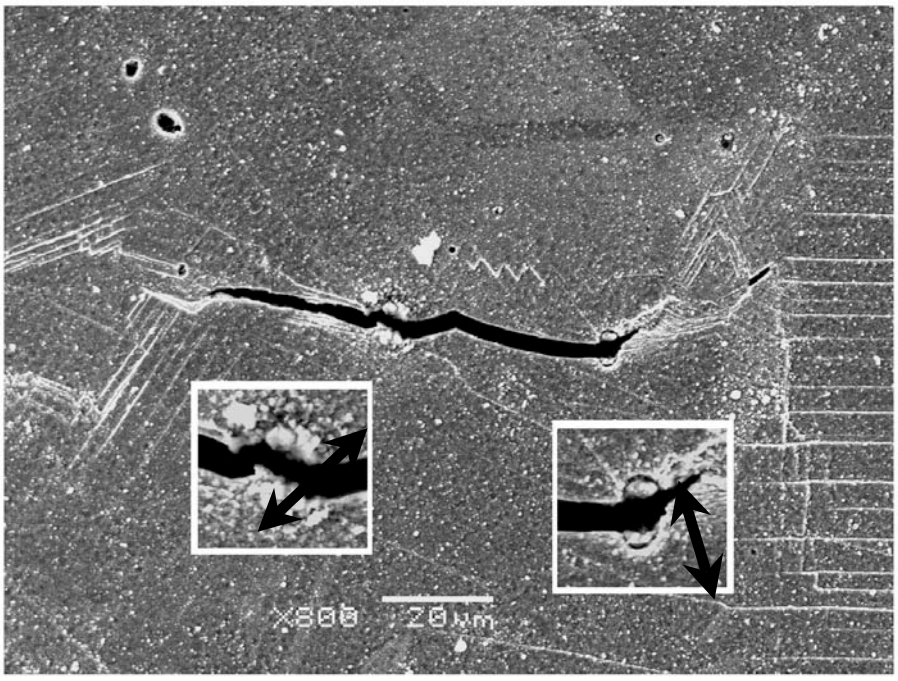

Figure 3-17: Fracture of MnS inclusions in alloy A irradiated to 5 dpa and strain to 1% in BWR. The fractured MnS inclusions are magnified in the inserts.

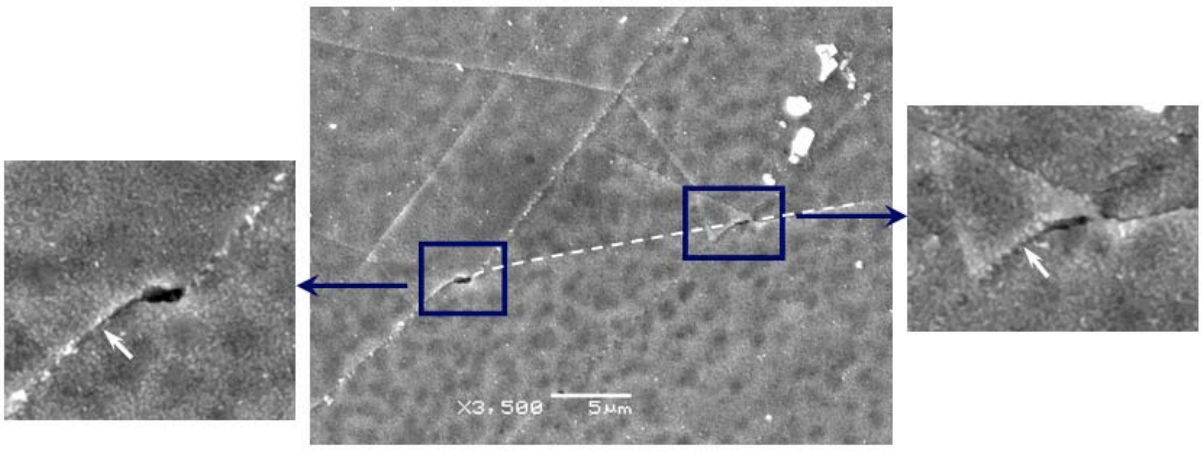

Figure 3-18: Crack initiation in proton-irradiated alloy C strained to 1% in simulated BWR environment. The position of the grain boundary is highlighted by dashed line. The slip lines are indicated by small arrows in the inserts.

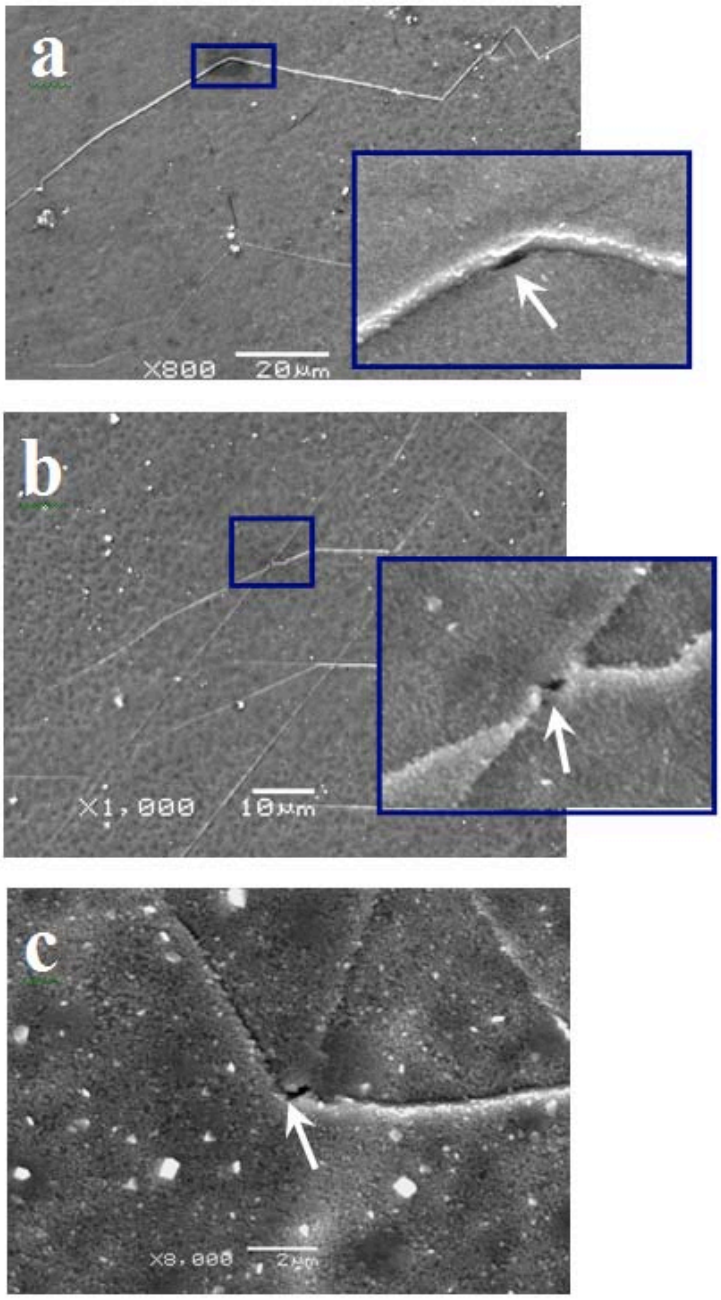

Figure 3-19: More examples of crack initiation sites in alloys C ((a) and (b)) and E (c) irradiated to 5 dpa at 360°C and strained to 1% in simulated BWR environment.

3.5.2 CERT tests in argon

The characterization of the localized deformation requires a clean sample surface. To obtain a relatively clean surface, interrupted CERT tests were also performed in argon in a multiple-specimen test system at 288°C using the same strain rate of 3.5×10^{-7} s^{-1}. All alloys irradiated to 1 and 5 dpa were strain to 1% and 3% except alloy D at 1 dpa, which the irradiated tensile sample for test in argon was not available. After each strain, the irradiated surfaces were examined for slip channel morphologies and any sign of crack. The slip channel height was measured from replicas of the irradiated and deformed surface using AFM.

Figure 3-20 shows the typical morphologies of slip channels observed on the surface of proton-irradiated austenitic alloys strained in argon at 288°C in alloy C and G. A notable feature of slip channels in both alloys strained to 1% is their inhomogeneity. First, the spacing between slip lines varies from one grain to another and even within the same grain. For instance, the spacing between slip lines in Figure 3-20 (b) can be as large as 30 μm and as low as 1 μm. Secondly, the amount of deformation in slip channels fluctuates. Some slip channels as indicated by arrows in Figures 3-20 (a) and (b) obviously have much greater deformation than others. Within the same grain, the height of slip channels in alloy G at 1 dpa and 1% strain ranges from 34 nm to 245 nm. As the samples are strained further to 3%, both channel height and spacing tend to be more homogenous (Figure 3-20 (c)). The largest spacing between channels in Figure 3-20 (c) is about 15 μm. More SEM images of the morphologies of slip channels are shown in Figure 3-21.

The inhomogeneity at 1% is better seen from AFM surface plot. Figure 3-22 shows AFM surface plots of alloy C irradiated to 1 dpa and strained to 1 and 3% at 288ºC. The slip channel marked 1 that did not exist after 1% strain appeared after 3% strain. The slip channel marked 2 was the largest after 1% strain in the grain, but after 3%, the channel height became more uniform within the same grain.

The average channel height and the weighted average channel height for alloys are summarized in Table 3-8. A comparison of the weighted average channel height among alloys is shown in Figure 3-23. In general, weighted average channel height increases with strain and dose. The channel height is greatest in alloy A irradiated to 5 dpa and strained to 3% (420 nm) and smallest in alloy G irradiated to 1 dpa and strained to 1% (119 nm).

The distribution of slip channels in alloys irradiated to 1 and 5 dpa and strained to 1% and 3% are shown in Figure 3-24 and 3-25, respectively. Compared to that of 1 dpa, distributions of 5 dpa samples are wider spread.

Table 3-8: summary of average channel height and weighted average channel height and yield stress at 0.2% strain for all seven alloy irradiated to 1 and 5 dpa and strained to 1% and 3% at 288ºC in argon. Average channel spacing was examined for some conditions.

Dose (dpa)	Alloy	Localized deformation analysis					
		Strain (%)	Yield stress (MPa)	Number of grains/channels	Avg channel height (nm)	weighted channel height (nm)	Average channel spacing (μm)
1	A	1	192	6/20	164.4	197	8
		3	-	7/43	238	311	
	B	1	162	13/79	83.8	122	
		3	-	11/70	179.4	239	4
	C	1	165	10/58	203.8	255	
		3	-	11/85	288.9	351	
	D	1	-	NM			
		3	-	NM			
	E	1	173	7/39	154.9	190	7
		3	-	8/40	208.5	288	
	F	1	159	12/40	128.5	168	4.5
		3	-	11/80	179.3	232	
	G	1	158	10/37	84.6	119	
		3	-	12/69	139.6	180	
5	A	1	201	7/36	319.2	401	10
		3	-	8/42	304.5	420	
	B	1	168	11/75	90.4	139	
		3	-	11/75	245.4	313	
	C	1	177	10/29	260.6	322	
		3	-	13/57	313.3	364	
	D	1	162	15/56	243.7	313	
		3	-	12/79	293.8	360	
	E	1	183	14/101	206	322	7.8
		3	-	10/69	316.4	393	
	F	1	165	15/75	195.5	305	
		3	-	11/61	266.7	348	
	G	1	156	8/28	112.9	146	
		3	-	6/37	242.4	314	

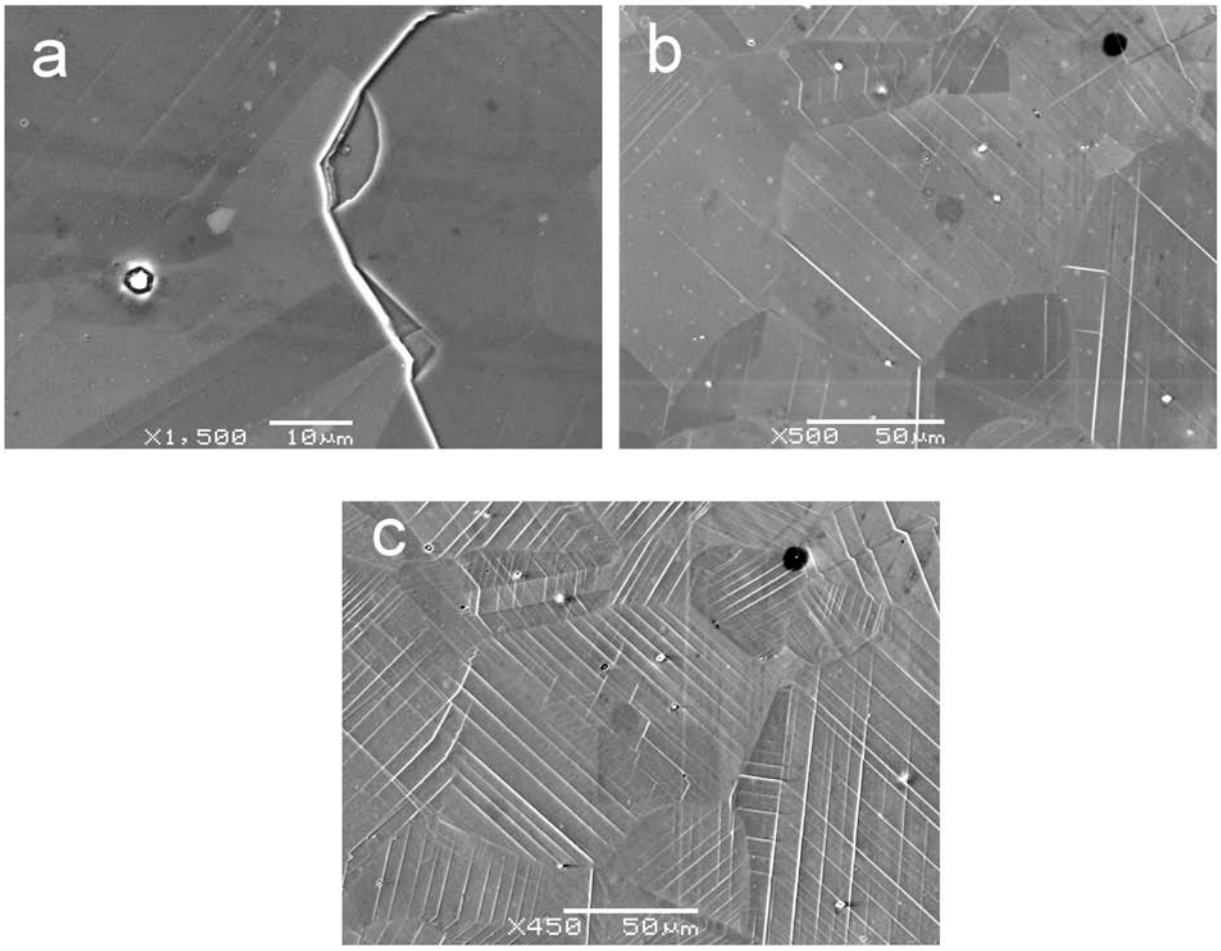

Figure 3-20: Morphologies of slip channels on the surface of irradiated samples strained in argon at 288°C: (a) C at 5 dpa and 1%, (b) G at 1 dpa and 1% and (c) G at 1 dpa and 3%.

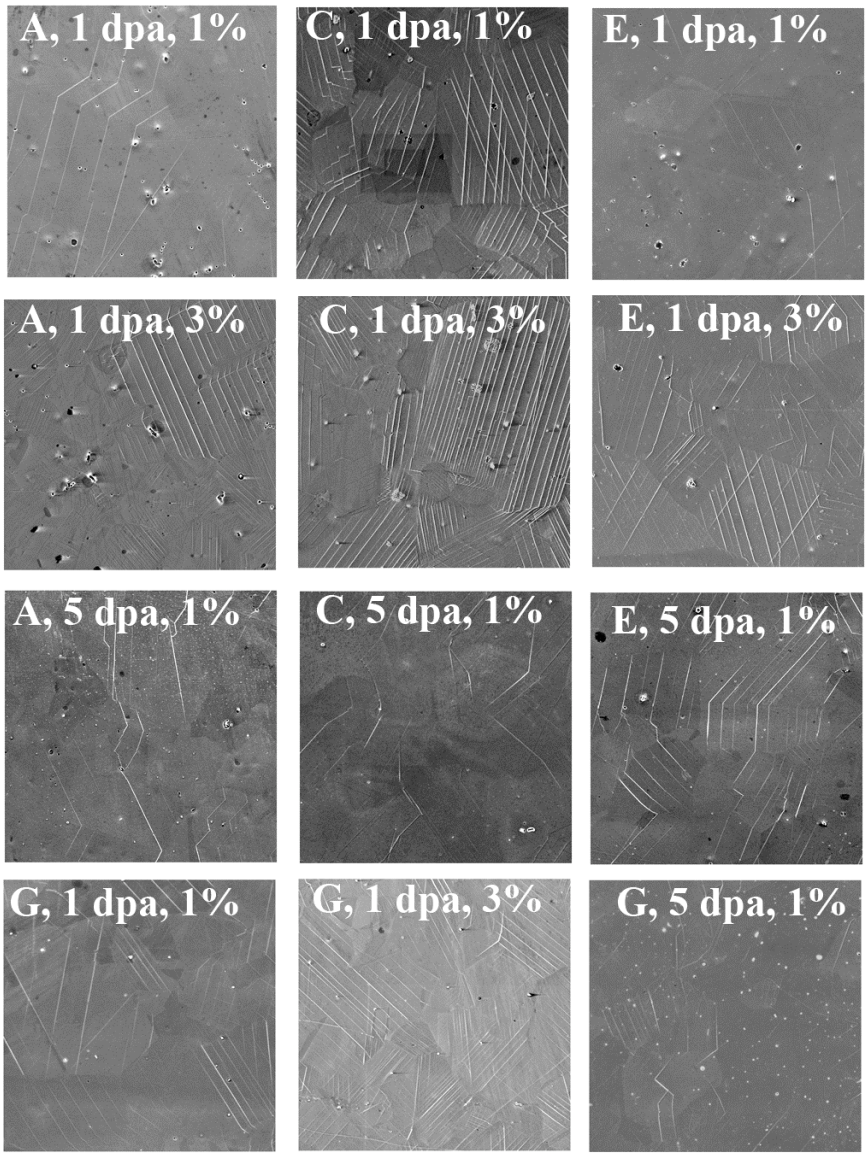

Figure 3-21: SEM images of slip channel morphologies in several alloys irradiated to 1 and 5 dpa and strained to 1% and 3% at 288ºC in argon.

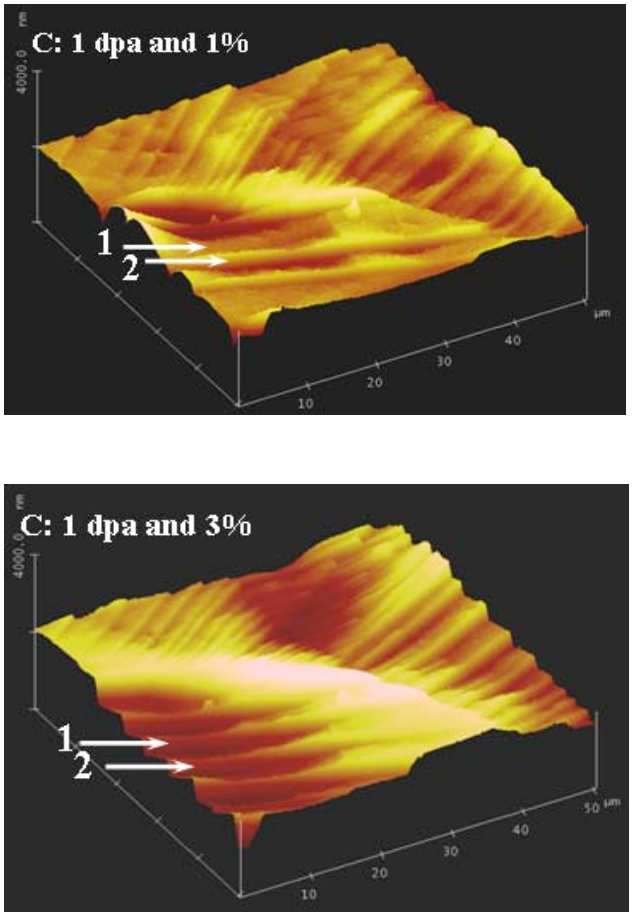

Figure 3-22: AFM surface plot of alloy C irradiated to 1 dpa and strained to 1 and 3% at 288ºC. The slip channel marked 1 that did not exist after 1% strain appeared after 3% strain. The slip channel marked 2 was the largest after 1% strain in the grain, but after 3%, the channel height became more uniform within the same grain.

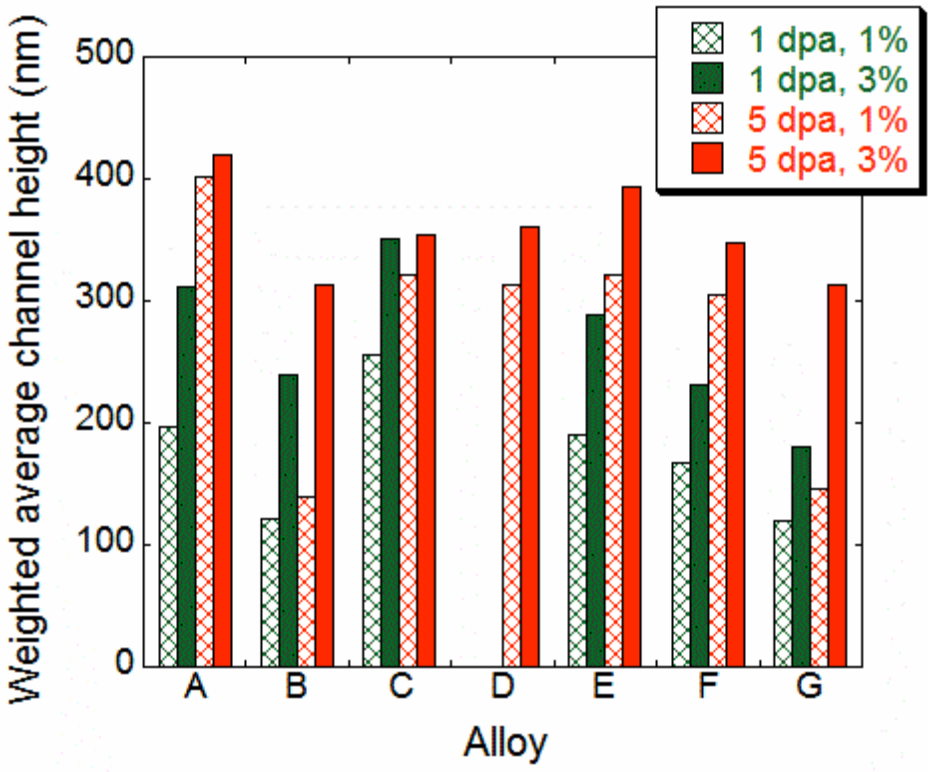

Figure 3-23: A comparison of weighted average channel height among alloys irradiated to 1 and 5 dpa and strained to 1% and 3% at 288ºC in argon.

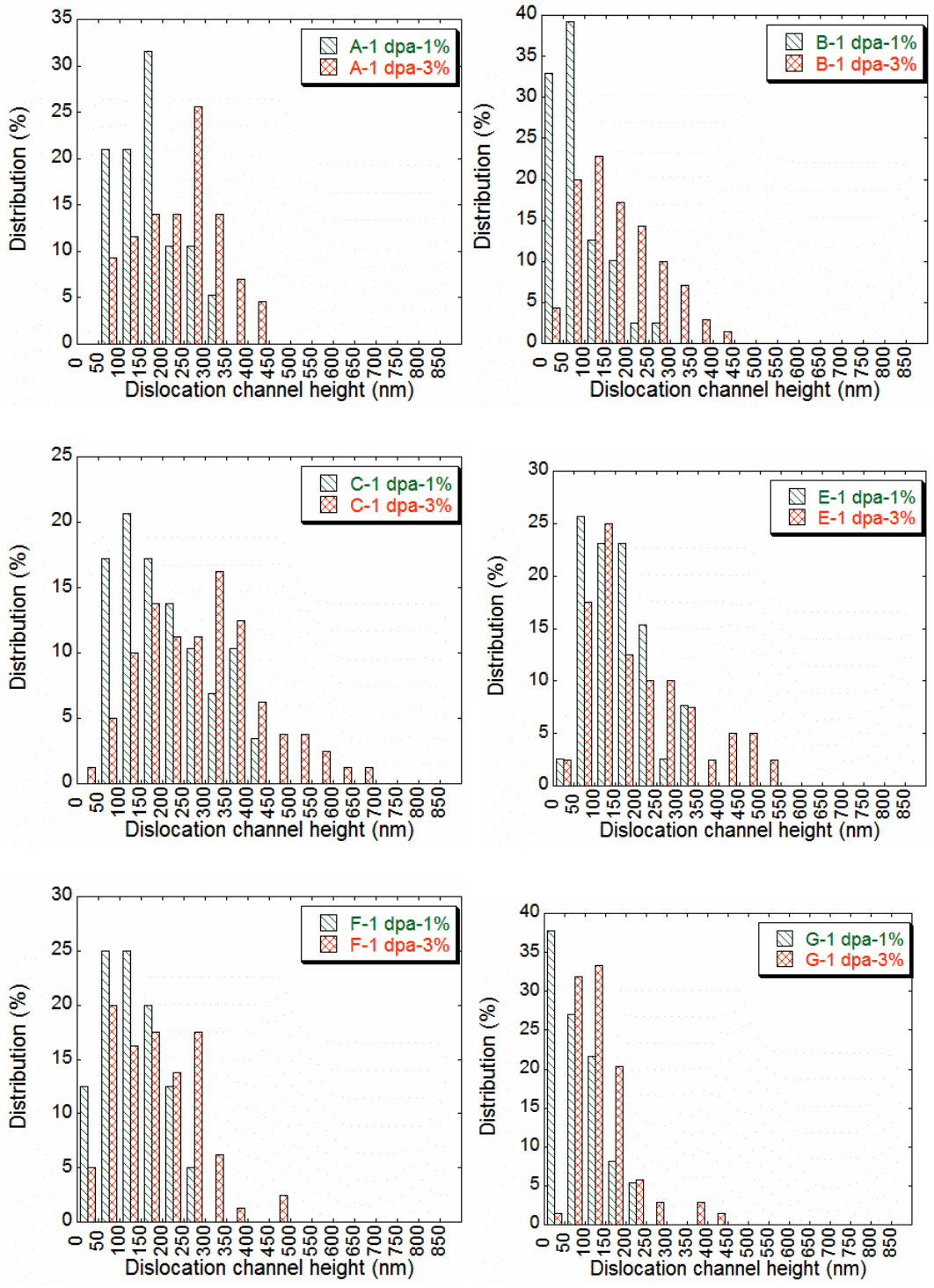

Figure 3-24: Distribution of slip channels in alloys A, B, C, E, F and G irradiated to 1 dpa and strained to 1% and 3% in argon.

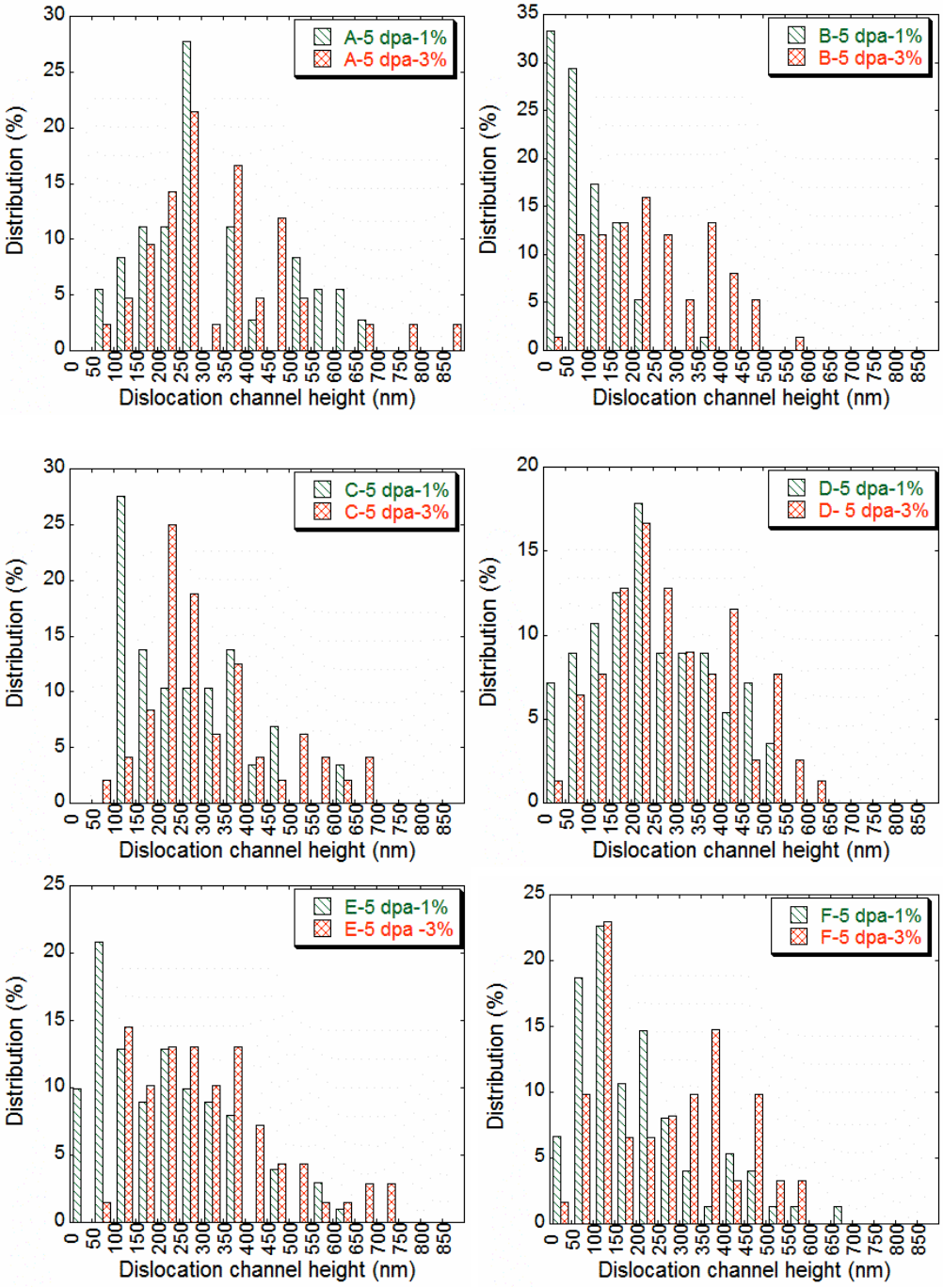
A-5 dpa-1%
A-5 dpa-3%
B-5 dpa-1%
B-5 dpa-3%
C-5 dpa-1%
C-5 dpa-3%
D-5 dpa-1%
D- 5 dpa-3%
E-5 dpa-1%
E-5 dpa -3%
F-5 dpa-1%
F-5 dpa-3%
Distribution (%)
Dislocation channel height (nm)

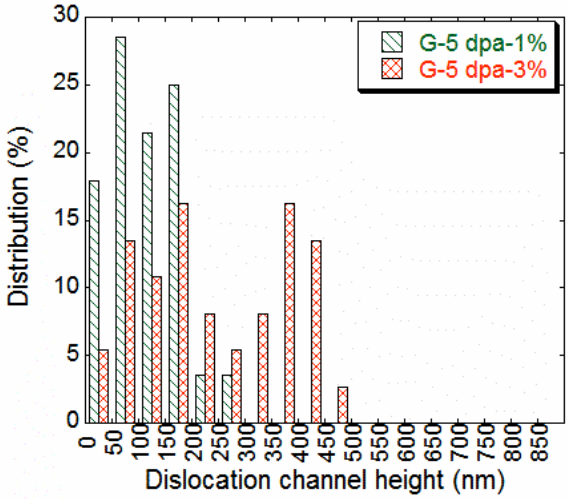

Figure 3-25: Distribution of slip channels in alloys A, B, C, E, F and G irradiated to 1 dpa and strained to 1% and 3% in argon.

4. Discussion

In this chapter, the results presented in Chapter 3 are analyzed. Stacking fault energy and radiation-induced hardening and calculated changes to yield stress are discussed first. Characterization of the dislocation loops and voids are also analyzed and compared to the observed changes in hardness. The influence of the different solutes on microstructure is also compared to the available literature data. Radiation-induced segregation is then discussed followed by localized deformation. The influence of the SFE, hardness and localized deformation on cracking susceptibility in water environment is discussed. Finally, the potential mechanisms of IASCC are reevaluated using the results from this study.

4.1 Stacking fault energy

Depending on the empirical equation, the predicted SFE value can vary significantly. While the absolute values are questionable, they can be used as a guide to see if the measured value agrees with the general trend of predicted values. Figure 4-1 shows the measured SFEs compared to those predicted by Pickering's correlation [16]. The measured values are always smaller than the predicted ones. However, they generally follow the same trend. The SFE differences among alloys are typically as expected. The measured SFE values are also compared to the values from theoretical calculation [24] and other experimental data by other researchers for similar alloys (Figure 4-2). The measured values are within the range of other experimental and theoretical calculation data.

Since we have measured seven alloys with various Cr, Ni and Si compositions, a regression run over the three elements is possible. The regression result is shown as follows:

$$SFE=1.8+0.5*Cr+1.7*Ni-42*Si \quad (4\text{-}1)$$

Predicted values by this study as compared to the measured values and the values predicted by Rhodes' correlation [25] in Figure 4-3. The regression result matches the measured value much better.

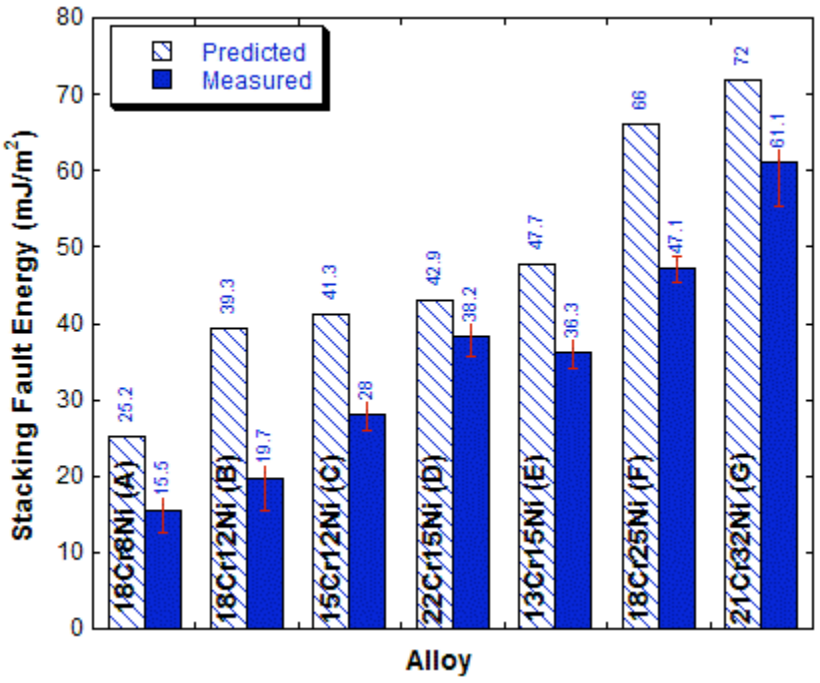

Figure 4-1. Measured stacking fault energies as compared to the predicted values by Pickering's correlation [16].

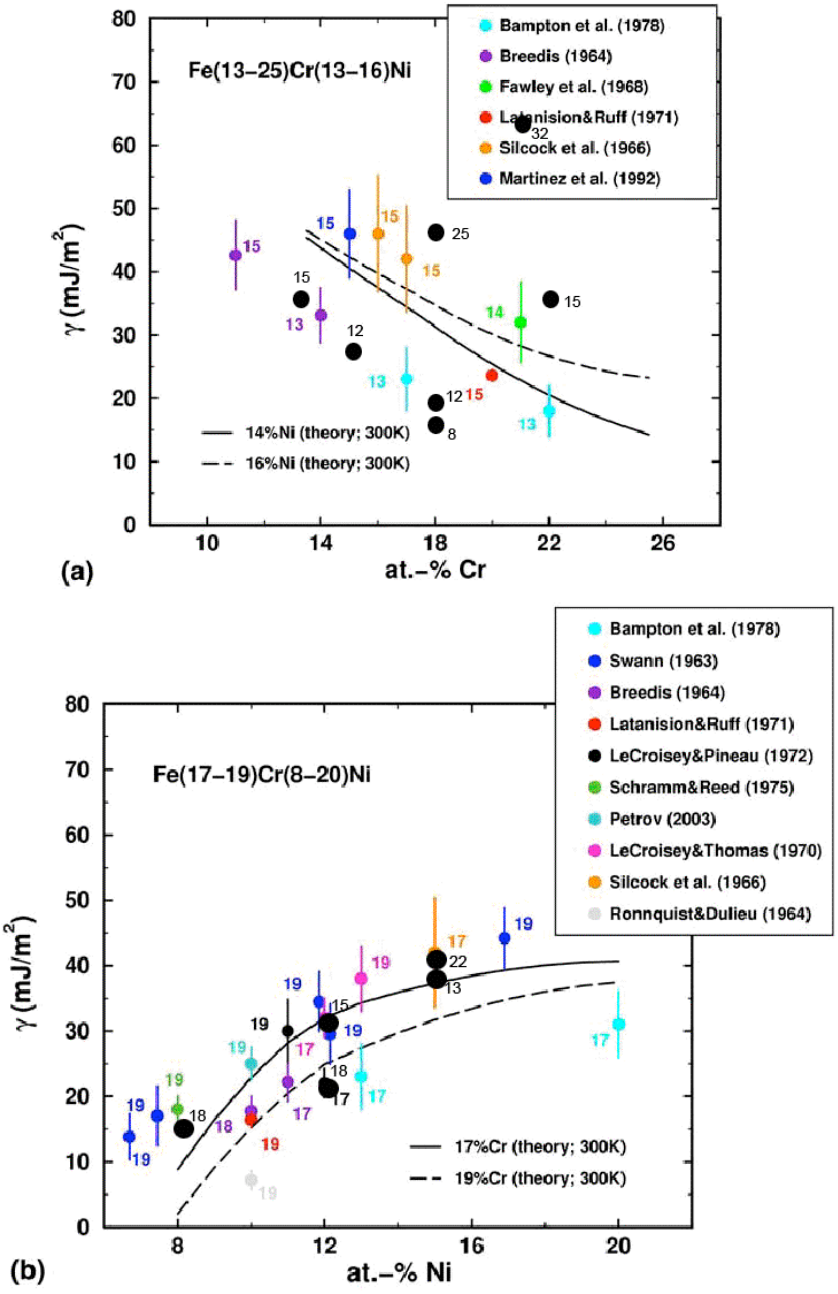

Figure 4-2. Effect of alloying on the theoretical (solid and dashed lines) and experimental SFE energy in Fe–Cr–Ni alloys. [24] The numbers next to the symbols give the actual compositions used in experiments. The larger solid circles were measured in this study.

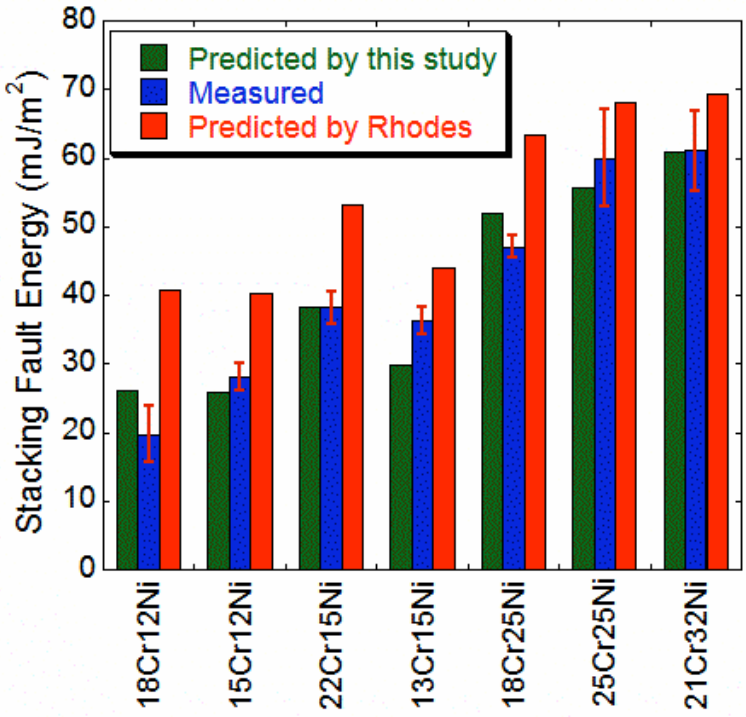

Figure 4-3: Predicted values by this study as compared to the measured values and the values predicted by Rhodes' correlation [24].

4.2 Microstructure

4.2.1 Dislocation Loops

The mean loop diameter and density are plotted as a function of dose along with data from the CIR-I program [19, 24] in Figure 4-4. The boxes in the figures show the range of the data measured in this study. The measured loop diameters are in good agreement with those from previous studies. The measured loop densities are in excellent agreement with similar proton irradiated alloys but they are generally lower than the neutron-irradiated alloys. The loop density for neutron irradiation is higher than that for proton irradiation by a factor of between 1.5 and 3 in 304 and 316 stainless steels [27].

Among the seven alloys, alloy A had the smallest loop diameter, but the loop density was a factor of two – three higher. The higher Si content in alloy A (0.65%) may be responsible for the higher loop density than other alloys, which contains only $\leq$0.1 wt% Si. This is also consistent with the work of Carter et al. [28] who examined Si- and P-doped alloys irradiated with protons to 1.0 dpa at 400°C. Carter et al. measured a dislocation density in a Si-doped heat that was almost a factor of two higher than found in the base heat. Silicon is known to enhance the vacancy diffusivity [29]. An increase in vacancy diffusivity may lead to an increase in vacancy loss at sinks, thus the partitioning

of interstitials to loops will increase, consistent with the experimental results of this study and those of Carter.

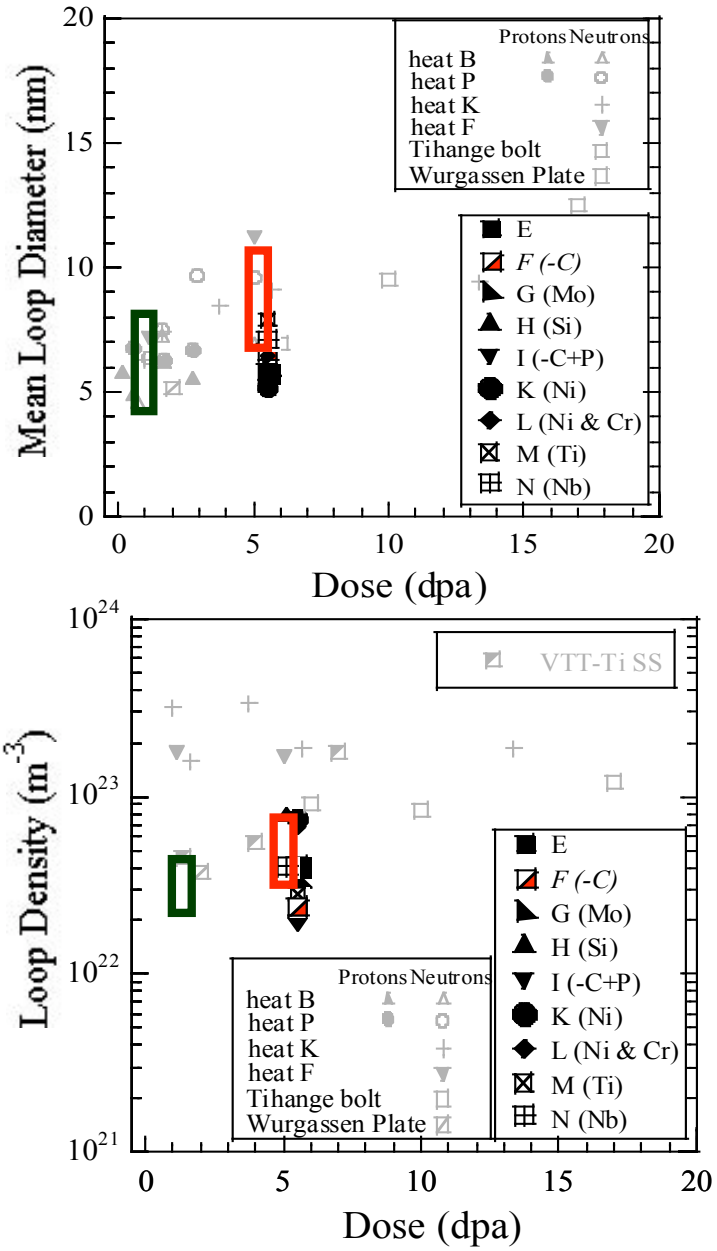

Figure 4-4: Comparison of solute addition alloys irradiated with protons to 5.5 dpa at 360°C with proton- and neutron-irradiated alloys from CIR-I [19, 24, 30]. The boxes in the figures show the range of the data measured in this study.

4.2.2 Voids

Voids were observed in three of the seven alloys, B, D, and E, at 1 dpa. At 5 dpa, voids were observed in all high purity alloys B-G but not in the commercial grade alloy, A. Voids have been observed in previous studies of proton-irradiated high-purity austenitic stainless steels [31], but not in commercial purity alloys [24].

One reason for the absence of voids in alloy A may be the presence of silicon. Bates et al. [3231] found Si to be a very effective swelling inhibitor in neutron irradiated 316 stainless steels (2 x 10^{22} n/cm^2, E > 0.1 MeV at ~ 500°C). Brager [33] also reported a significant reduction in swelling in increased Si content in neutron-irradiated 316 stainless steels. A decrease of swelling with increasing Si from 2.75% at 0.16 wt.% to 0.1% at 0.9 wt.% was observed. Silicon is believed to suppress void swelling by increasing the vacancy diffusivity and reducing the vacancy supersaturation, thereby reducing void nucleation [29].

Swelling in alloys B, D, F and G was calculated and plotted in Figure 4-5. It shows an increase with Cr content and a decrease with Ni content. These trends are consistent with the literature [34, 35] as shown in Figures 4-6 and 4-7.

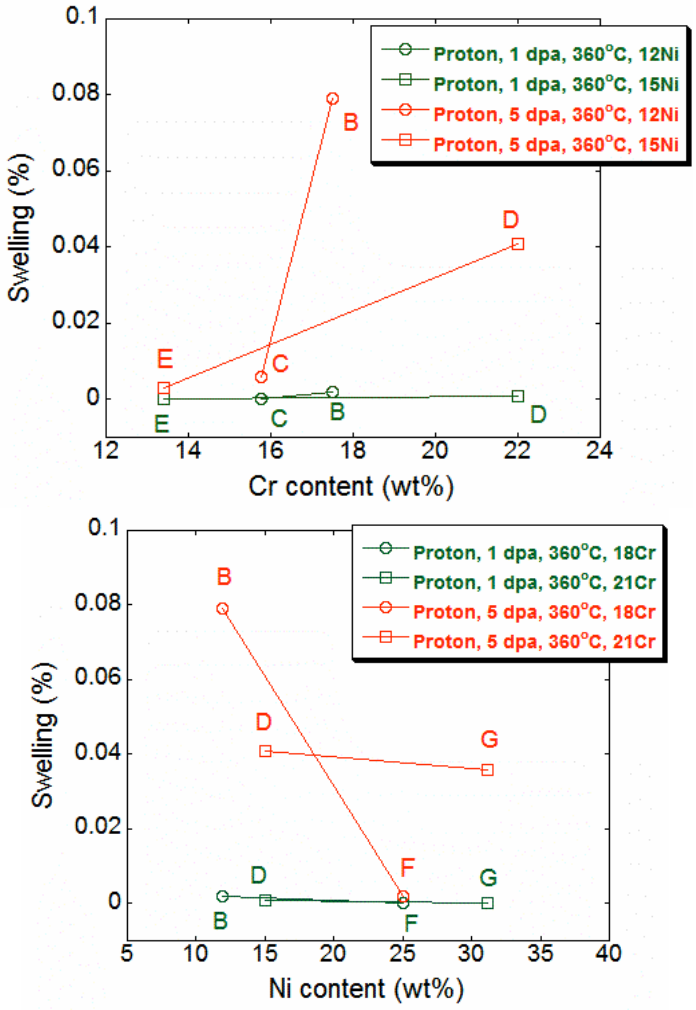

Figure 4-5: Swelling as a function of Ni and Cr content.

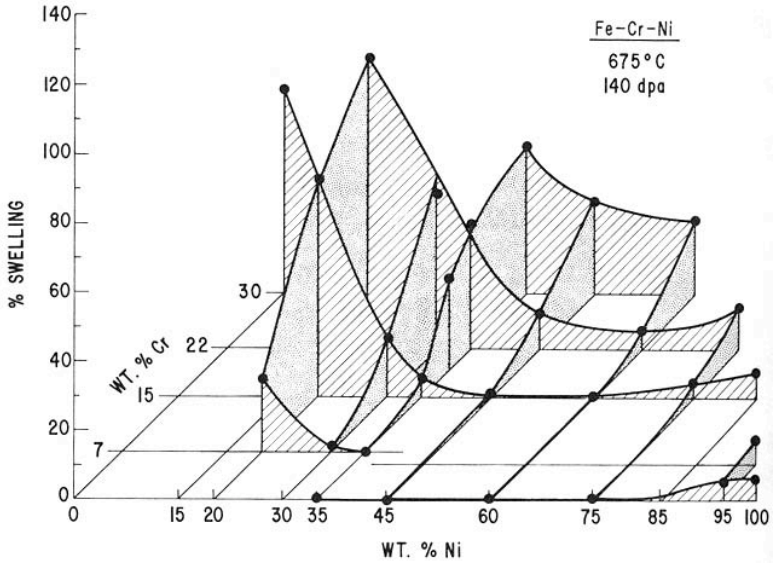

Figure 4-6: Swelling as a function of Ni and Cr content in Fe-Cr-Ni alloys. [34]

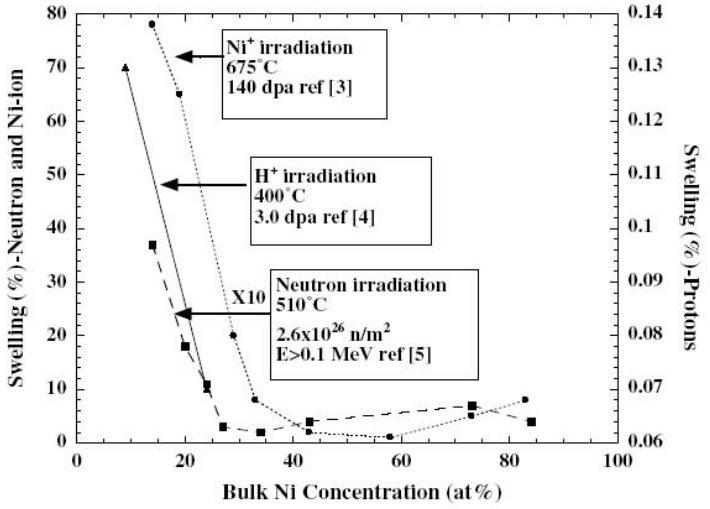

Figure 4-7: Swelling as a function of Ni content in Ni+, neutron or proton irradiated austenitic alloys. [35]

4.3 Irradiated Microstructure and Hardening

The change in yield strength due to irradiation can be estimated using the dispersed-barrier hardening model [36]. In this model, the increase in yield stress, $\Delta\sigma_y$, is equal to the increase in applied stress required to move a dislocation through a field with obstacle strength, α, and inter-obstacle spacing, L. The changes in yield stress, $\Delta\sigma_y$, can be calculated using a simple equationL

$$\Delta\sigma_y = \frac{M\alpha\mu b}{L} = \begin{cases} M\alpha\mu b\sqrt{Nd}, & \text{for discrete obstacles} \\ M\alpha\mu b\sqrt{\rho_d}, & \text{for network dislocations} \end{cases} \tag{4-2}$$

where N is the number density of obstacles, d is the mean diameter of the obstacle, ρ_d is the network dislocation density, μ is the shear modulus of the matrix, b is the Burgers vector of the moving dislocation, and M is a factor to relate the shear stresses on a slip plane in a single crystal to the applied tensile stress necessary to activate slip in a polycrystalline material (M=3.06, [37]). The barrier strength, α, is typically taken as 0.25 for loops and 1.0 for voids [38]. Frank loops and small precipitates have intermediate strength and dislocations are the weakest barriers. The contributions from different defect types are typically combined with a superposition law and the total change in the yield stress, $\Delta\sigma_{tot}$, can be calculated as;

$$\Delta\sigma_{tot} = \sqrt{\sum_i \left(\Delta\sigma_{SR,i}\right)^2} + \Delta\sigma_{LR}, \tag{4-3}$$

where $\Delta\sigma_{SR}$ is for short range obstacles such as Frank loops and voids in Equation 4-3, and $\Delta\sigma_{LR}=3\alpha\mu b\rho^{0.5}$ is for the long range obstacle such as network dislocations (ρ is dislocation density).

The change in yield stress from dislocation and void microstructure is compared to that calculated from hardness measurements in Figure 4-8. The 45° line in Figure 4-13 represents a one-to-one correlation between yield stress from hardness and that calculated from microstructure. In general, the two values are in good agreement. The values calculated from hardness at 1 dpa are lower than those calculated from microstructure, and they are probably underestimated if a single coefficient was used for both doses. If a larger coefficient was used for 1 dpa as suggested in [39], a better fit can be observed.

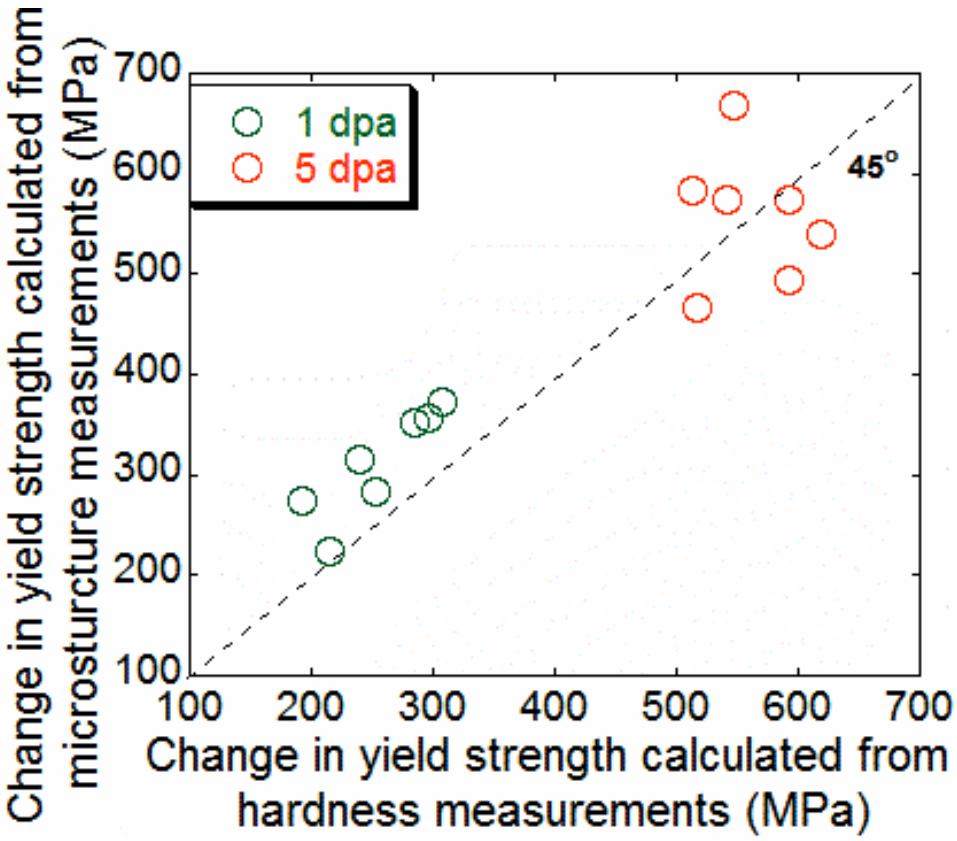

Figure 4-8: Comparison of change in yield strength calculated from hardness and change in yield strength calculated from dislocation and void microstructure for alloys A-G irradiated with protons to 1 and 5 dpa at 360°C. $\alpha = 0.5$ for loops and $\alpha = 1.0$ and for voids.

4.4 Radiation induced segregation

Radiation-induced segregation was measured in all eight irradiated alloys. In all cases, Cr was depleted and Ni was enriched. This is consistent with the literature of austenitic alloys irradiated with either neutrons or protons. The amount of enrichment of Ni and depletion of Cr were found to be dependent on the bulk Ni content as shown in Figure 4-9. Bulk Ni content may be the driving force for observed RIS.

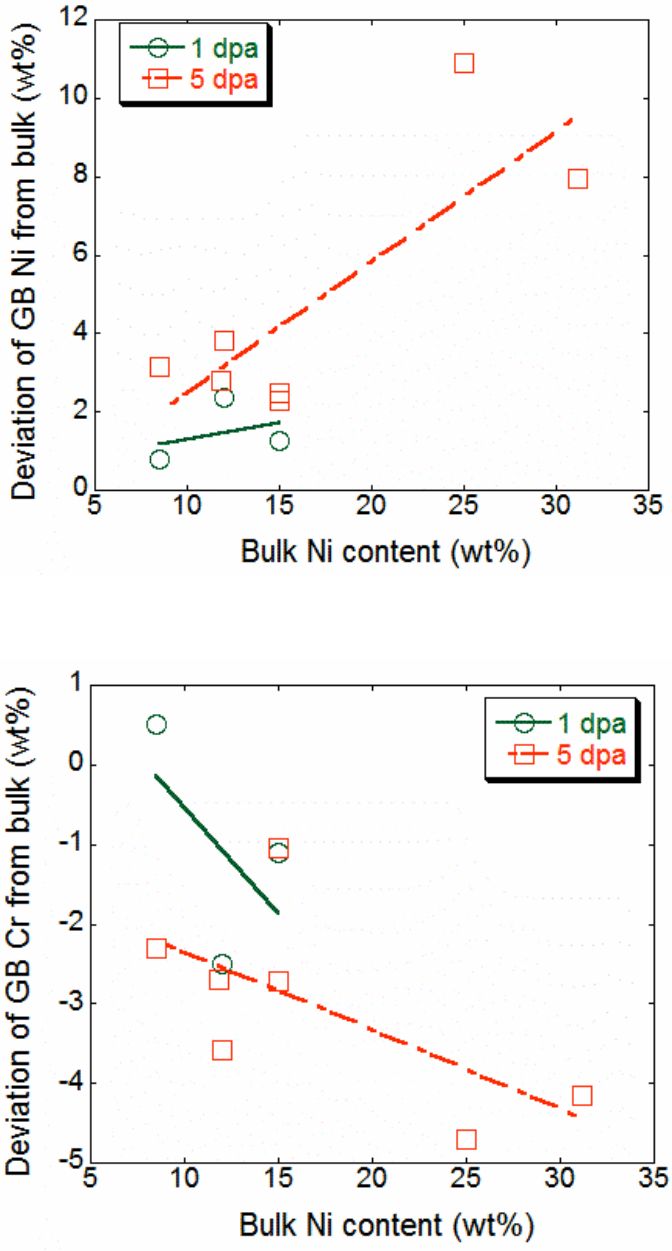

Figure 4-9: Deviation of grain boundary Ni and Cr content after irradiation as a function of bulk Ni content.

4.5 Localized deformation

Changes in deformation mode from a uniform mode to an inhomogeneous, localized mode can be detrimental to IASCC, as noted by Bruemmer et al. [40]. The nature of deformation can be influenced by radiation microstructures and differences in material properties such as stacking fault energy. Since the mechanical properties such as hardness are also affected by irradiation microstructures, correlation between localized deformation and hardness may exist.

4.5.1 Irradiation microstructure and localized deformation

The presence of radiation-induced microstructure can have a profound influence on deformation mode. The interaction between small loops and moving dislocations may result in very inhomogeneous deformation, through either twinning or dislocation channeling. Cole et al, [41] found that twinning or channeling are dependent on the test temperature and strain rate. At low strain rates and/or high temperatures, the material deforms by channeling, whereas at high strain rates and/or low temperatures, the material deforms by twinning.

In the channeling process, the initial, moving dislocations encounter a dislocation loop, which acts as a barrier to the dislocations. To overcome this barrier, dislocations annihilate or combine with the defects on the slip plane and continue to glide. Lee et al. [42] examined this process in some detail and concluded that the interaction between a moving glide dislocation and radiation-induced defect occurs by a two-step process with pairs of partial dislocations. Subsequent dislocations will tend to glide along this same path, clearing out additional defects resulting in a channel that is free of defects. The areas in between the channels usually remain untouched, so all of the deformation is concentrated in these channels, resulting in highly localized deformation.

To examine which irradiation feature contributes more to the localized deformation, the weighted average channel height was plotted against dislocation loop size and density, void size and density in Figures 4-10 and 4-11. There is no correlation between dislocation loop size and channel height, however, the channel height shows dependence on loop density. Average channel height tends to be larger in alloys with high population of dislocation loops. Larger voids and higher density do not result in larger degree of localized deformation; instead, channel height tends to decreases with increasing void size and density (Figure 4-12).

Figures 4-13 and 4-14 show the correlation between weighted average channel height and irradiation hardening calculated from irradiation microstructure *with* (Figure 4-13) and *without* (Figure 4-14) the contribution of voids. A better correlation was observed if the hardening from voids were removed. This means that dislocation loops are more important than voids to promote localized deformation.

Dislocation channels are clear of dislocation loops. Once channels are formed, dislocations are confined to the channels due to the harder matrix in between dislocation

channels. Therefore, localized deformation shows dependence on the irradiation hardening due to dislocation loops. Large voids cannot be removed by gliding dislocations. The voids do not change the relative hardness between dislocation channels and the matrix. Also larger void size and higher void density may promote dislocation cross-slip. Moving dislocations cannot annihilate voids as they would with dislocation loops, but must still overcome these obstacles. Voids alone will not produce defect-free channels during deformation as shown by the schematic drawing in Figure 4-15.

Figure 4-17 shows the contribution of hardness to weighted average channel height. Although the data are scattered, a general trend of increase of channel height with hardness can be observed. However, the observed increase of channel height with hardness is probably due to the irradiation dose effect. With the same dose, the correlation is not observed. Compared Figure 4-17 to Figure 4-13, the same dependence was observed whether using measured hardening or that calculated from the microstructure.

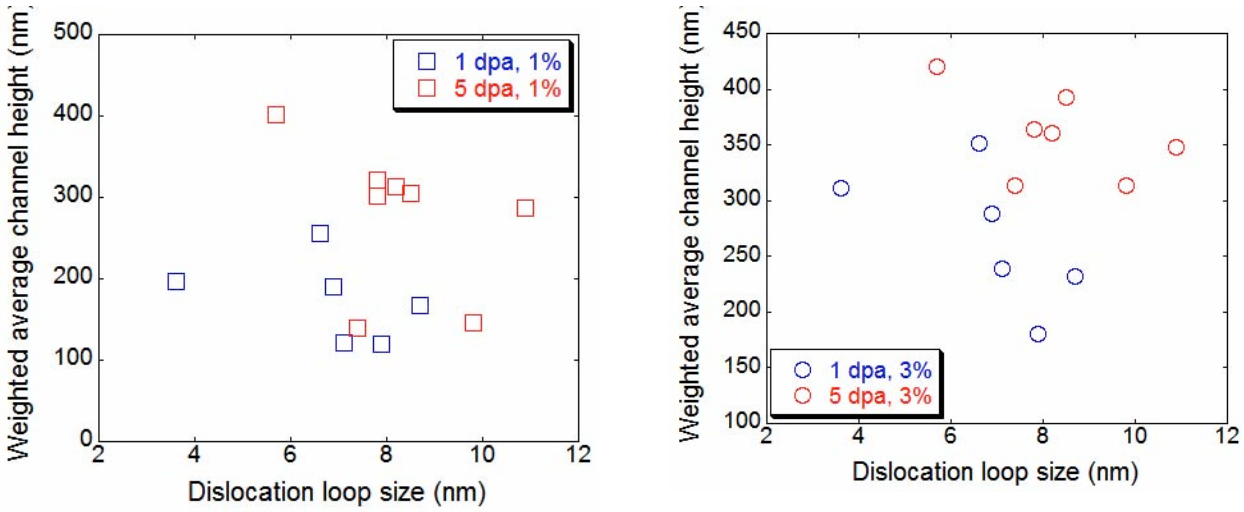

Figure 4-10: Dependence of weighted average channel height on dislocation loop size.

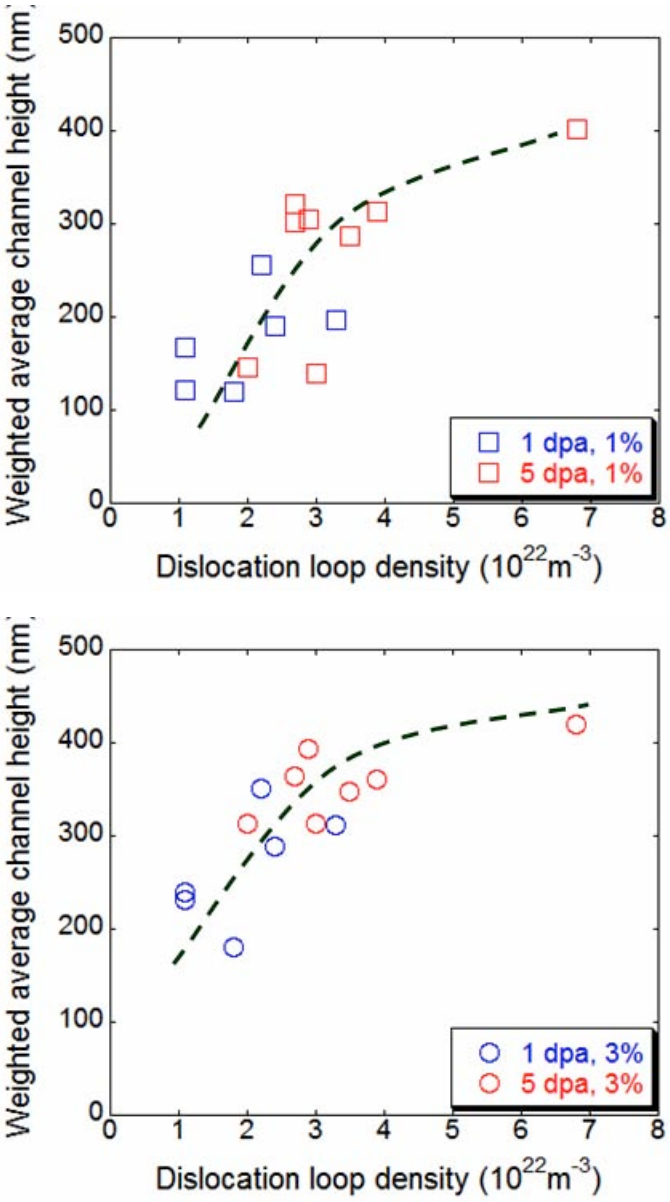

Figure 4-11: Dependence of weighted average channel height on dislocation loop density.

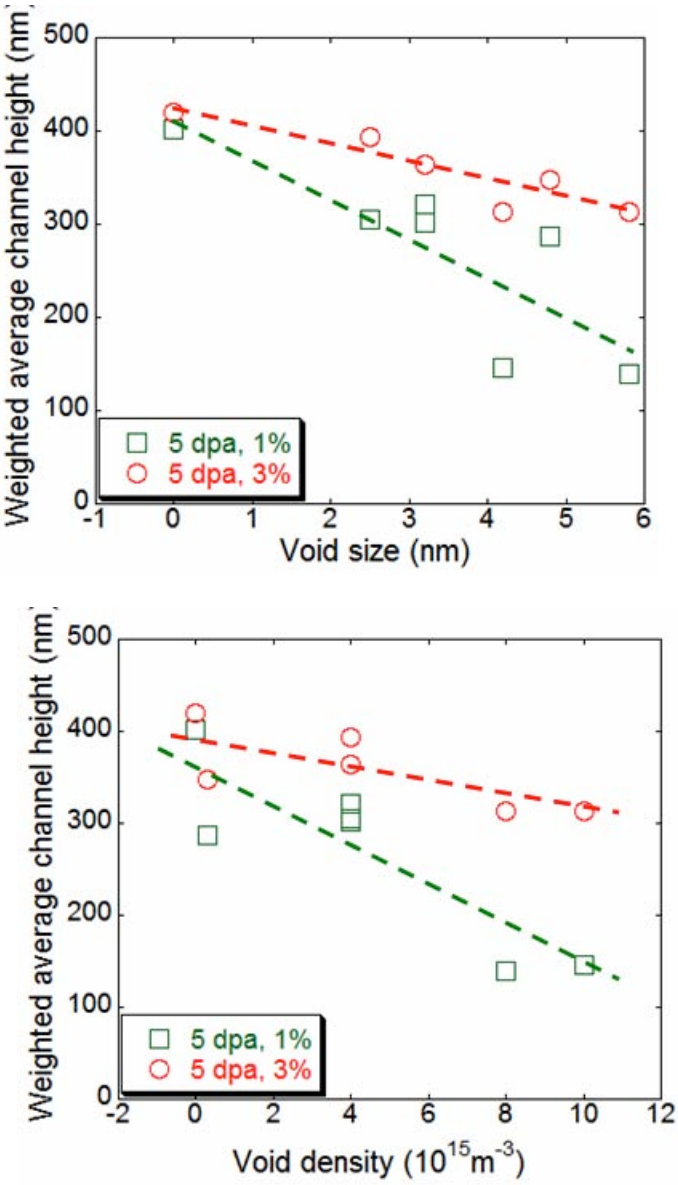

Figure 4-12: Dependence of weighted average channel height on dislocation loop density.

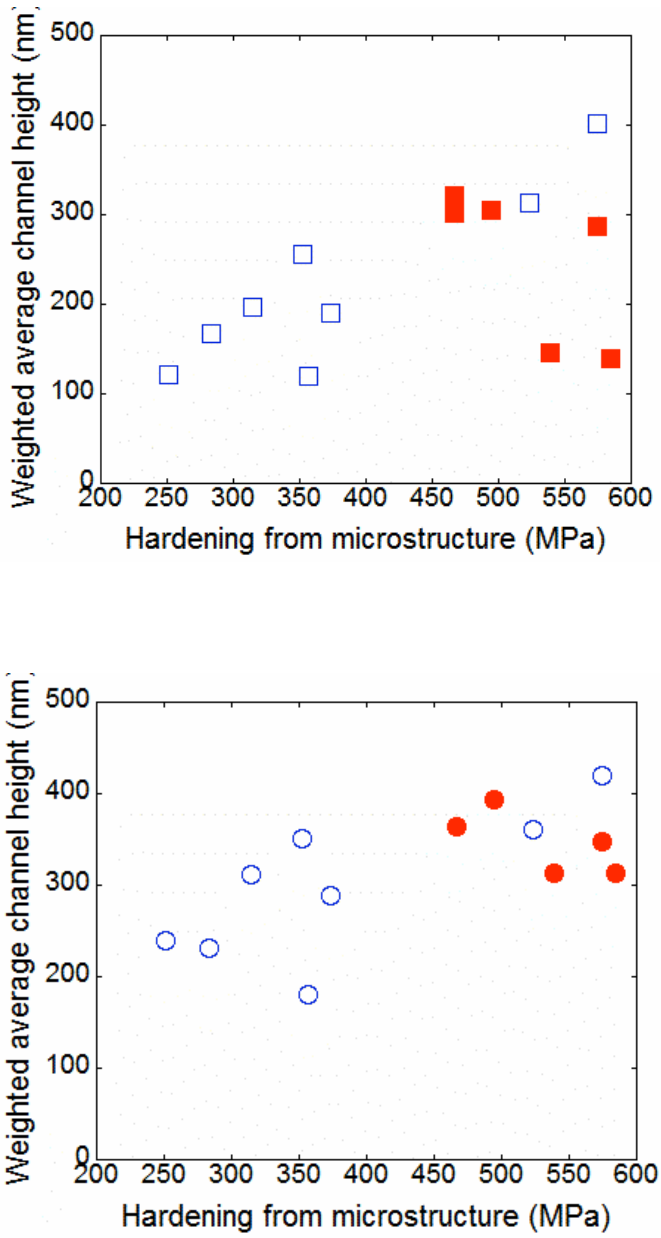

Figure 4-13: Dependence of weighted average channel height on hardening from microstructure. The red filled squares and circles indicate hardening *including* the part from voids.

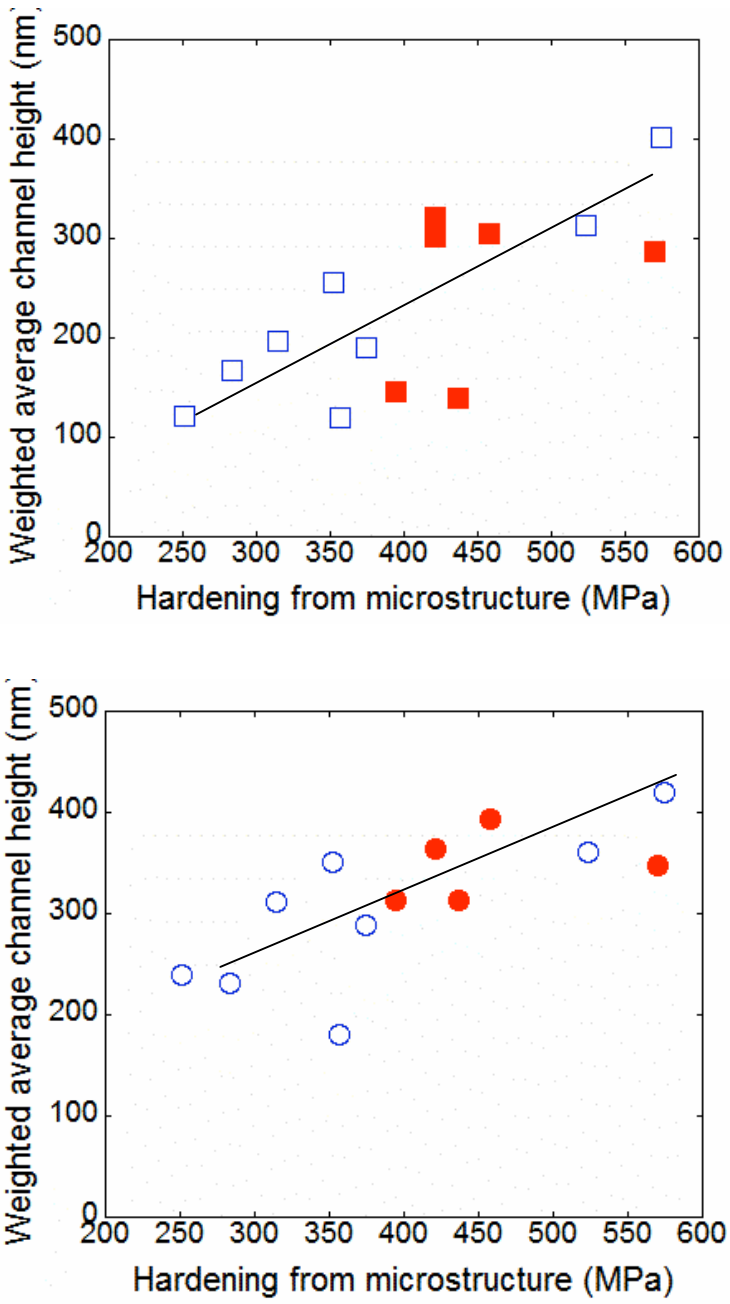

Figure 4-14: Dependence of weighted average channel height on hardening solely from dislocation loops. The red filled squares and circles indicate hardening *excluding* the part from voids.

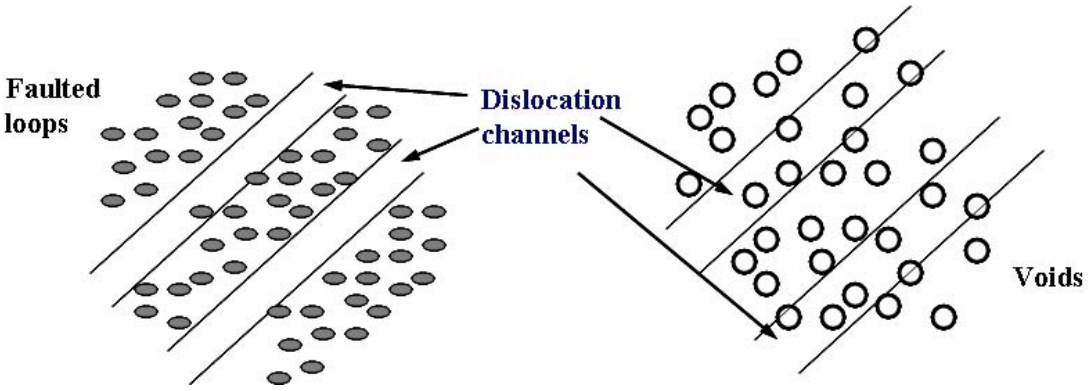

Figure 4-15: schematic showing the different effect of faulted dislocation loops and voids on the formation of dislocation channels.

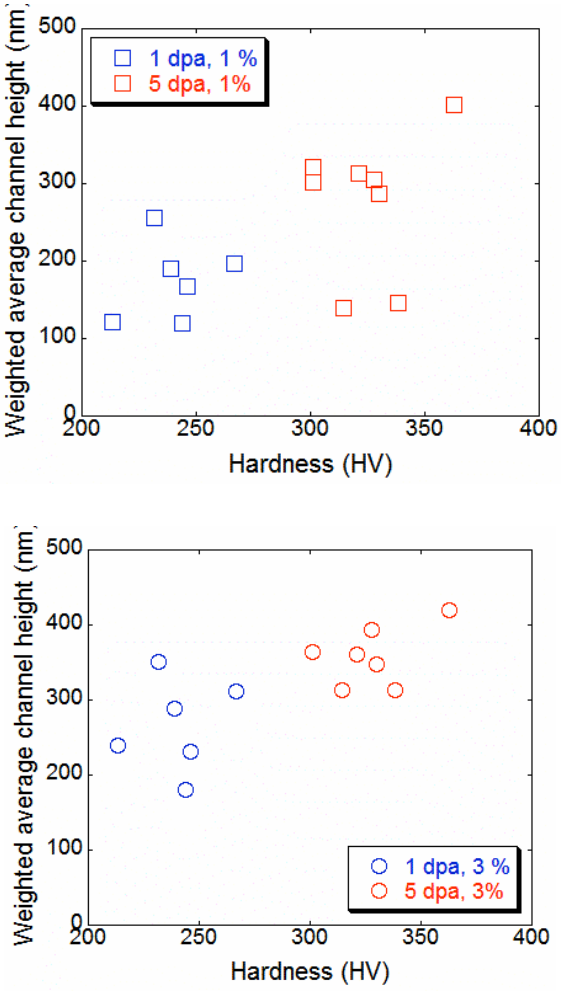

Figure 4-16: weighted average channel height as a function of hardness.

4.5.2 Stacking fault energy and localized deformation

Stacking fault energy (SFE) also strongly influences deformation mode. In fcc alloys, both the ease of cross-slip and stages of deformation have been correlated with SFE [44]. According to Courtney [45], higher stacking fault energy promotes cross slip. An alloy with a low stacking fault energy results in partial dislocations that are widely spaced. Higher stacking fault energies result in more closely spaced partials. Cross-slip requires the partial dislocations to recombine. Thus, the more widely separated partials result in a more difficult recombination process. As described by Lee et al. [42], increased separation of partials can also result in increased locking and pinning at jogs, further impeding dislocation motion and further decreasing the ability to cross slip. Thus, fcc alloys with low SFE's cross slip with difficulty and vice versa. A reduced tendency to cross-slip, by which dislocation motion can bypass obstacles, generally results in greater strain hardening.

When faced with a dislocation loop, a gliding dislocation in a high SFE alloy has the ability to simply continue motion on a different plane. To the contrary, a moving dislocation in a low SFE alloy cannot cross slip to bypass that dislocation loop and must overcome that obstacle. This leads to channeling and localized deformation, which, in turn, can impact cracking susceptibility. However, the low SFE still greatly reduces the possibility of cross-slip, which leads to enhanced dislocation pinning as described by Lee et al. [42]. This enhances dislocation pile-up at grain boundaries and promotes IASCC.

The dependence of channel height on SFE is shown in Figure 4-17. Localized deformation decreases with SFE but the dependence is not strong at 1% and is even weaker at the higher strain. Thus, while SFE may affect channeling, it does not appear to be a key factor in the channel height.

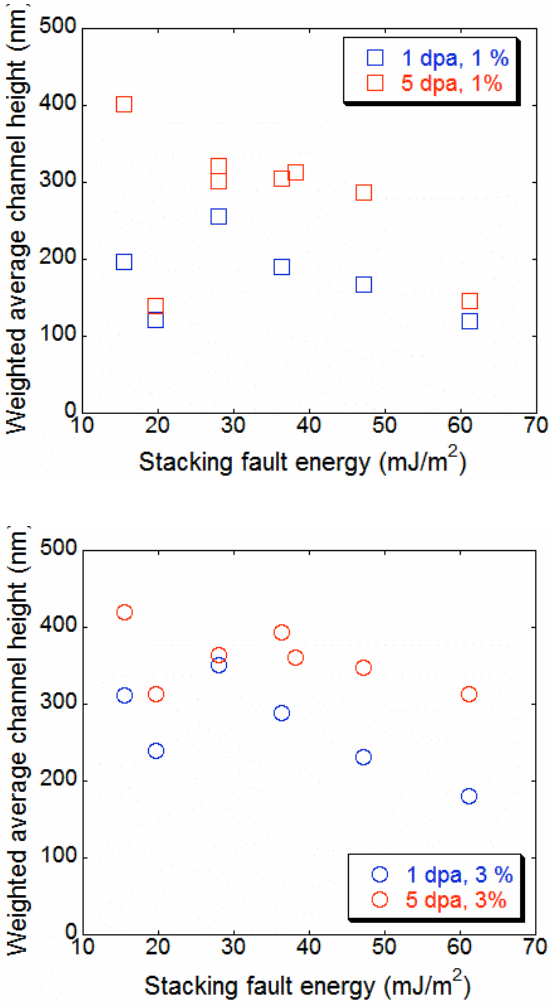

Figure 4-17: weighted average channel height as a function of SFE.

4.6 Irradiation assisted stress corrosion cracking

IASCC susceptibility can be measured by a number of ways. The most commonly used are crack initiation (whether cracks observed for an alloy under a certain testing condition), crack number density (number of cracks initiated per unit area), crack length per unit area (the extent of cracking), percentage of cracking with intergranular (%IG) character, and crack growth rate. The IG% was not characterized since the samples susceptible to cracking were only strained to 3% and the fracture surfaces were not obtained. However, the cracks on the samples are generally IG type. Crack growth rate experiments were not carried out because they were beyond the topic of this study.

In this section, IASCC susceptibility as measured by crack initiation, crack number density and crack length per unit area was examined against factors such as stacking fault energy, hardness, radiation-induced segregation and localized deformation. The factor that contributes the most to IASCC will be assessed using the correlation strength (S_{IASCC}), defined by:

$$S_{IASCC} = (L_{total} - L_{mixed})/L_{total}, \quad (4\text{-}4)$$

where L_{total} is the total examined range of a factor. It is calculated as the total range of the available data (the maximum value minus the minimum value for the available data). L_{mixed} is the range that both cracked and non-cracked samples are observed.

4.6.1 Stacking fault energy and IASCC

The contribution of stacking fault energy to crack initiation, crack number density and crack length per unit area is shown in Figure 4-18. The correlation strength of stacking fault energy with IASCC, $S_{IASCC}(SFE) = 0.5$. Figure 4-19 shows the IASCC susceptibility as measured by %IG cracking as a function of stacking fault energy determined using Rhode's correlation for various data in [43] and the correlation strength of stacking fault energy with IASCC was around 0.35. Only the alloys with very high SFE are resistant to cracking (>50 mJ/m^2, calculated from Rhode's correlation). In this study, alloy F and G with high SFE were resistant to cracking. However, no cracks were observed in alloy B with a low SFE either, which means that SFE is not a crucial factor for cracking.

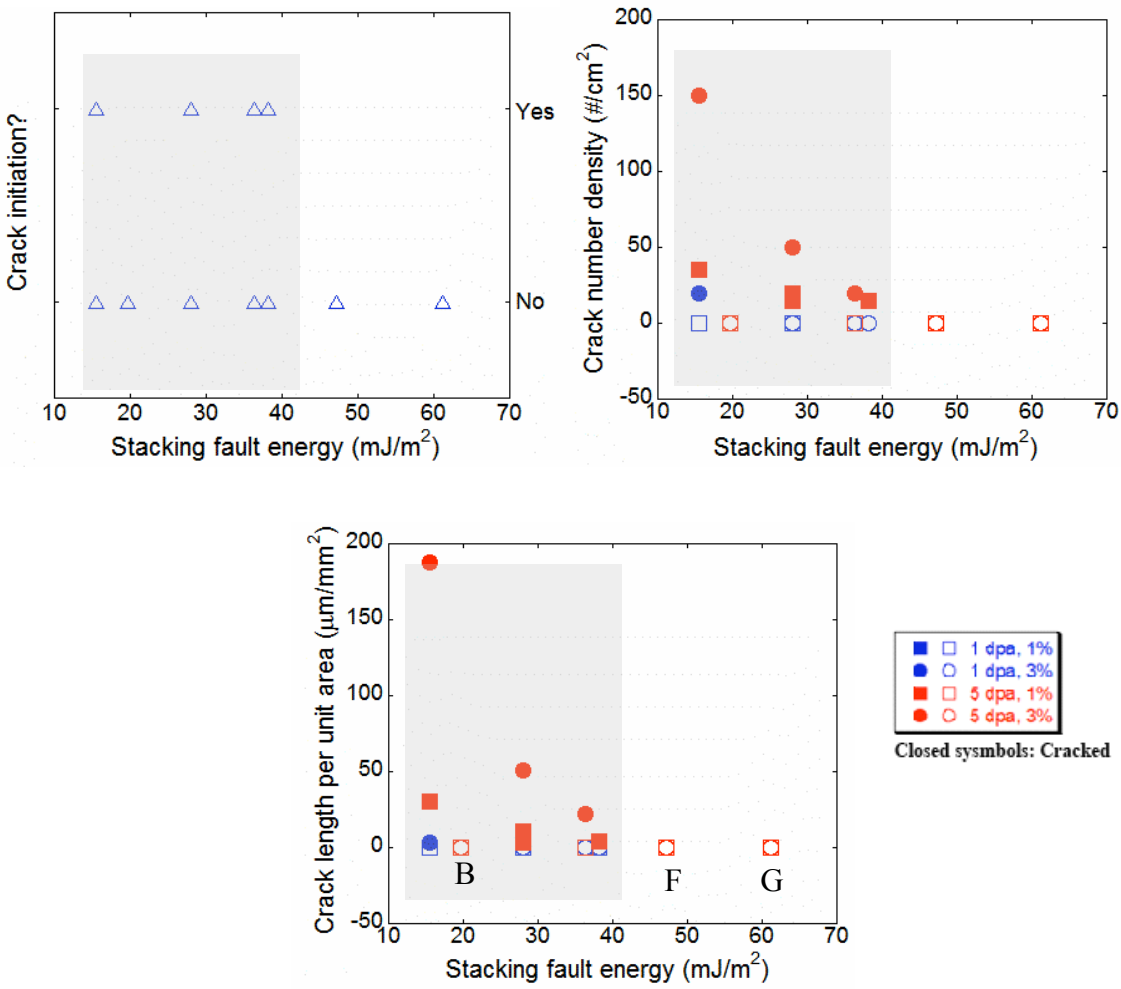

Figure 4-18: The contribution of stacking fault energy to crack initiation, crack number density and crack length per unit area. The correlation strength of stacking fault energy with IASCC, $S_{IASCC}(SFE) = 0.5$

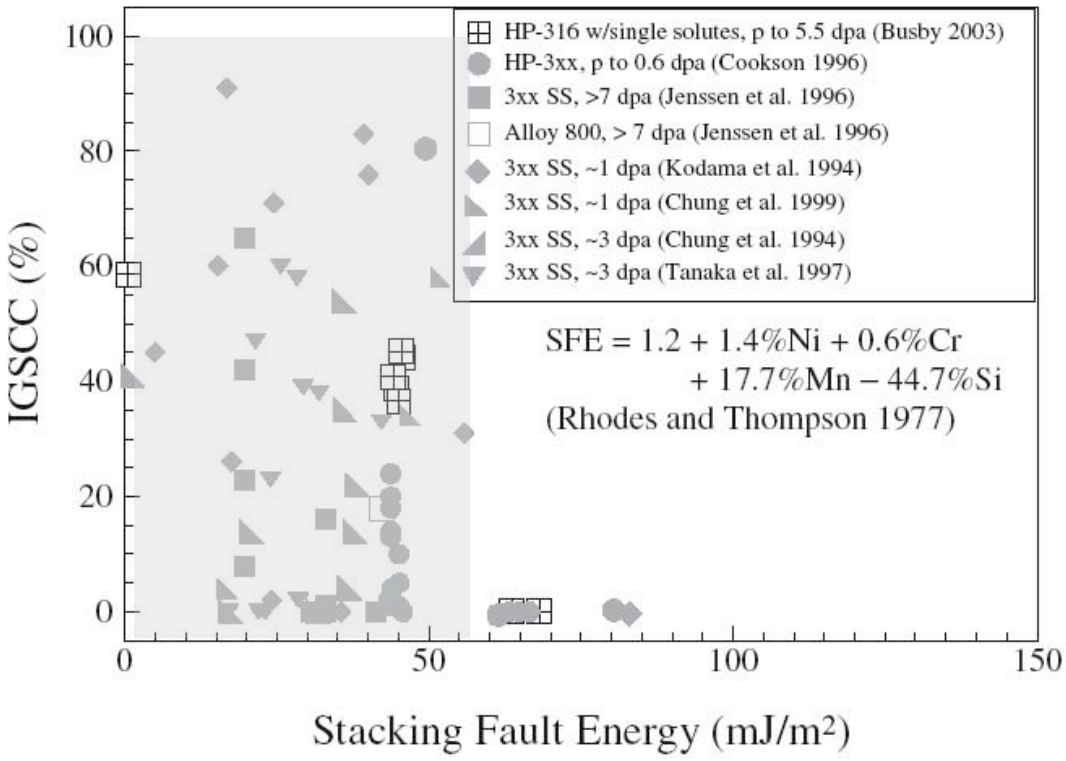

Figure 4-19: IASCC susceptibility as measured by %IG cracking as a function of stacking fault energy determined using Rhode's correlation [24] [43]. The correlation strength of stacking fault energy with IASCC, $S_{IASCC}(SFE)$=~ 0.35.

4.6.2 Hardness and IASCC

The formation of extended defects, following irradiation leads to an increase in the yield stress of the irradiated material, as these defects impede the motion of dislocations required for deformation to occur [46]. Conversely, the uniform tensile strain at failure drops dramatically. The increase in the stress required for deformation and loss of ductility have potentially important implications for the IGSCC susceptibility of stainless steels.

Bruemmer et al. [47] compiled existing data and compared yield strength measurements with IGSCC results and found that cracking was only observed after the yield stress has increased to above 600 MPa. Increased cracking of nickel base alloys in 288°C high purity water has been correlated with an increase in the degree of cold work and yield stress in the work of Speidel et al. [48]. Based on these results, it is expected that increased yield strength will be deleterious in terms of cracking in stainless steels. Since correlation exists between hardness and tensile strength, a similar contribution of hardness to IASCC would also be expected.

Figure 4-20 shows the contribution of hardness to crack initiation, crack number density and crack length per unit area. The correlation strength of hardness with IASCC, S_{IASCC}(hardness) = 0.54. Figure 4-21 shows the effect of yield strength on %IGSCC in 300-series stainless steels. The correlation strength of hardness with IASCC (S_{IASCC}(hardness)) is also ~0.5. The correlation of hardness with IASCC is consistent with the correlation of yield strength will IASCC.

The correlation strength of hardness (0.54) is about the same as that of SFE (0.5). Hardness is probably as important a factor that contributes to IASCC as SFE. However, recent post-irradiation annealing studies by Busby et al. [49], have shown that hardening is not the sole cause of IASCC. Following post-irradiation annealing, IASCC susceptibility was removed before any change in hardening was measured. Thus, hardening cannot be the only driving mechanism for IASCC

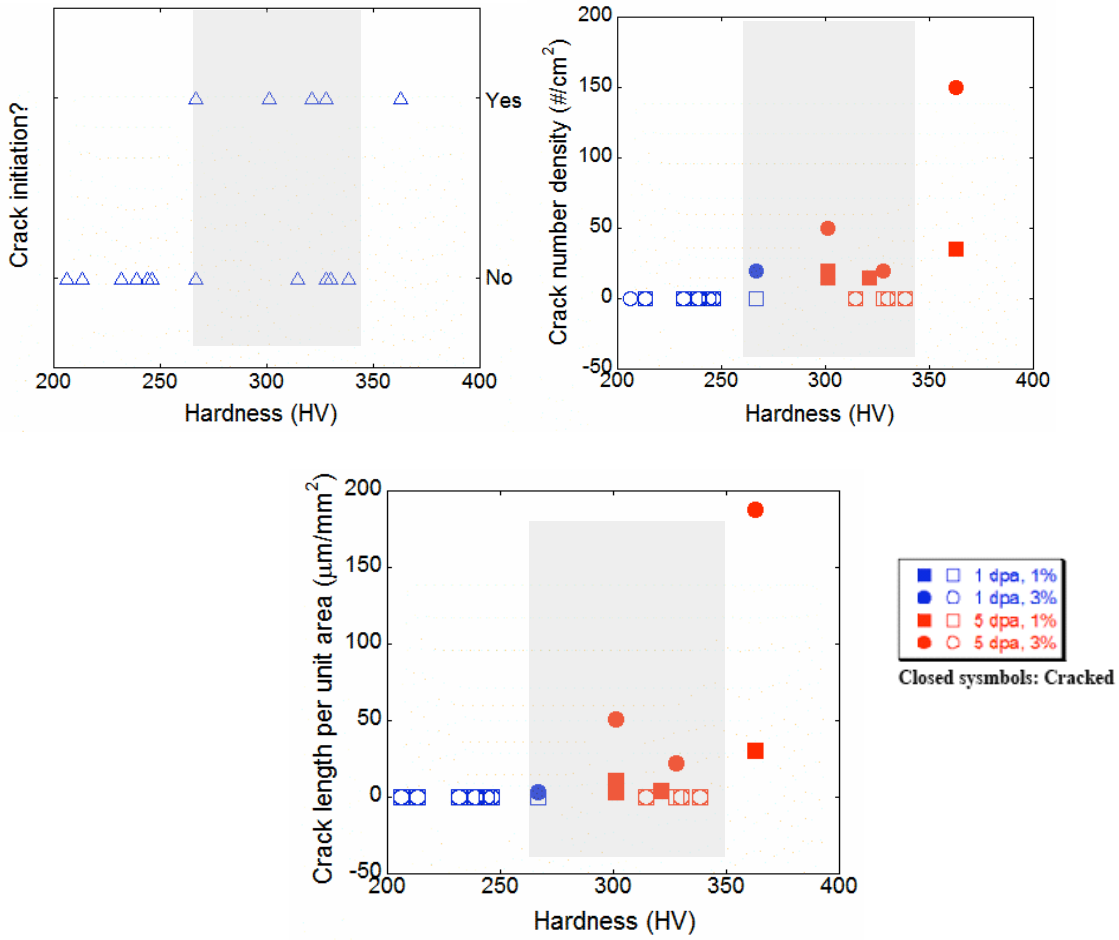

Figure 4-20: The contribution of hardness to crack initiation, crack number density and crack length per unit area. The correlation strength of hardness with IASCC, S_{IASCC}(hardness)= 0.54.

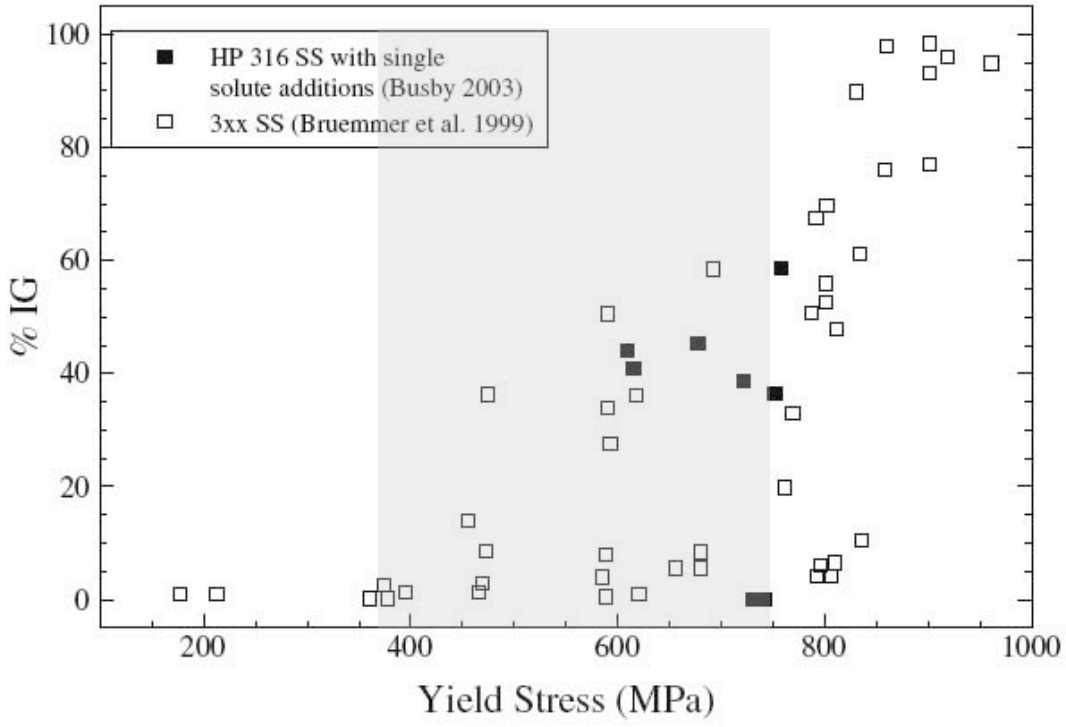

Figure 4-21: Effect of yield strength on %IGSCC in 300-series stainless steels where hardening is by irradiation [43]. The correlation strength of hardness with IASCC, S_{IASCC}(hardness) = 0.52.

4.6.3 Radiation-induced segregation and IASCC

One of the most extensively reviewed parameters in terms of stress-corrosion cracking in stainless steels is the Cr content, and more specifically, Cr depletion at the grain boundary (in both the unirradiated and irradiated state). The role of Cr as a beneficial element in iron-base alloys is well known [50, 51]. The presence of chromium increases the corrosion resistance through formation of chromium-rich oxide, which passivates the alloy and leads to a reduction in the rate of general corrosion. Changes in grain boundary chemistry have been implicated in intergranular stress corrosion cracking (IGSCC) of unirradiated stainless steel [53] and austenitic nickel-base [52] components for many years. The formation of chromium carbide ($Cr_{23}C_6$) precipitates at grain boundaries during heat treatment results in a local depletion of chromium in the regions surrounding the carbide, leaving the alloy in a sensitized state, which has been linked with cracking susceptibility in a number of studies [54-56]. Since RIS results in depletion of Cr at grain boundaries, analogous to that observed in thermally sensitized materials irradiated alloys are also suspected to be susceptible to intergranular cracking.

Figure 4-22 shows the contribution of grain boundary Cr content to crack initiation, crack number density and crack length per unit area. The correlation strength of RIS with IASCC, S_{IASCC}(SFE) = 0. That is, no correlation of GB Cr with cracking was observed in

the examined GB Cr range of 12-19 wt%. Figure 4-23 shows the effect of grain boundary chromium content on IGSCC for irradiated stainless steels complied in [43]. The correlation of GB Cr with IG% was about 0.4. However, in the rang of 12-19wt%, both cracked and uncracked alloys were observed, which is consistent with this study. Actually, only one data point with extreme high GB Cr (21 wt%) showed resistance to IG cracking. Alloys with GB Cr less than 12 wt% are subject to cracking.

The threshold for gain boundary Cr content that whether an alloy cracks or not in BWR environment probably is very high (>20 wt%?). Once the GB Cr is below that value, cracks may occur regardless of GB Cr content.

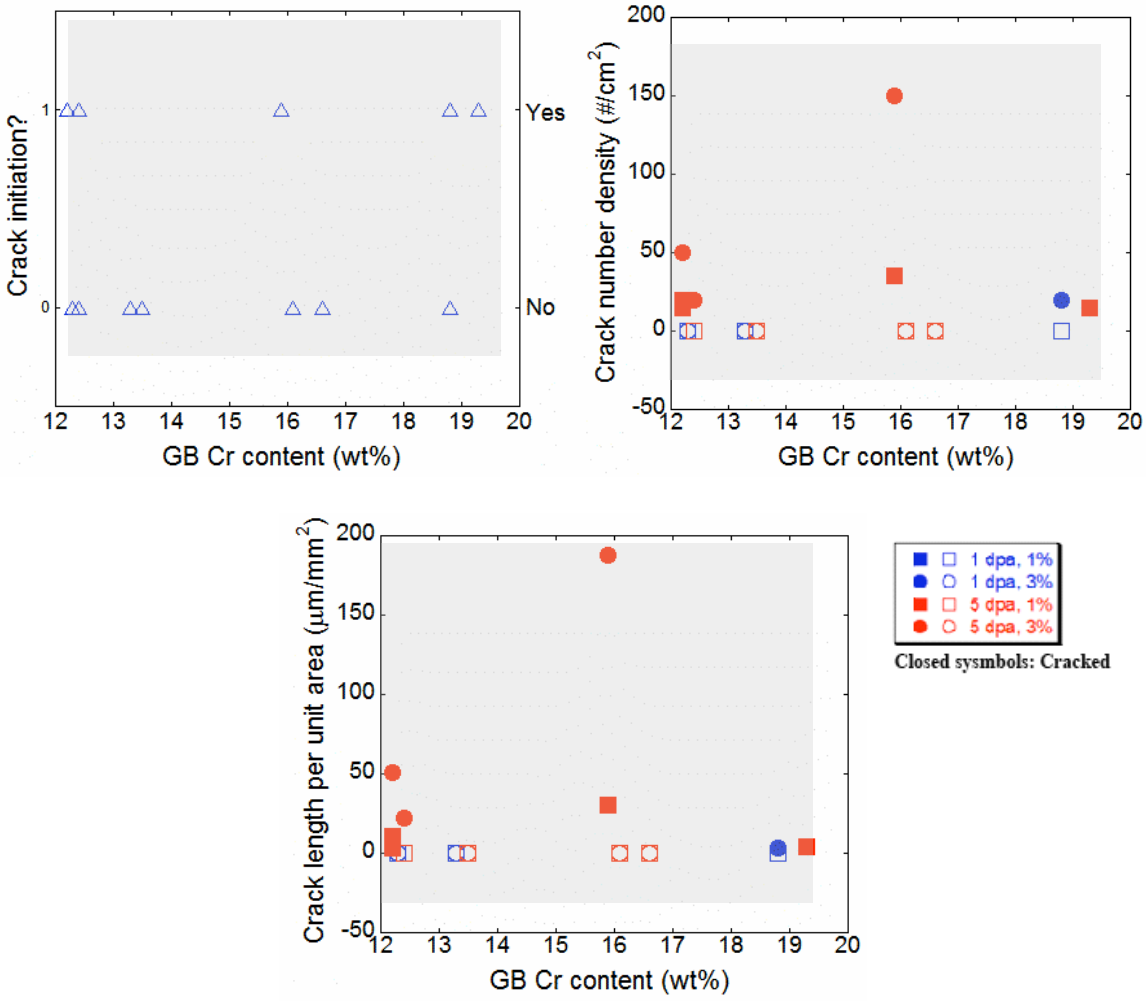

Figure 4-22: The contribution of grain boundary Cr content to crack initiation, crack number density and crack length per unit area. The correlation strength of grain boundary Cr content with IASCC, S_{IASCC}(GB Cr) = 0.

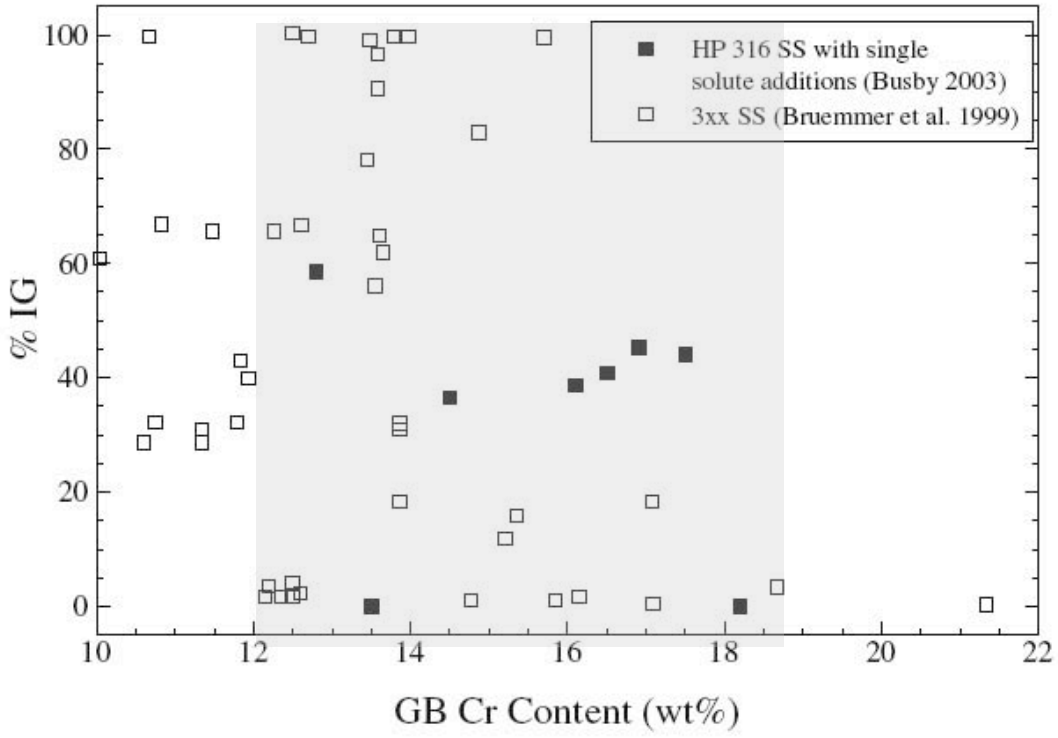

Figure 4-23: Effect of grain boundary chromium content on IGSCC for irradiated stainless steels [43]. The correlation strength of grain boundary Cr content with IASCC, S_{IASCC}(GB Cr) = 0.4.

4.6.4 Localized deformation and IASCC

Deformation mode has been linked to IASCC in several studies. Bailat et al. [57] reported a possible correlation between deformation mode and IASCC in the neutron-irradiated ABB stainless steels. Bruemmer et al. [40] noted that localized deformation can be detrimental to IASCC by promoting dislocation pileups at the grain boundaries. To accommodate local strain, a grain boundary may absorb dislocations at the boundary, emit new dislocations, create deformation microtwins, or crack if no further strain can be accommodated. Further, dislocation channels may have a finite life before pile-ups occur closing the channel to further dislocation glide. As available channels for plasticity are eliminated, the grain boundary may not be able to accommodate further strain by emitting new dislocations or microtwins.

Similarly, Busby et al. [58] also attributed the results of post-irradiation annealing studies to deformation mode. Analysis of the slip step bands on the surface of irradiated and annealed samples showed a difference in the degree of slip step systems, with those annealed at higher temperatures and/or times having a lower density of slip step systems. Annealed specimens failing with IG cracking had a higher density of slip bands, indicating that localized deformation leads to IG cracking.

The contribution of localized deformation as measured by the weighted average channel height to crack initiation, crack number density and crack length per unit area is shown in Figure 4-24. The correlation strength of localized deformation with IASCC, $S_{IASCC}(LD)$ = 0.88. The correlation strength is the highest among other examined factors (S_{IASCC}(Hardness) = 0.54, S_{IASCC}(SFE) = 0.5 and S_{IASCC}(GB Cr) = 0-0.4). Now the question is: Why localized deformation, especially the channel high, correlates to IASCC?

As discussed earlier, dislocation channeling is normally the main deformation mode in irradiated austenitic stainless steels. During deformation, the majority of dislocation activities occur in dislocation channels. Experimental observations [59,60] suggest that dislocations originating from grain boundaries and other stress concentrators are responsible for defect-free channels. General grain boundaries have many irregular sites such as micro scale ledges that, under certain stress, can emit lattice dislocations [61]. In the unirradiated alloy in the annealed condition, the dislocation density is very low. At the beginning of plastic deformation, the emitted lattice dislocations can glide easily once the applied stress reaches the critical resolved shear stress. However, in an irradiated alloy, the simultaneous glide of an array of dislocations is required to annihilate the defect obstacles and initiate defect-free dislocation channels [62]. Thus, even within the same grain boundary, only certain irregular sites with the capability to emit large number of dislocations can initiate dislocation channels. Since most of the applied deformation goes into these channels, the amount of deformation in the channels can be very large.

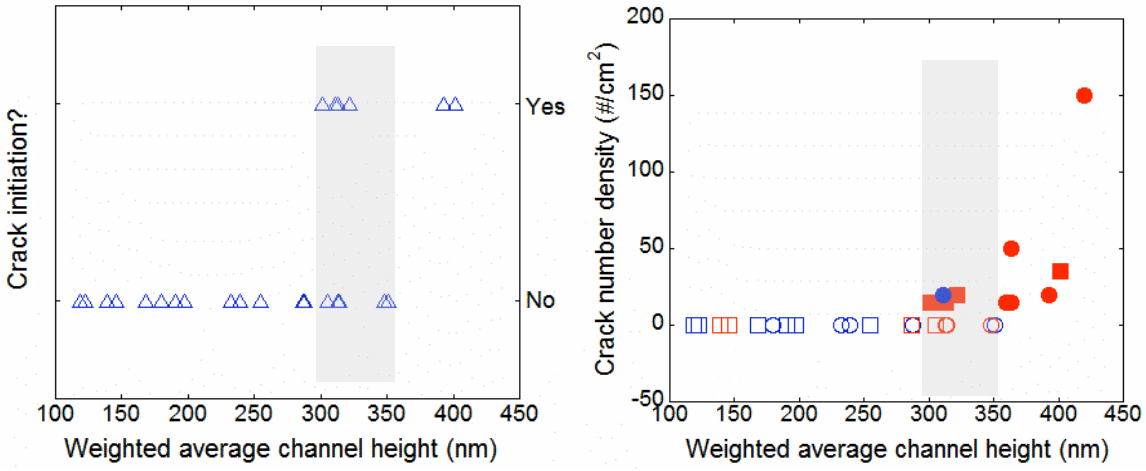

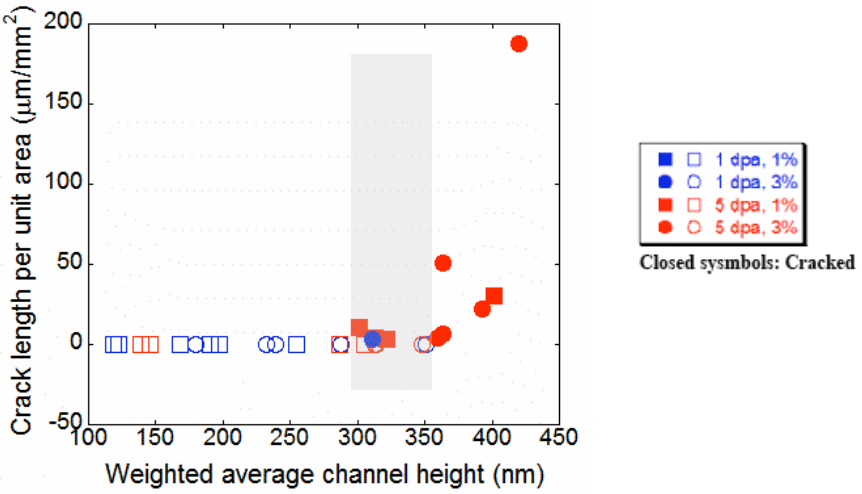

Figure 4-24: The contribution of localized deformation as measured by the weighted average channel height to crack initiation, crack number density and crack length per unit area. The correlation strength of stack fault energy with IASCC, $S_{IASCC}(SFE) = 0.88$.

Since IASCC is typically in the form of intergranular cracking, it is of interest to see how dislocation channels interact with grain boundaries to generate deformation in grain boundaries. Note that grain boundary deformation is believed to be an important factor for IG cracking [63]. In general, grain boundary deformation includes grain boundary sliding and migration. Grain boundary migration is a diffusionally accommodated process and mostly occurs at high temperatures. However, grain boundary sliding can be either diffusionally accommodated or achieved by glide of grain boundary dislocations. Furthermore, grain boundary sliding can be significantly enhanced by the impingement of lattice dislocations on the grain boundary [64, 65].

Figure 4-25(a) is a surface plot containing a grain boundary obtained by AFM of alloy C irradiated to 5 dpa and strained to 1%. A schematic of the plot is shown in Figure 4-25 (b). The grain boundary plane is indicated by arrows in both figures. Grain boundary sliding is clearly shown as the grain on the left of the boundary plane is displaced nearly vertically relative to the one on the right. The amount of displacement caused by sliding was measured to be ~380 nm. The sliding is likely caused by the interaction of the large slip channel (~500 nm height, the boldest line in Figure 4-25 (b)) with the grain boundary. However, among all eight grain boundaries examined by AFM in alloy G, no visible grain boundary sliding is observed. Figure 4-25 (c) shows an example of AFM scan of a grain boundary in alloy G. A large number of small slip channels intersecting the grain boundary causing a relatively large deformed area (light color in Figure 4-25 (c)) containing the grain boundary (dashed line in Figure 4-25 (c)). The deformation is not confined to the grain boundary plane when small channels intersect grain boundaries.

Grain boundary sliding is known to occur by the motion of grain boundary dislocations rather than by instantaneous shear of the entire boundary [64]. When a newly initiated dislocation channel intersects a grain boundary, it results in a pile-up of dislocations. When a higher stress is applied on the sample, more dislocations will join the dislocation

queue. At a certain point, the leading dislocation will merge into the grain boundary. It becomes an extrinsic grain boundary dislocation (EGBD) and further dissociates into grain boundary dislocations. As more lattice dislocations under stress "squeeze" into the grain boundary, the stress on the grain boundary dislocations will be high enough to cause the dislocations to glide. The glide of dislocations in the grain boundary results in grain boundary sliding. It is noteworthy that grain boundary sliding is very likely to be localized to a small region of the grain boundary close to the intersection with the channel. Localized grain boundary sliding is probably the cause of the formation of deformation ledges near slip channel – grain boundary intersections in Figure 4-26. For the same reasoning, the crack initiation sites in Figure 3-18 may be linked to localized grain boundary sliding. For a large channel of 500 nm in height, about 2000 dislocations have interacted with the grain boundary. This large number of dislocations will likely lead to a ledge in an inert environment. When this occurs on the samples tested under BWR conditions, localized grain boundary sliding may reach to the surface and rupture the oxide film above the grain boundary and IASCC initiates. In contrast, in alloys with small dislocation channels, the deformation is distributed in a large area around the grain boundary. A significant amount of grain boundary dislocation activities is therefore not expected.

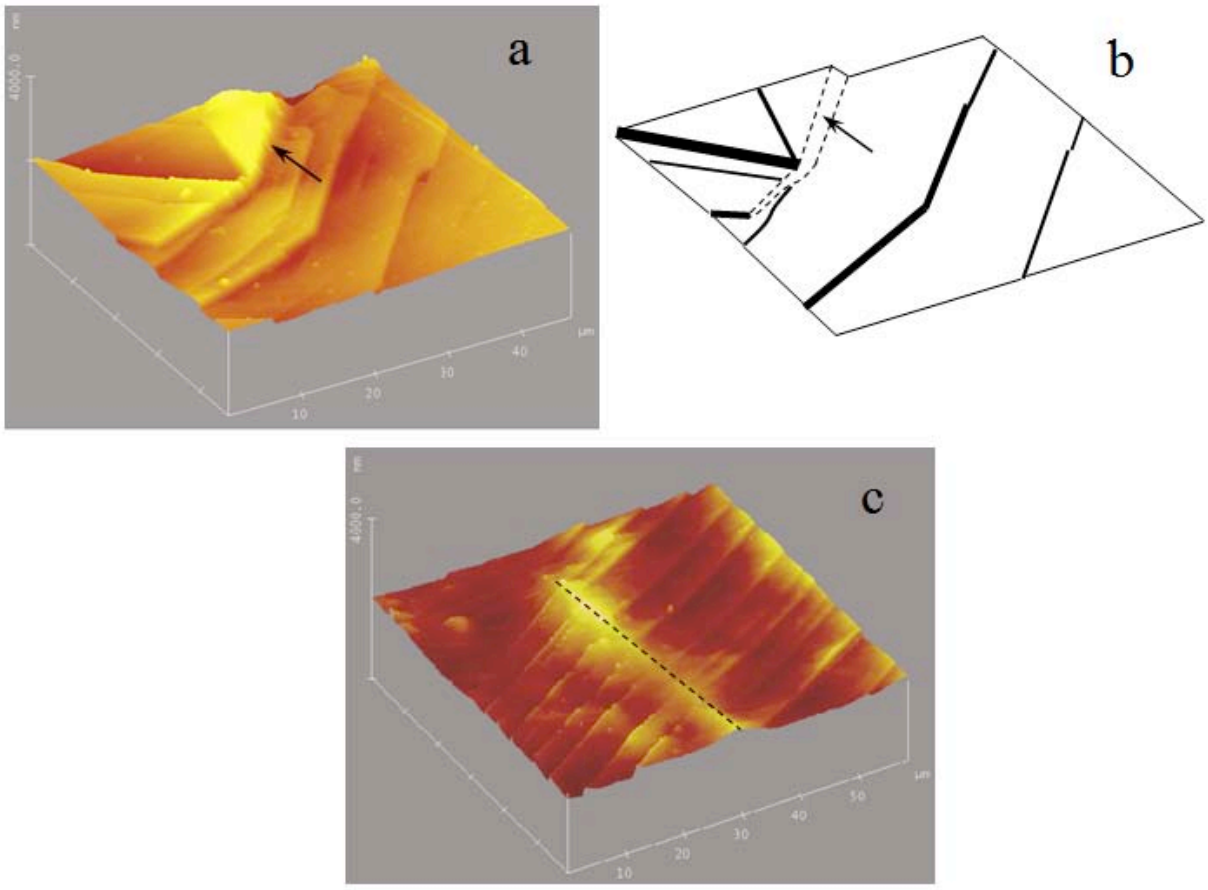

Figure 4-25: Deformation at grain boundaries as characterized by AFM: (a) a surface plot in alloy C at 5 dpa and 1% strain; (b) a schematic of the plot in (a); (c) a surface plot in alloy G at 1 dpa and 3% strain. Arrows in (a) and (b) show the grain boundary deformation in alloy C. The amount of "planar" deformation at the grain boundary caused by grain boundary sliding is bounded by dashed line in (b). The bold lines in (b) represent slip channels in (a). The dashed line in (c) indicates the position of the grain boundary in alloy G. Light color surrounding the dashed line is the sign of the broadened deformation in the grain boundary area.

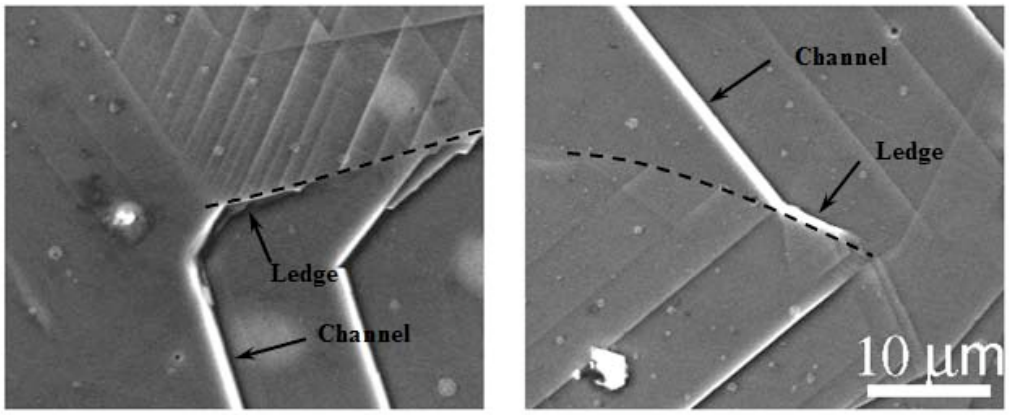

Figure 4-26: Ledge formation due to dislocation channel and grain boundary interaction in proton-irradiated C strained to 1% in argon at 288°C. The position of the grain boundary is indicated by a dashed line.

4.6.5 Combination of SFE, hardness, RIS and Localized deformation

The contributions of SFE, hardness, RIS and localized deformation to IASCC can be summarized in Figure 4-27. Localized deformation in slip channels is affected by irradiation microstructures (especially, the dislocation loop density) which is affected by alloy composition, SFE and high irradiation dose. The SFE affects the irradiation microstructure and dislocation slip behavior, and therefore shows some degree of correlation with localized deformation. Irradiation microstructure contributes to localized deformation and hardness, giving it a higher degree of correlation with cracking. RIS, which is affected by alloy composition and irradiation dose, shows weak correlation with IASCC. Localized deformation shows the best correlation with IASCC among all the examined factors.

Like other contributors to IASCC, localized deformation alone may not cause intergranular cracking. This is why for the same amount of deformation and irradiation dose, cracks were not observed in any alloys tested in argon atmosphere. Both corrosion and deformation at grain boundary are important in understanding the mechanism of IASCC. Water chemistry and RIS at grain boundary would contribute to accelerated IASCC while localized grain boundary sliding would contribute to deformation. For different environment, the susceptibility to IASCC may differ even with the same amount of grain boundary deformation. Since these cracking measurements were focused on crack initiation, results indicate that localized deformation may be most important in the initiation of cracks.

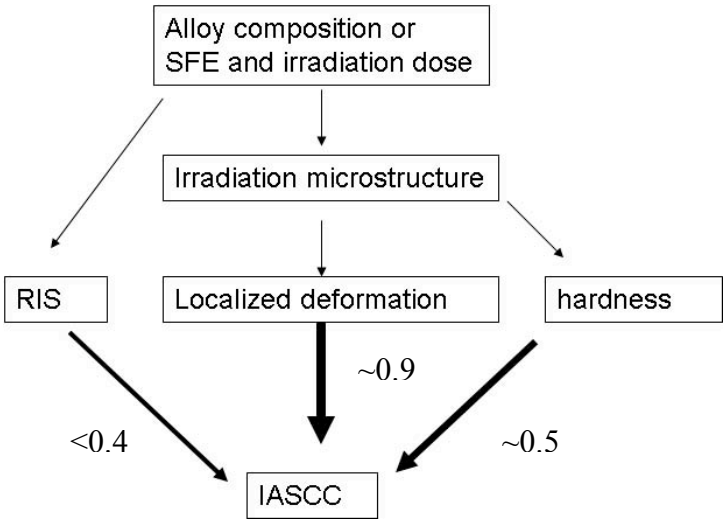

Figure 4-27: Contribution of SFE, hardness, RIS, and localized deformation to IASCC initiation. The numbers are the correlation strength.

5. Conclusions

The stacking fault energies were measured in all seven alloys and the results were compared to the predicted values. The measured SFE showed the same trend as predicted values and were within the range of similar alloys from other experimental measurements.

The microstructures were examined for all alloys irradiated to 1 and 5 dpa. A high density of dislocation loops was observed in alloy A. Voids were observed in all high purity alloys B-G at the highest dose. The swelling decreased with Ni content and increased with Cr content. This is consistent with the literature. Irradiation hardening was observed in all irradiated alloy. Greater hardening was observed in 5 dpa samples. The change of yield stress calculated from irradiation hardening correlates reasonably well with that calculated from irradiation microstructures.

Radiation-induced segregation was measured in selected alloys at selected conditions. Cr was found to deplete at grain boundaries and Ni was found to enrich at grain boundaries. Larger amounts of segregation ere found in higher Ni content alloys.

The IASCC susceptibility of the studied alloys increases with increasing irradiation dose when tested in a simulated BWR environment. Alloy A is susceptible to cracking at both 1 dpa and 5 dpa. Alloys C, D and E are resistant to cracking at 1 dpa but are susceptible to cracking at 5 dpa. Alloy B, F and G shows cracking resistance at both doses. IASCC was found to initiate at locations where a large slip channel intersects a grain boundary in simulated BWR environment.

Localized deformation was characterized in proton-irradiated austenitic alloys A-G irradiated to 1 and 5 dpa and strained to 1% and 3% at 288ºC in argon. The slip channels in all alloys are inhomogeneous at 1% plastic strain. At a higher strain of 3%, slip channels become more homogeneous. The average step height in the channel is much smaller in alloys B, F and G. High irradiation dose results in larger channel height. Localized grain boundary sliding was observed to be associated with large dislocation channels intersecting grain boundaries. Large regions of deformation around grain boundaries were observed when small dislocation channels interact with grain boundaries.

Localized deformation was found to be dependent on irradiation microstructures. The dislocation loops contribute more to localized deformation than voids because voids do not contribute to the formation of dislocation channels.

The correlation of SFE, hardness, RIS and localized deformation with IASCC was examined. The correlation strength was the highest for localized deformation (0.88) followed by hardness (0.54), SFE (0.5) and RIS (<0.4). Localized grain boundary deformation caused by the intersection of large slip channels with grain boundaries is believed to be important for IG cracking.

6. References

1. Barry Gordon, General Electric Nuclear Energy, Personal communication, October, 2003.
2. Generation IV Roadmap, (www.ne.doe.gov).
3. P.L. Andresen, F.P. Ford, S.M. Murphy, and J.M. Perks, *Proc. 4th Int. Symp. on Environmental Degradation of Materials in Nuclear Power Systems - Water Reactors* NACE International, Houston, 1990, p. 1.
4. G.S. Was, "Recent Developments in Understanding IASCC," *Proc. 11th Int. Symp. on Environmental Degradation of Materials in Nuclear Power Systems - Water Reactors*, American Nuclear Society, La Grange, IL, 2003, p. 965.
5. J.T. Busby, G.S. Was, and E.A. Kenik, "Isolation of the Role of Radiation-Induced Segregation in IASCC of Proton-Irradiated Austenitic Stainless Steels," *J. Nucl. Mater.*, **302** (2002) 20-40.
6. A.J. Jacobs, S. Dumbill, "Effects of Low Temperature Annealing on the Microstructure and Grain Boundary Chemistry of Irradiated 304 SS and Correlations with IASCC, "*Proc. 7th International Symposium on Environmental Degradation of Materials in Nuclear Power Systems – Water Reactors*,(NACE International, Houston, TX, 1995, pp. 1021.
7. S. Nishimura, Y. Ishiyama, M. Kodama, R. Katsura, Private communication.
8. K. Asano, K. Fukuya, K. Nakata, and M. Kodoma, Proceedings of the Fifth International Symposium on Environmental Degradation of Materials in Nuclear Power Systems-Water Reactors, D. Cubicciotti (Ed.), American Nuclear Society, 1992, p. 838.
9. S. Katsura, Y. Ishiyama, N. Yokota, T. Kato, K. Nakata, K. Fukuya, H. Sakamoto, and K. Asano, "Post-Irradiation Annealing Effects of Austenitic SS in IASCC," *Corrosion 98 Conference*, (NACE , Houston, 1998), Paper 132.
10. S.M. Bruemmer, EPRI report, RP 4068-20, EPRI, August 2000.
11. K. Fukuya, M. Nakano, F. Katsuhiko, M. Kodama, and T. Torimaru, *Proc. Eleventh International Conference On Environmental Degradation of Materials in Nuclear Power Systems-Water Reactors*, L. Nelson (Ed.), American Nuclear Society, La Grange Park, IL, 2003, p. 1123.
12. M.C. Hash, J.T. Busby, and G.S. Was, "The Effect of Hardening Source in Proton-Irradiation Assisted Stress Corrosion Cracking of Austenitic Stainless Steel, Effects of Radiation on Materials: 21st International Symposium, ASTM STP 1447, M. R. Grossbeck, T. R. Allen, R. G. Lott and A. S. Kumar, Eds., American Society for Testing of Materials, West Conshohocken, PA, in press.
13. Thompson and Bernstein, Advances In Corrosion Science and Technology, R.W. Staehle, ed., Vol. 7, Plenum, 1980.
14. R.P. Tucker, M.S. Wechsler, and S.M. Ohr, in "Radiation Damage in Reactor Materials," Vol. 1., International Atomic Energy Agency, Vienna, 1969, p. 215.
15. K. Farrell, T. S. Byun and N. Hashimoto, "Deformation Mode Maps for Tensile Deformation of Neutron Irradiated Structural Materials, *J. Nucl. Mater.*, **335** (2004) 471.

16. F.B. Pickering, "Physical Metallurgical Development of Stainless Steels," Proceedings of the Conference on Stainless Steels 84, Gothenberg, Sweden, 1984, The Institute of Metals, London, 1985, p.2.
17. TRIM 97 program, J.F. Ziegler, J.P. Biersack, IBM Corp., Yorktown, NY.
18. "Standard Practice for Neutron Radiation Damage Simulation by Charged-Particle Irradiation," ASTM Designation E 521-89, Annual Book of ASTM Standards, Vol. 12.02, p. D-9, American Society for Testing and Materials, Philadelphia, Pa, 1989.
19. S. M. Bruemmer et al., "Characterization of Neutron-Irradiated 300-Series Stainless Steels to Assess Mechanisms of Irradiation Assisted Stress Corrosion Cracking," Final Report, EPRI Project WO4068-20, November 2000.
20. J.T. Busby, M. Hash and G.S. Was, J. Nucl. Mater 336 (2005), p. 267.
21. D. Hull and D.J. Bacon, Introduction to Dislocations, International Series on Materials Science and Technology, Vol. 37, Pergamon Press, 1984, p 98.
22. G.S. Was and P.L. Andresen, JOM, 44 (4) (1992), p. 8.
23. P. L. Andresen, "Irradiation-Assisted Stress-Corrosion Cracking," in Stress–Corrosion Cracking, Materials Performance and Evaluation, Russell H. Jones, Ed., ASM International, Materials Park, OH, 1992, p. 181.
24. L. Vitos, J.-O. Nilsson, B. Johansson, Acta Materialia, 54 (2006) 3821–3826.
25. C.G. Rhodes and A.W. Thompson, Met. Trans. A 8A 901 (1977).
26. G. S. Was, "Use of Proton Irradiation to Understand IASCC in LWR's," Final Report, EPRI, RP4068-26, 2001.
27. G. S. Was, J. T. Busby, T. Allen, E. A. Kenik, A. Jensson, S. M. Bruemmer, J. Gan, A. D. Edwards, P. M. Scott and P. L. Andreson, "Emulation of neutron irradiation effects with protons: validation of principle", J. Nucl. Mater., 300 (2002) 198.
28. R.D. Carter, et al., "Effects of proton irradiation on the microstructure and microchemistry of type 304L stainless steel," J. Nucl. Mater., 205 (1993) p. 361-373.
29. F.A. Garner, W.G. Wolfer, J. Nucl. Mater., 102 (1981) 143.
30. VTT in-kind contribution for CIR-II, presented at CIR-II Steering Committee Meeting, May 2002, New Orleans, USA.
31. G.S. Was et al., "Microchemistry and microstructure of proton-irradiated austenitic alloys: toward an understanding of irradiation effects in LWR core components," J. of Nucl. Mater., 270 (1999) p. 96-114.
32. J.F. Bates, J.J. Holmes, M.M. Paxton and J.L Straaslund, U.S. Patent. 3,856,517, 1974.
33. H.R. Brager, ASTM STP 570, 1975.
34. W.G. Johnston, T. Lauritzen, J.H. Rosolowski, and A.M. Turkalo, "The Effect of Metallurgical Variables on Void Swelling," Radiation Damage in Metals, American Society of Metals, N.L. Peterson and S.D. Harkness, Eds., 1975, p. 221.
35. T.R. Allen, J.I. Cole, J. Gan, G.S. Was, R. Dropek and E.A. Kenik, J. Nucl. Mater., 342 (2005) 90-100.
36. A. Seeger, Proc. 2nd UN Int. Conf. On Peaceful Uses of Atomic Energy, Geneva, Sept., 1958, Vol. 6, p. 250.
37. G.I. Taylor, J. Inst. Met. 62 (1938) 307.
38. G.E. Lucas, J. Nucl. Mater. 206 (1993) 287-305.

39. G. S. Was, “The Use of Proton Irradiation to Determine IASCC Mechanisms in Light Water Reactors: Solute Addition Alloys,” Final Report, EPRI, EP-P3038/C1434, 2003.
40. S.M. Bruemmer, J.I. Cole, J.L. Brimhall, R.D. Carter, and G.S. Was, Proc. Sixth Int'l Symp. on Environmental Degradation of Materials in Nuclear Power Systems - Water Reactors, TMS, 1993, p. 537.
41. J. Cole, J.L. Brimhall, J.S. Vetrano, and S.M. Bruemmer, 17th Int. Symp on Effects of Rad. On Materials, STP1270, 1996.
42. E.H. Lee, M.H. Yoo, T.S. Byun, J.D. Hunn, K. Farrell, and L.K. Mansur, Acta mater., 49 (2001), p. 3277-3287.
43. G. S. Was and J. T. Busby, Philosophical Magazine, 85 (2005) 443.
44. I. Karaman, H. Sehitoglu, Y.I. Chumlyakov, and H.J. Maier, J. of Materials, July, 2002, p. 31.
45. T. Courtney, “Mechanical Behavior of Materials," McGraw-Hill, 1996, page 116.
46. D. Olander, Fundamental Aspects of Nuclear Reactor Fuel Elements, NTIS TID26711-P1, p. 396-412.
47. S.M. Bruemmer, E.P. Simonen, P.M. Scott, P.L. Andresen, G.S. Was, and J.L. Nelson, J. of Nucl. Mater., 274 (1999) p. 299-314.
48. M.O. Speidel and R. Magdowski, Proc. Sixth Int. Symp. On Env. Deg. of Materials in Nuclear Power Systems-Water Reactors, R.E. Gold and E.P. Simonen (Ed.), (TMS, 1993), p. 361-369.
49. J.T. Busby, G.S.Was, and E.A. Kenik, J. of Nucl. Mater., 302 (2002) p 20.
50. A.J. Sedriks, Corrosion of Stainless Steel, John Wiley and Sons, New York, 1979.
51. R.H. Jones, in Metals Handbook, 9th Ed. Vol. 13, (1987) p. 145.
52. J.T. Busby, G.S.Was, and E.A. Kenik, J. of Nucl. Mater., 302 (2002) p 20.
53. S. M. Bruemmer and G. S. Was, "Microstructural and michrochemical mechanisms controlling intergranular stress corrosion cracking in light-water-reactor systems," J. Nucl. Mater. 216 (1994) 348.
54. S.M. Bruemmer, Mat. Sci. Forum, 46 (1989) p. 309.
55. S.M. Bruemmer and L.A. Charlot, Scripta Met., 20 (1986) p. 1010.
56. P.L. Andresen, Proc. Fifth Int. Symposium on Env. Deg. of Materials in Nuclear Power Systems-Water Reactors, D. Cubicciotti (Ed.), Monterey CA, ANS (1992) p. 209.
57. C. Bailat, A. Almazouzi, M. Baluc, R. Schaublin, F. Groschel, and M. Victoria, J. Nucl. Mater., 283-287 (2000), p. 446-450.
58. J.T. Busby, M.M. Sowa, G.S. Was, and E.A. Kenik, Proceedings of 21st Int. Symp on Effects of Rad. On Materials, ASTM, 2002.
59. D.J. Edwards, B.N. Singh and J.B. Bilde-Sørensen, J. Nucl. Mater., 342 (2005) 164.
60. I.M. Robertson, J. Robach, B. Wirth and A. Arsenlis, Mat. Res. Soc. Symp. Proc. Vol. 779, 2003, Materials Research Society.
61. E.V. Esquivel and L.E. Murr, Materials Science and Engineering A, 409 (2005) 13.
62. T.S. Byun and N. Hashimoto, J. Nucl. Mater., 354 (2006) 123.
63. B. Alexandreanu and G.S. Was, Corrosion 59 705 (2003).
64. G.R. Kegg, C.A.P. Horton and J.M. Silcock, Phil. Mag., 27 (1973) 1041.
65. R.J. Kurtz, R.G. Hoagland and J.P. Hirth, Phil. Mag. A, 79 (1999) 665.